

Masterarbeit

LOCAL PROBING OF THE
BEREZINSKII–KOSTERLITZ–THOULESS
TRANSITION IN A
TWO-DIMENSIONAL BOSE GAS

Niclas Luick

Erstgutachter: Prof. Dr. Henning Moritz

Zweitgutachter: Prof. Dr. Ludwig Mathey

INSTITUT FÜR LASERPHYSIK
UNIVERSITÄT HAMBURG
OKTOBER 2014

Abstract

We probe in-situ phase fluctuations in a two-dimensional trapped Bose gas to locally study the Berezinskii–Kosterlitz–Thouless transition. We gain access to local phase fluctuations by performing a short expansion of the cloud. During expansion phase fluctuations transform into density fluctuations. We analyse spatial density correlations in expanded clouds to probe the decay of phase correlations. Our high-resolution imaging setup allows to restrict the evaluation of correlations to regions in the trapped cloud with a certain density. In the central high-density area of the cloud we find evidence for the algebraic decay of phase correlations. In the outer low-density area of the cloud phase correlations decay quickly on a short length scale. We determine the critical phase space density that marks the transition to algebraically decaying phase correlations. A comparison with recent theoretical studies enables us to extract the algebraic scaling exponent over a wide range in phase space density. Using local values of the scaling exponent, we reconstruct the local superfluid density of a two-dimensional Bose gas. Our evaluation scheme is tested using simulated density distributions with imprinted correlations.

In a separate set of measurements, we measure the critical velocity in the BEC-BCS crossover. We stir an ultracold ${}^6\text{Li}$ gas with a small attractive potential moving with a certain velocity. Above a critical velocity heating is observed. We determine the critical velocity for various interparticle interaction strengths and compare our results to the speed of sound, which we measure in the same sample. We excite an outward travelling sound wave by creating a local density perturbation in the center of a cloud. In the BEC regime, our results for the critical velocity are supported by numerical simulations.

In another endeavor, we measure the speed of sound v_s in a two-dimensional Fermi gas in the BEC-BCS crossover. We excite an outward travelling sound wave by creating a local density perturbation in the center of a cloud. We track the distance between cloud center and density maximum after various delay times to obtain the speed of sound. We prepare clouds in the interaction parameter range $\ln(k_F a_{2D}) \approx -1.5$ to 1.5 and compare our results for v_s to values obtained from the derivative of the equation of state $v_s^2 = 1/m \cdot \partial P / \partial n$. The pressure equation of state $P(n)$ is obtained from in-situ absorption images of the density distribution n . We see excellent agreement between the two approaches providing a link between static and dynamic behaviour of strongly-interacting two-dimensional Fermi gases.

Zusammenfassung

Wir untersuchen in-situ Phasenfluktuationen in einem zweidimensionalen Bosegas, um den Berezinskii–Kosterlitz–Thouless Übergang lokal zu charakterisieren. Wir extrahieren lokale Phasenkorrelationen durch eine kurze Expansion des atomaren Gases. Während der Expansion werden Phasenfluktuationen in Dichtefluktuationen sichtbar. Wir werten räumliche Dichte-Korrelationen in expandierten Wolken aus, um auf den Zerfall von Phasenkorrelationen zu schließen. Ein Abbildungssystem mit hoher räumlicher Auflösung ermöglicht die Auswertung von Dichte-Korrelationen in Bereichen der Wolke mit einer bestimmten Dichte. Im Zentrum der Wolke mit hoher Dichte finden wir einen Hinweis auf den algebraischen Zerfall von Phasen-Korrelationen. Im äußeren Teil der Wolke mit niedriger Dichte zerfallen Phasen-Korrelationen auf kurzen Längenskalen. Wir bestimmen die kritische Phasenraumdichte, die den Übergang zu algebraisch abfallenden Phasen-Korrelationen markiert. Durch den Vergleich mit einer aktuellen theoretischen Arbeit können wir den Exponenten des algebraischen Abfalls über einen großen Bereich in der Phasenraumdichte bestimmen. Aus der Dichteabhängigkeit des Exponenten rekonstruieren wir die lokale suprafluide Dichte eines zweidimensionalen Bosegases. Das Auswerteschema wird mittels simulierter Testverteilungen mit aufgeprägten Korrelationen getestet. In einem weiteren Experiment bestimmen wir die kritische Geschwindigkeit v_c im BEC-BCS Übergang. Wir rühren mit einem attraktiven Potential mit einer gewissen Geschwindigkeit in einem ultrakalten ^6Li Gas. Oberhalb einer kritischen Geschwindigkeit beobachten wir das Einsetzen eines Hitzeintrags in das System. Wir bestimmen die kritische Geschwindigkeit für verschiedene Wechselwirkungsstärken und vergleichen unsere Ergebnisse mit der Schallgeschwindigkeit, die wir im gleichen Gas bestimmen. Durch eine lokale Dichtestörung wird im Zentrum der Wolke eine Dichtewelle angeregt, die sich mit der Schallgeschwindigkeit nach außen bewegt. Unsere Ergebnisse für v_c im BEC Bereich werden durch numerische Simulationen unterstützt. In einem weiteren Experiment, messen wir die Schallgeschwindigkeit v_s in einem zweidimensionalen Fermigas im BEC-BCS Übergang. Wir regen im Zentrum der Wolke durch eine lokale Dichtestörung eine Schallwelle an und messen die Distanz zwischen Dichtemaximum und Zentrum nach verschiedenen Zeiten, um v_s zu erhalten. Wir preparieren Wolken für verschiedene Werte des Wechselwirkungsparameters $\ln(k_F a_{2D}) \approx -1.5$ bis 1.5 und vergleichen unsere Ergebnisse jeweils mit der Schallgeschwindigkeit, die wir aus der Ableitung der Zustandsgleichung erhalten $v_s^2 = 1/m \cdot \partial P / \partial n$. Die Dichte-Zustandsgleichung $P(n)$ bestimmen wir aus der in-situ Dichteverteilung n für die jeweiligen Wechselwirkungsparameter. Die Ergebnisse beider Methoden stimmen sehr gut überein und bestätigen den Zusammenhang zwischen statischem und dynamischem Verhalten eines stark wechselwirkenden zweidimensionalen Fermigases.

Contents

1	Introduction	9
2	Strongly interacting two-dimensional Fermi gases	11
2.1	Creation of an ultracold quantum gas	12
2.2	Preparation of a single two-dimensional layer	15
2.3	Strong interactions in two dimensions	17
3	Local probing of the Berezinskii-Kosterlitz-Thouless transition in a two-dimensional Bose gas	21
3.1	The BKT transition in a 2D Bose gas	22
3.1.1	Universal phase transitions	22
3.1.2	Mechanism and phenomenology of the BKT transition	24
3.1.3	The BKT transition in a trapped 2D Bose gas: Just an ordinary BEC after all?	27
3.2	Revealing in-situ phase fluctuations after short time of flight	31
3.2.1	Understanding the connection between phase fluctuations and density fluctuations	34
3.2.2	Density dependence of phase correlations	37
4	Extracting the algebraic scaling exponent	39
4.1	Methods	39
4.1.1	Measurement procedure	39
4.1.2	Temperature and condensate fraction	40
4.1.3	Local evaluation of correlations	42
4.1.4	Testing the evaluation scheme	45
4.1.5	Other influences to measured correlations	48
4.2	Results	52
4.2.1	Critical point of the BKT transition	52
4.2.2	Revealing the algebraic decay of phase correlations	54
4.3	Summary and outlook	60
5	The critical velocity in the BEC-BCS crossover	62
6	The speed of sound in a strongly-interacting 2D Fermi gas	69

1 Introduction

A paradigm in modern physics is the reduction of complex phenomena to fundamental laws. However, just because we know the microscopic laws that govern a system at the single-particle level we cannot in general start from those laws and predict the behaviour of many interacting particles [1]. Among others, the observation of Mott insulators [2], heavy-fermion superconductors [3], high-temperature superconductors [4] and the fractional quantum hall effect [5] revealed that interactions can trigger a collective behaviour that is more than the sum of its parts. While the fundamental quantum-mechanical laws of interacting electrons at the single particle level are well-established the description of strongly correlated quantum-many body systems remains one of the biggest challenges in contemporary physics [6, 7]

Most experimental studies of condensed matter systems probe excitations or macroscopic observables like the conductivity to find evidence for the microscopic origin of a phenomenon. Ultracold quantum gases provide the unique possibility to probe the quantum mechanical state itself by analysing correlations in quantum fluctuations [8].

Of special interest is the phase transition to a superfluid in a two-dimensional (2D) system. While the Mermin-Wagner-Hohenberg (MWH) theorem rules out any long-range phase coherence in 2D [9, 10], 2D systems can still be a superfluid. Berezinskii, Kosterlitz and Thouless (BKT) revealed that the formation of bound vortex-antivortex pairs prevents the rapid decay of phase correlations [11, 12]. In their ground-breaking work they proposed a direct link between the superfluid density and the form of the decay of phase correlations.

The BKT transition in an ultracold 2D Bose gas was first observed by Hadzibabic et al. [13]. They analysed the density distribution of two interfering condensates to probe the decay of phase correlations. Their experiment was only sensitive to global properties of the gas and did not provide local information about the decay of phase correlations. While first studies of local phase fluctuations in 2D Bose gases were already performed [14], the algebraic decay of phase correlations could not be observed so far.

Here, we probe in-situ phase correlations in a strongly interacting 2D Bose gas. We extract local information about phase correlations by performing a short time of flight. During expansion phase fluctuations transform into density fluctuations. We measure local density-density correlations to access the local decay of phase correlations. Our measurement opens the opportunity to probe the BKT transition locally. We find clear evidence for the predicted algebraic decay of phase correlations in the superfluid phase of a 2D Bose gas. A quantitative analysis of

the local decay of phase correlations allows us to determine the algebraic scaling exponent over a wide range in phase space density. The scaling exponent decreases significantly with increasing density. Values of the scaling exponent allow us to reconstruct the local superfluid density of a trapped 2D Bose gas. The study constitutes an important step to test the connection between phase correlations and superfluidity in two-dimensional systems.

In a separate endeavor, we probe the stability of superfluids against external perturbations in the BEC-BCS crossover [15]. A small attractive potential is dragged through an ultracold gas of ${}^6\text{Li}$ with a certain velocity. Above a critical velocity we observe the onset of heating. According to the Landau criterion the critical velocity is directly connected to the excitation spectrum of the system. We compare our results for the critical velocity to the speed of sound which we measure in the BEC-BCS crossover. We observe significant deviations from Bogoliubov theory which predicts that speed of sound and critical velocity should match in the BEC regime. Our results for the critical velocity are supported by numerical simulations carried out in the BEC regime.

In another endeavor, we measure the speed of sound in a 2D Fermi gas in the BEC-BCS crossover. We excite an outwards travelling density wave in the cloud's center and measure its propagation speed for different interaction strengths. The sound wave is excited by a local density perturbation using a red-detuned tightly focused dipole trap. As a comparison, we determine the equation of state of a 2D Fermi gas in the BEC-BCS crossover by analysing in-situ density distributions. Derivatives of the equation of state enable an alternative method to determine the speed of sound. We observe excellent agreement between the static and dynamic approach. Our measurements give insight in the dynamic behaviour of strongly interacting Fermi gases, which previously generated surprising results [16,17]. Similarly to our measurements in 3D, the speed of sound in 2D will serve as a reference for future studies of the critical velocity in a 2D Fermi gas.

All the experiments described here were performed in the group of Prof. Henning Moritz. The studies rely on an experimental apparatus which was built over the last years by the PhD students Wolf Weimer and Kai Morgener. During the construction phase, Jonas Siegl and later Klaus Hueck joined the group as PhD students. While I contributed to many parts of our work on the speed of sound in 3D and 2D, our results are only briefly presented in chapter 5 and chapter 6 of this thesis. The measurement of the critical velocity in the BEC-BCS crossover is described in detail in the PhD thesis by Wolf Weimer [18]. The measurement of the speed of sound in 2D will be described in detail in the PhD thesis by Kai Morgener [19].

Intrigued by the appearance of density ripples in a 2D Bose gases after short expansion, I dedicated the last two months of my work as a Master student to understand and analyse these density patterns. I am happy that the analysis of spatial density correlations in expanded 2D Bose gases turned out to be so rich that I can report our results in detail in chapter 3 and 4 of this thesis.

2 Strongly interacting two-dimensional Fermi gases

Two-dimensional quantum systems offer a variety of fascinating quantum-many body effects [20]. The discoveries of superfluidity in liquid helium films [21], the fractional quantum hall effect [5], high-temperature superconductivity [4] and massless Dirac fermions in graphene [22] are only a few examples of the rich phenomena encountered in two-dimensional systems. All of these phenomena were observed in the context of macroscopic liquids or solids, where it can be hard to extract the fundamental origin of the effect due to the complexity of compounds, defects and little controllability over microscopic details. Further, it is impossible to prepare isolated low-dimensional materials as they always need a substrate or compound for stability.

The interaction between laser light and atoms enables the controlled creation, manipulation and detection of isolated low-dimensional quantum systems. Using magnetic fields and specifically tailored optical potentials one can simulate physical systems with tunable interactions ranging from lattice structures in solids [23] to the effect of strong magnetic fields [24]. The ground-breaking experiment which showed that quantum gases can be used as versatile *quantum simulators* was the observation of the quantum phase transition¹ from a superfluid to a Mott-insulator [26,27]. In our experiment, we prepare an ultracold two-dimensional Fermi gas of ${}^6\text{Li}$. By exposing the gas to a magnetic field we can tune interactions between atoms in a wide range. Microscope objectives allow local manipulation and probing of the quantum gas with a resolution approaching the interparticle distance. Thereby, we can gain information about microscopic details of quantum-many body phenomena in two dimensions.

Here, I will first give a short overview of the main steps to prepare an ultracold quantum gas. I will then sketch how we prepare and characterise a single two-dimensional layer of ${}^6\text{Li}$ atoms. Finally, I will conclude by giving a short introduction to the properties which distinguish strongly interacting 2D quantum gases from their counterparts in 3D. The overview given in this section is far from being complete². A detailed description of our experimental setup can be found in the recent PhD thesis by Wolf Weimer [18] and the PhD thesis by Kai Morgener [19] which is in preparation.

¹In contrast to regular phase transitions, a quantum phase transition occurs at zero temperature and is driven by quantum fluctuations. A detailed description can be found in Ref. [25]

²An overview of the creation of ultracold Fermi gases is given in Ref. [28]. An overview of the simulation of quantum-many body phenoma with quantum gases is given in Ref. [20].

2.1 Creation of an ultracold quantum gas

The development of laser cooling starting in the late 1970s opened the possibility to cool an atomic gas down to temperatures where its quantum nature becomes relevant [29–31]. As first demonstrated in the ground-breaking works at MIT and JILA in 1995 [32, 33], below a critical temperature bosonic ^{87}Rb atoms can form a new state of matter: a Bose-Einstein condensate. Our experimental setup uses fermionic ^6Li atoms, which due to the Pauli exclusion principle cannot condense but form a degenerate Fermi gas. One of the biggest appeals of ^6Li is its tunability of interactions. By exposing the atomic cloud to a magnetic field one can facilitate a so called Feshbach-resonance to tune interactions between atoms over a wide range as first shown for a BEC in [34]. The first degenerate Fermi gas with ultracold atoms was realised in the group of Deborah Jin in 1999 [35]. Using a Feshbach resonance they [36] and the group of Rudolf Grimm [37] demonstrated in 2003 that fermionic ^{40}K atoms can form bosonic molecules which in turn condensed to a BEC. The formation of a molecular BEC of ^6Li dimers was demonstrated in the following year [38]. Here, I will briefly sketch how we reach a molecular BEC in our experimental setup.

The overall process to create an ultracold quantum gas of ^6Li with our setup lasts about 10 s and includes multiple stages which are precisely timed and coordinated. Figure 2.1 shows an overview of our experiment. In general, the preparation of atomic gases is extremely sensitive to external perturbations and requires a complete isolation from the environment. The process therefore takes place inside an ultra-high vacuum system reaching pressures as low as 1×10^{-11} mbar. The source of ^6Li atoms is a chunk of Lithium which is heated inside an oven to temperatures of about 400°C . The atoms leaving the oven form a collimated beam which is directed towards the first cooling stage of our setup: the Zeeman slower. Here, the fast thermal atoms leaving the oven are decelerated by a counterpropagating light beam. To maintain resonance between the laser beam and atoms over a larger range of atom velocities we use an inhomogeneous magnetic field in propagation direction. The magnetic field compensates the velocity dependent Doppler shift of decelerated atoms through the Zeeman shift of atomic levels.

The decelerated beam enters the next stage of our cooling scheme: a magneto-optical trap (MOT). Here, the atoms are trapped and cooled through a combination of magnetic gradient fields and three pairs of counterpropagating laser beams. At this stage we expect the cloud's temperature to be on the order of the so-called Doppler temperature $T \approx 140 \mu\text{K}$, which is determined by the linewidth of the addressed atomic transition in ^6Li ³.

In a next step, we compress the cloud and transfer it to a large volume trap formed by a red-detuned standing wave inside an optical resonator. By ramping down the intensity of both resonator beams we perform the first evaporation inside multi-

³Zeeman slower and MOT address the D2 transition of ^6Li . We could also address the D1 line to create a *gray molasses* which promises temperatures below the Doppler limit [40].

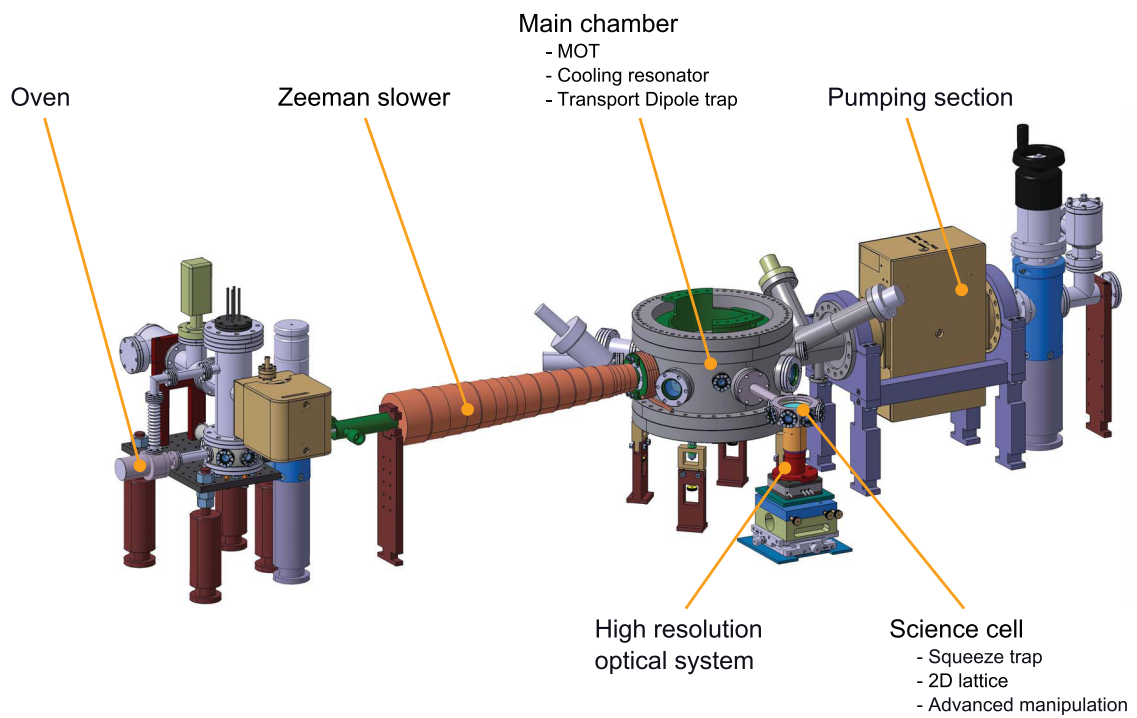
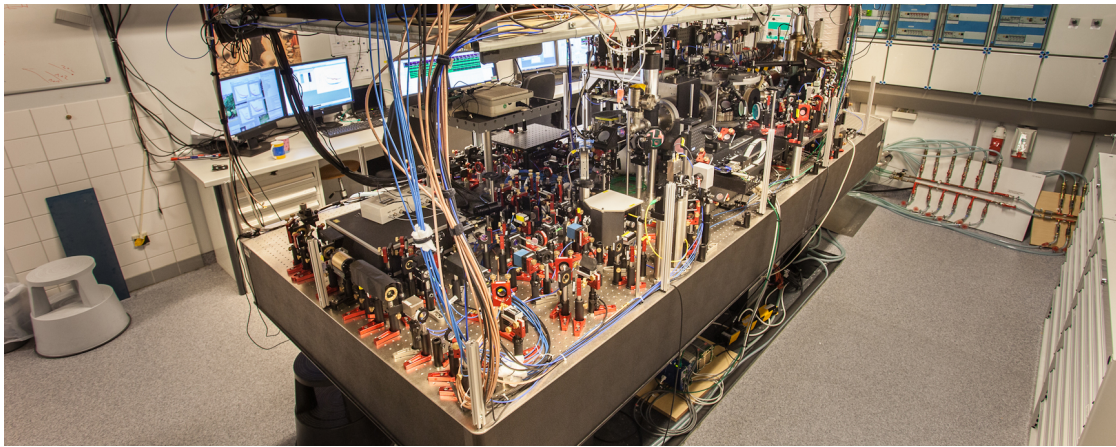


Figure 2.1: Overview of the experimental apparatus to create an ultracold Fermi gas of ${}^6\text{Li}$. Top panel: Picture of the experimental setup as of October 2013, reprinted from [39] Bottom panel: Schematic drawing of the main stages to prepare and probe and ultracold ${}^6\text{Li}$ gas as explained in the text, reprinted from [18].

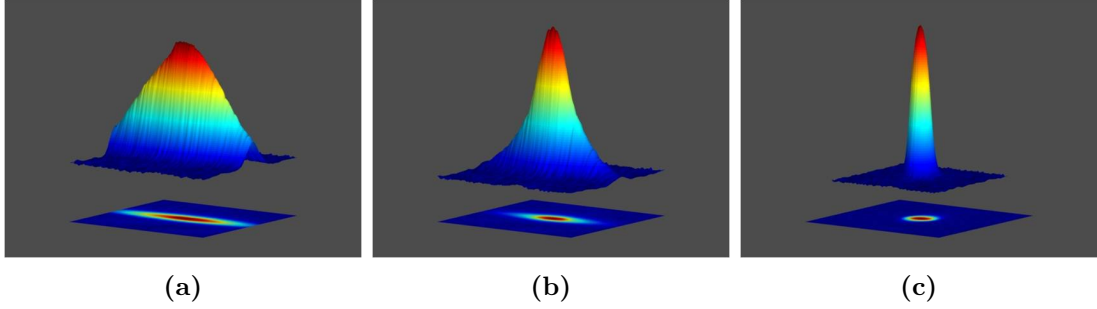


Figure 2.2: Formation of a molecular BEC of ${}^6\text{Li}$ dimers. A non-degenerate gas of ${}^6\text{Li}$ atoms is trapped inside the focus of a red-detuned transport beam (a). We evaporatively cool the gas by ramping down the intensity of the transport beam while applying a magnetic field $B = 832$ G. By ramping the magnetic field to lower values, ${}^6\text{Li}$ atoms form bosonic dimers which condense to a molecular BEC, clearly visible in the bimodal density distribution (b,c).

ple maxima of the standing wave⁴. After evaporation the atoms are transported from the main chamber to the science cell which provides excellent optical access required for our envisaged experiments. The transport is realised inside the focus of another far red-detuned dipole trap. We shift the beam's focus and thereby move the atomic cloud from the resonator position to the science cell. Inside the science cell the atoms form a cigar shaped cloud whose form is determined by the intensity distribution inside the focus of the transport beam. At this point we achieve atomic clouds containing a few 10^5 atoms with a temperature still too high for quantum degeneracy. We therefore perform another evaporation step in which the intensity of the transport beam is ramped down. Thereby, we loose the hottest atoms while the rest of the cloud rethermalises. The process of thermalisation is greatly enhanced at a Feshbach resonance where the scattering rate between atoms is increased significantly. We approach a Feshbach resonance of ${}^6\text{Li}$ by ramping the magnetic field to values of around $B = 832$ G [41]. After evaporation we can ramp the magnetic field to lower values where ${}^6\text{Li}$ forms bosonic dimers. As shown in Fig. 2.2 we observe a clear bimodal density distribution indicating the phase transition to a molecular BEC⁵. The condensation of ${}^6\text{Li}$ dimers indicates that we have achieved the prerequisite for the following experiments in two dimensions: a quantum-degenerate Fermi gas. The next section will explain how we squeeze the three-dimensional atomic cloud to a thin two-dimensional layer.

⁴Originally, it was intended to transport the cloud inside the maxima of the standing wave to the focal plane of the resonator beams. Here, a more efficient evaporation inside the running wave of one of the resonator beams would have been possible. This scheme was not adopted due to parametric heating during the transport.

⁵In the local density approximation, the density of a BEC follows the harmonic trapping potential, whereas the distribution of thermal atoms is described by a Gaussian function.

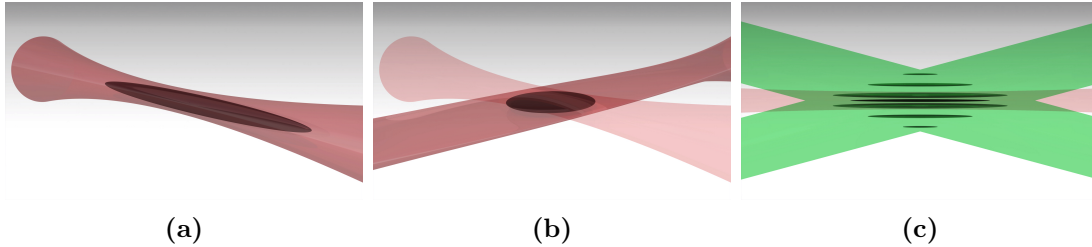


Figure 2.3: Illustration of the preparation of a single two-dimensional layer. We transfer the 3D Fermi gas from a cigar shaped transport beam (a) to a pancake-shaped red-detuned dipole trap (b). After compression inside the pancake trap the atoms are transferred into the single layer of a blue-detuned optical lattice (c). Reprinted from [18].

2.2 Preparation of a single two-dimensional layer

The preparation of a clean two-dimensional atomic sample is a technically challenging task. In solids one always needs a substrate or compound material to stabilise the system. In ultracold quantum gases one has the unique possibility to achieve isolated 2D quantum systems by using a tight optical confinement in one direction of the atomic cloud. While the first two-dimensional atomic gases could already be realised with bosons [42, 43] and fermions [44, 45] about 10 years ago, the preparation and verification of isolated layers remains a technical challenge. Two-dimensional systems require a tight confinement which can be realised by using dipole traps with a high trap-frequency aspect ratio [46], a blue-detuned TEM_{01} mode [47] or a one-dimensional optical lattice [13]. While optical lattices due to small lattice spacings of a few μm are best suited to create 2D systems it is in general hard to resolve and load individual sites. The first direct observation of a 2D ultracold Fermi gas revealed multiple occupied lattice sites [48]. Here, we employ a two-step loading procedure similar to that in [49] that allows for a reliable preparation of single 2D layers of ${}^6\text{Li}$ with negligible occupancy of neighbouring lattice sites. The experimental setup was built up and successfully implemented by Klaus Hueck in the framework of his Master’s thesis [39].

In the first step of the loading procedure, the atomic cloud is transferred from the cigar-shaped transport beam to a pancake-shaped dipole trap as shown in Fig. 2.3a. After a final evaporation step inside the pancake trap, we can achieve around 2×10^4 to 3×10^4 atoms⁶ with a condensate fraction deep in the BEC regime of about 90%. Due to the relatively high trap-frequency aspect ratio $\omega_z/\omega_r \approx 40$ of the pancake trap and the weak magnetic confinement in radial direction, we can squeeze the atomic cloud in z-direction by increasing the beam intensity. The expected Thomas-Fermi-radius of the squeezed cloud should be on the order of $1 \mu\text{m}$ in z-direction for a beam power of $P \approx 1 \text{ W}$. This allows us to transfer the cloud into a single layer of a repulsive blue-detuned one-dimensional optical lattice

⁶All atom numbers given in this thesis refer to the atom number per spin state. This number coincides with the atom number obtained from absorption images over the BEC-BCS crossover.

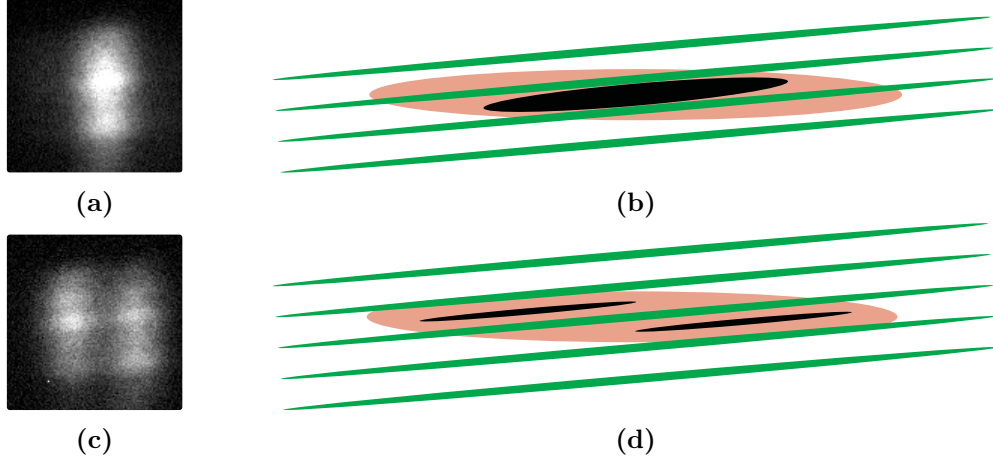


Figure 2.4: Verification of the creation of a single two-dimensional layer. The symmetry axis of red-detuned pancake trap (red) and blue-detuned optical lattice (green) do not coincide (b,d). Depending on the position of the pancake trap in axial direction we load a single (b) or two (d) 2D layers. Imaging along axial direction reveals the loading of a single (a) and two (c) 2D layers. Reprinted from [18].

as shown in Fig. 2.3c. The lattice is formed by two laser beams with wavelength $\lambda = 532\text{ nm}$ which interfere under an angle of 10.4° resulting in a lattice spacing of $d \approx 2.9\ \mu\text{m}$. After loading into a single layer, the pancake trap is slowly ramped down and the cloud remains trapped between the intensity maxima of the repulsive lattice. The trapping in radial direction is ensured by a weak magnetic trap with frequency $\omega_r \approx 2\pi \cdot 30\ \text{Hz}$. The strong lattice confinement $\omega_z \approx 2\pi \cdot 25\ \text{kHz}$ compared to the weak radial confinement results in a very high aspect ratio $\omega_z/\omega_r \approx 830$. In general, a system is called two-dimensional when only the ground state of the harmonic oscillator in axial direction is occupied. Assuming the Fermi energy E_F of a non-interacting system we achieve a ratio

$$\frac{E_F}{\hbar\omega_z} = \frac{\hbar\omega_r\sqrt{2N}}{\hbar\omega_z} = \frac{\omega_r}{\omega_z}\sqrt{2N} \approx 0.2 \quad (2.1)$$

for a particle number of $N = 3 \times 10^4$. Therefore, the occupation of excited state in axial direction is heavily suppressed for low temperatures and the gas can be treated as 2D. As shown in Fig. 2.3c the loading into a single lattice site only works when the pancake trap is aligned with a minimum of the optical lattice. Therefore, the procedure described above greatly depends on the relative position between the two traps. Using piezo actuated mirrors we can shift the axial position of the pancake trap with respect to the lattice. But how do we determine its optimal position? In contrast to the experiment described in Ref. [48] our imaging setup along the radial cloud direction does not provide sufficient resolution to resolve neighbouring lattice sites. In principle, one would expect a difference in radial cloud size when loading into one or multiple layers, but this method did not provide reliable results. Surprisingly, the answer in our case is provided by a misalignment. The symmetry

axis of the pancake trap does not coincide with the symmetry axis of the lattice, but is tilted by a few degrees as shown in Fig. 2.4. By imaging along the axial direction we can directly detect the number of occupied layers and adjust the axial position of the pancake trap accordingly. Absorption images in Fig. 2.4a show that we observe no significant occupancy of neighbouring lattice sites when loading into a single layer. Our resolution here is only limited by the thermal wings of the 2D cloud which overlap with neighbouring sites when imaged in axial direction. In the case of other occupied sites one would expect a bump on the thermal wings, which is not observed here. We have therefore prepared and verified the deterministic preparation of a single two-dimensional layer of a strongly interacting Fermi gas.

2.3 Strong interactions in two dimensions

Probably the most fascinating phenomena in nature are those which are not yet understood. While many poorly understood phenomena in high-energy physics enjoy great theoretical dedication, there is often a lack of experimental input to test theories against. Strongly interacting two-dimensional quantum gases are an example of a fruitful interplay between the development of new theoretical approaches and direct experimental input. Here, I will explain a few aspects why the world of strong interactions in two dimensions is worth exploring.

One of the most universal tools in physics is the solution of a complicated complex problem by reducing it to a simple problem with known solution. Starting from the simple solution one can then step-by-step estimate the effect of the simplifications to approximate the solution to the complicated problem. One prime example of this method is perturbation theory. In perturbation theory one describes an interacting system by reducing it to a well-understood non-interacting system. The effect of interactions are then treated as a perturbation of the non-interacting system which are step-by-step added to the solution. This treatment forms the basis of a large part of our understanding of physical phenomena. In the context of condensed matter systems, a perturbative treatment led to the fundamental results of Fermi liquid theory where interacting systems can effectively be described as non-interacting systems with renormalised parameters [50, 51]. In strongly correlated quantum systems this method usually breaks down. Here, the non-interacting system is not a good reference point anymore and non-perturbative approaches [52, 53] or computationally demanding Quantum Monte Carlo studies [54] are required. Recent measurements of the equation of state in a strongly interacting 3D Fermi gas are a beautiful example of the invaluable input experiments with ultracold quantum gases can deliver to test newly developed theoretical approaches [55].

Not only strong interactions, but also the reduction of dimension has dramatic effects on the description of a quantum system. There are several exciting predictions of phenomena in two dimensions covering high-temperature superconductivity [7], quasi-particles with non-abelian statistics [56] and fault-tolerant quantum computers [57]. While there is great ongoing effort to realise these systems with cold

atoms, they require atomic gases with extremely low temperatures or entropies which are currently out of reach. Here, I will focus on the more basic question what we mean by strong interactions in a 2D quantum gas, before giving a short introduction to the peculiarities of phase transitions in 2D which will be covered in more detail in the next chapter.

As already mentioned in section 2.1, the broad Feshbach resonance of ${}^6\text{Li}$ allows us to control interactions between atoms. More precisely, we can tune the 3D scattering length a_{3D} which determines the mean field interaction strength g between ${}^6\text{Li}$ atoms of mass m :

$$g = \frac{4\pi\hbar^2 a_{3D}}{m}. \quad (2.2)$$

When we prepare a two-dimensional gas in a tight axial confinement, we introduce another length scale which influences scattering and thereby interactions in our system. The relevant length scale is the harmonic oscillator length $l_z = \sqrt{\hbar/m\omega_z}$ which determines the extent of the ground-state wave function in a trap with frequency ω_z . Most experiments in 2D Bose gases were performed in the weakly interacting regime where $a_{3D} \ll l_z$. In the weakly interacting limit the 2D interaction strength can be expressed by a dimensionless⁷ quantity [59]

$$\tilde{g} = \sqrt{8\pi} \frac{a_{3D}}{l_z}. \quad (2.3)$$

Only recently the regime of strong interactions in 2D where $g > 1$ has become accessible [49, 60–62]. Here a_{3D} is on the order of l_z and the coupling strength in eq. 2.3 needs to be replaced by a density dependent expression. This is in sharp contrast to the interaction parameter 2.2 which remains density independent for all values of a_{3D} . The analysis by Petrov et al. [63] revealed that scattering in this regime can be described just as in a pure 2D system, where microscopic scattering is still 3D. Moreover, the Feshbach resonance of ${}^6\text{Li}$ allows us to reach a regime where a_{3D} greatly exceeds l_z and the microscopic nature of scattering changes from 3D to 2D [64].

Finally, I will turn to some aspects of phase transitions in 2D. In a 3D system the transition to a BEC can be described by some macroscopic wavefunction Ψ , which is associated with long-range phase coherence. Bose-Einstein condensation in 3D might be a quantum-mechanical effect but its description with a scalar wave function does not require any treatment in terms of quantum operators. In other words: a mean-field description which ignores any quantum fluctuations is justified. This approximation breaks down in 2D, where fluctuations are necessary to describe the quantum state of the system. The presence of fluctuations might

⁷It turns out that the dimensionless coupling strength in combination with the underlying $\mathcal{SO}(2,1)$ symmetry of the Hamiltonian results in scale invariance of weakly interacting Bose gases for all temperatures. Hung et al. [58] and Yefsah et al. [59] revealed scale invariance for coupling strengths $g < 1$ by showing that the scaled density $n\lambda_T^2$ and its fluctuations are a function of the ratio μ/T instead of the chemical potential μ and temperature T separately.

suggest that no long-range order and therefore no Bose-Einstein condensation can occur. Surprisingly, despite fluctuations a 2D system can show superfluidity as was first observed in liquid helium films [21] and recently demonstrated in a 2D Bose gas [65]. Due to fluctuations the phase transition to a superfluid does not involve a broken symmetry or long-range ordering but is characterised by a very subtle change in the decay of phase correlations.

In the following chapters 3 and 4 we will describe, how we can access this subtle change in phase correlations to probe the BKT transition in a 2D Bose gas.

3 Local probing of the Berezinskii-Kosterlitz-Thouless transition in a two-dimensional Bose gas

Phase transitions are one of the most profound manifestations of a system's collective behaviour. As temperature, density or interactions are changed materials can suddenly freeze, vaporise, magnetize or even become superconducting. Each phase transition is associated with the occurrence of a certain type of order or coherence, which is usually connected to a broken symmetry. When the temperature in a 3D Bose gas is lowered below a critical value, the system breaks its $\mathcal{U}(1)$ -symmetry by picking a global phase and becomes long-range phase coherent.

In a 2D system the Mermin-Wagner-Hohenberg (MWH) theorem rules out the occurrence of a spontaneously broken symmetry [9,10]. However, Berezinskii, Kosterlitz and Thouless (BKT) pointed out that there can still exist a certain degree of coherence via the formation of bound vortex-antivortex pairs [11,12]. In contrast to second-order phase transitions in 3D, the BKT transition is not characterised by any broken symmetry but only a qualitative change in the decay of phase correlations. While the decay of phase correlations prevents the occurrence of true-long range order in 2D the system can still be a superfluid.

The analysis of correlations provides a powerful tool to gain insight into fundamental properties of quantum systems [8]. The landmark experiment performed by Hanbury Brown and Twiss used noise correlations of a distant light source to probe the nature of the light field [66]. In the context of cold atoms noise correlations were used to study the pairing of fermions [67], ordering in optical lattices [68,69] and (anti-)bunching of bosonic (fermionic) atoms [70–72]. The analysis of phase correlations is difficult because the local phase of an atomic cloud is not directly accessible from absorption images. In the experiment performed by Hadzibabic et al. [13] the BKT transition was revealed by interfering two independent 2D Bose gases as suggested by Polkovnikov et al [73]. Their experiment provided evidence for quasi long-range order and the microscopic mechanism of the transition, but did not provide local information about the decay of phase correlations. First local studies of phase fluctuations in 2D Bose gases were reported in Ref. [74] and Ref. [14]. So far, no experimental studies are available which probe the predicted connection between the decay of phase correlations and the superfluid density.

Here, we are performing the first local studies of the BKT transition. We probe local phase correlations in a strongly interacting two-dimensional Bose gas by performing a short expansion of the cloud. During the expansion phase fluctuations are transformed into density fluctuations by free time evolution. The local analysis of spatial density correlations allows us to distinguish between regions in the cloud with exponentially and algebraically decaying correlations. By performing a quantitative comparison with recent theoretical predictions [75] we gain access to the algebraic scaling exponent which is directly connected to the superfluid density. Since the overall density of the cloud does not deviate significantly from its original distribution for short expansion times we are able to compare the derived superfluid density to the total density of a two-dimensional Bose gas.

3.1 The BKT transition in a 2D Bose gas

Due to the absence of true long-range order it is puzzling that there exists a phase transitions in 2D at all. It turns out that the transition and the associated order is much more subtle than in 3D. In this section we will briefly review fundamental concepts of second order phase transitions to explain how we can understand and classify the BKT transition in a strongly interacting 2D Bose gas.

3.1.1 Universal phase transitions

Phase transitions are omnipresent in nature. They range from the transition between liquid, gaseous and solid phases over the magnetisation of solids to more exotic quantum phase transitions which are only driven by quantum fluctuations. Despite their diverse nature most transitions can be described very accurately within the same framework of *Statistical Mechanics*. Remarkably, systems close to a phase transition behave completely independent of their microscopic details but only according to their *universality class* determined by very general properties like dimension, symmetry and the type of interactions.

One of the main quantities to characterise a phase transition is the (*local*) *order parameter* $\Psi(\mathbf{r})$, which quantifies (local) ordering in the system. Most easily understood is the case of a second-order phase transition in which the order parameter changes in a continuous but not-differentiable way at the critical point.

An illustrative example of this type of transition is the spontaneous magnetisation of ferromagnets. Here the local order parameter describes the local magnetisation of the system $\Psi(\mathbf{r}) = S(\mathbf{r})$. As the temperature is lowered towards a critical value T_c , microscopic domains are forming where all the spins are pointing in the same direction¹. However, there is no correlation between individual domains and therefore no net magnetisation of the solid. As the temperature is further decreased,

¹In the theory of phase transition the order parameter $\Psi(\mathbf{r})$ is just a classical scalar function. While the terminology of *spins* might suggest a quantum-mechanical treatment, we simply treat spins classically rather than as operators.

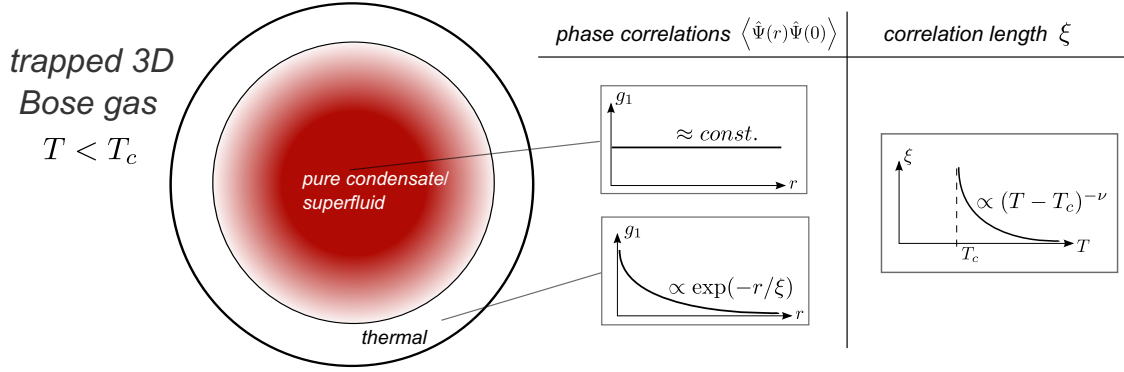


Figure 3.1: Phase correlations in a trapped 3D Bose gas. Below a critical temperature T_c a BEC forms in the center of a trapped 3D Bose gas. A 3D BEC is characterised by the occurrence of long range phase coherence $g_1(r) \approx \text{const.}$. In the thermal wings of the cloud phase correlations decay exponentially $g_1(r) \propto \exp(-r/\xi)$ on a length scale ξ . The correlation length ξ diverges with a universal critical exponent ν as the temperature is lowered from above towards T_c .

domains grow larger and reach the macroscopic size of the system at a critical temperature T_c . Here the system picks up a net magnetisation which continuously breaks the spin rotation symmetry. Since there are still various domains with different spin orientation at the critical point, the magnetisation does not jump to a finite value but continuously increases as the temperature is lowered below T_c . Further below T_c , the net magnetisation increases until it reaches its maximal value at $T = 0$.

Besides global properties like the overall magnetisation, phase transitions can be fully characterised by local correlations of the order parameter. The fundamental quantity to quantify correlations is the normalised two-point correlation function

$$g_1(\mathbf{r}, \mathbf{r}') = \frac{\langle \hat{\Psi}(\mathbf{r})\hat{\Psi}(\mathbf{r}') \rangle}{\langle \hat{\Psi}(\mathbf{r}) \rangle \langle \hat{\Psi}(\mathbf{r}') \rangle}, \quad (3.1)$$

which, in the context of a ferromagnet, measures the correlation between the spin orientation at position \mathbf{r} and another spin at position \mathbf{r}' . For $T < T_c$ the formation of domains of size ξ is captured in an exponentially decaying correlation function

$$g_1(\mathbf{r}, \mathbf{r}') \propto e^{-|\mathbf{r}-\mathbf{r}'|/\xi}. \quad (3.2)$$

We see from eq. 3.2 that spins within a single domain, i.e. $r = |\mathbf{r} - \mathbf{r}'| \ll \xi$, are well correlated and $g_1 \approx \text{const.}$ while correlations between individual domains, i.e. $|\mathbf{r} - \mathbf{r}'| \gg \xi$, decay very quickly and $g_1 \approx 0$. We will therefore refer to ξ as the *correlation length*. As we approach T_c from above, macroscopic domains are forming which is captured in a diverging correlation length

$$\xi \propto \frac{1}{(T - T_c)^\nu}. \quad (3.3)$$

with a universal critical exponent ν . At the critical point spin correlations decay algebraically without any characteristic length scale

$$g_1(r) \propto \frac{1}{r}. \quad (3.4)$$

Below the critical temperature $T < T_c$ magnetic domains stretch over the whole system. We therefore have long-range magnetic order and the correlation function remains constant over the system size.

The qualitative features described above are a general property of second-order phase transitions and can be applied to describe the transition to a 3D BEC as well. Just like the net magnetisation of a 3D ferromagnet, the total particle number of condensed atoms increases continuously as we cool the Bose gas below a critical temperature T_c . In a 3D BEC the local order parameter is the condensate wavefunction $\Psi(\mathbf{r}) = \sqrt{n(\mathbf{r})}e^{i\varphi}$ itself. Similarly to magnetic domains with a common spin orientation, a 3D BEC picks a global phase and becomes long-range phase coherent. The connection between long-range coherence and condensation is directly visible in the Penrose-Onsager definition of the condensate density [76]:

$$n_c = \lim_{r \rightarrow \infty} \langle \hat{\Psi}(r)\hat{\Psi}(0) \rangle \quad (3.5)$$

The analogy between a 3D Bose gas and a 3D ferromagnet explained so far was based on common qualitative features. In general, quantitative details like the critical temperature or the correlation length depend on the microscopic details of the transition. While spontaneous magnetisation is driven by interactions between spins, a BEC is the result of a Bose gas reaching a critical phase space density. It is therefore very surprising that in a 3D Bose gas and a 3D ferromagnet the correlation length in eq. 3.3 diverges with the *same* critical exponent ν . This is an example of systems which fall into the same universality class².

The aim of this section was to introduce the basic phenomenology of second-order phase transitions in three-dimensional systems. We introduced the two-point correlation function g_1 and saw that the phase transitions to a 3D BEC and a 3D ferromagnet are associated with the occurrence of long-range order where the phase correlation function $g_1(r) \approx \text{const.}$

3.1.2 Mechanism and phenomenology of the BKT transition

The examples of spontaneous magnetisation and Bose-Einstein condensation in 3D systems might suggest that all phase transitions are naturally accompanied with some broken symmetry and long-range ordering. Consequently, the MWH-theorem would rule out the existence of any phase transition. It turns out that there can be phase transitions which *do not* break any symmetry of the system. The most

²Non-interacting BECs fall into the universality class of a Gaussian complex-field model, while any interactions in the BEC lead to the universality class of the 3D xy-model used to describe ferromagnets [77].

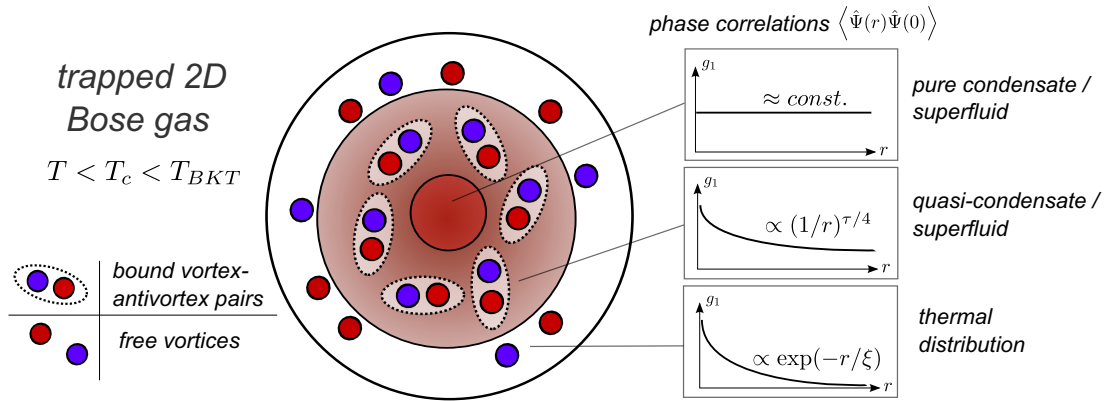


Figure 3.2: Phase correlations in a trapped 2D Bose gas. For sufficiently low temperatures $T < T_c$ phase fluctuations are suppressed and a pure BEC forms in the cloud’s center. Close to the center phase correlations decay algebraically $g_1(r) \propto (1/r)^{\tau/4}$ with a scaling exponent τ due to the formation of bound V-AV pairs. In the outer thermal region of the cloud free vortices can proliferate and phase correlations decay exponentially $g_1(r) \propto \exp(-r/\xi)$ on a length scale ξ .

prominent example for this surprising result is the BKT transition. Here, we will first give a short overview of the mechanism and phenomenology, before explaining in the next section how we can apply the ideas of the BKT transition to a 2D Bose gas. In parts, this section follows the treatment by Hadzibabic et al. [64], which gives an illustrative yet comprehensive introduction to the topic from an atomic physics perspective.

In their original work [11] Kosterlitz and Thouless studied the so called XY-model:

$$\mathcal{H} = -J \sum_{\langle ij \rangle} \cos(\varphi_i - \varphi_j) . \quad (3.6)$$

The Hamiltonian of eq. 3.6 describes spins on neighbouring lattices sites i, j , which interact through their relative in-plane spin orientation φ_i, φ_j . The sign of the coupling constant J determines whether a parallel ($J > 0$) or anti-parallel ($J < 0$) spin alignment is energetically favorable. Usually, one would expect that thermally activated phonons and vortices destroy any long-range phase ordering at temperatures $T > 0$ in 2D. However, Kosterlitz and Thouless revealed that below a certain temperature T_{BKT} vortices with opposite circulation can form stable vortex-antivortex (V-AV) pairs. These pairs disturb the phase on a length scale that is on the order of the vortex distance and do not qualitatively affect the long range behaviour of the system. It turns out that the existence of bound V-AV pairs only results in a *renormalisation* of the superfluid density n_s rather than completely destroying it. This results in the remarkable prediction that the superfluid density n_s directly determines the long-range decay of phase correlations. One can show that correlations decay *algebraically* for all temperatures $T < T_{BKT}$ as [75]

$$g_1(r) = \left(\frac{a^2}{a^2 + r^2} \right)^{\tau/8} , \quad (3.7)$$

with some scaling exponent $\tau = 4/(n_s\lambda_T^2)$, cutoff length a and thermal de Broglie wavelength $\lambda_T = 2\pi\hbar/\sqrt{2\pi m K_B T}$. In 3D systems, we encountered the algebraic decay of g_1 at the critical point of the phase transition. In 2D, the system remains critical for all temperatures $T < T_{BKT}$. Therefore, there is no long-range order and $g_1(r) \rightarrow 0$ for large distances r . However, as we will see below, phase correlations decay only very weakly since in general $\tau < 1$. Therefore, the BKT transition is associated with the occurrence of *quasi-long range order*.

As the temperature is increased, the size of vortex-antivortex pairs increases, which renormalises n_s to lower values and g_1 decays faster. When the temperature is further increased and reaches $T = T_{BKT}$ the formation of bound V-AV pairs is not energetically favorable anymore and free vortices can proliferate. This leads to the remarkable result that the superfluid density jumps from $n_s\lambda_T^2 = 4$ to 0 at the BKT transition point³. In the non-superfluid regime above T_{BKT} , free vortices can proliferate and g_1 decays exponentially

$$g_1(r) \propto e^{-r/\xi}, \quad (3.9)$$

where the correlation length diverges *exponentially*

$$\xi \propto \exp\left(\sqrt{\frac{T_{BKT}}{T - T_{BKT}}}\right) \quad (3.10)$$

when approaching T_{BKT} from above. This is in sharp contrast to the power law divergence in the 3D case from eq. 3.3 and basically a feature of an *infinite-order* phase transition, where no discontinuities in derivatives of the free energy are encountered.

The above section gave a short introduction to what makes a phase transition in 2D special. In sharp contrast to a second-order phase transition in a 3D system, the BKT transition in 2D is not connected with the occurrence of long-range order. The quantum state of the BKT phase does not break the symmetry of the Hamiltonian eq. 3.6 and can still show fluctuations in phase. Therefore, the transition cannot be described by a classical order parameter. Instead, the transition is characterised by a change in the form of the correlation function $g_1(r)$ from an exponential to an algebraic decay at the transition. The next section will explain how we can apply these ideas to the system we are interested in: a strongly interacting 2D Bose gas.

³This was shown using a *Renormalisation Group* analysis by Nelson et al. [78]. It can be understood by considering the energy $E = \hbar^2\pi n_s \ln(R/\xi)/m$ and entropy $S = 2k_B \ln(R/\xi)$ of a single vortex in a disk with radius R which results in the free energy:

$$F = E - TS = \frac{k_B T}{2} (n_s\lambda_T^2 - 4) \left(\frac{R}{\xi}\right) \quad (3.8)$$

At $n_s\lambda_T^2 = 4$, F changes sign which makes the system unstable against proliferation of free vortices and renormalises n_s to 0.

3.1.3 The BKT transition in a trapped 2D Bose gas: Just an ordinary BEC after all?

The occurrence of Bose-Einstein condensation in 3D can already be understood by considering a simple model of a non-interacting uniform Bose gas. The inclusion of a trapping potential and finite interactions might affect the phase quantitatively but does not change the mechanism of the transition. The situation changes dramatically in a 2D system. Here, a BEC is impossible in a non-interacting uniform Bose gas and only the effect of finite interactions or a trapping potential enable the existence of a phase transition. The trapping potential enables the existence of a pure BEC, while interactions are driving the BKT transition. This delicate behaviour makes it quite subtle to understand the underlying mechanism of the phase transition in a trapped interacting 2D Bose gas. Therefore, the next section aims to understand when we can apply the BKT theory to a 2D Bose gas and how the BKT phase competes with a pure BEC.

Let's consider a non-interacting Bose gas first. The reason that there is no BEC in a non-interacting uniform 2D system can be seen in the relation between phase space density $n\lambda_T^2$ and chemical potential μ ,

$$n\lambda_T^2 = -\ln(1 - e^{\mu/k_B T}) , \quad (3.11)$$

which has a solution for μ for every value of $n\lambda_T^2$ [20]. This is in sharp contrast to the 3D case where condensation is characterised by the absence of a solution for μ above a critical phase space density of $n\lambda^3 \approx 2.612$. However, when a trapping potential is turned on, the density of states changes and we can achieve a pure BEC in the trap center. The analysis by Bagnato et al. [79] revealed that condensation in a non-interacting trapped Bose gas occurs below a critical temperature $T_c < T_{BKT}$:

$$T_c = \frac{\hbar\omega}{k_B\pi} \sqrt{6N} , \quad (3.12)$$

determined by the radial trapping frequency ω and the number of bosons N .

We now turn our attention to an *interacting uniform* gas, where the MWH theorem and the above reasoning might suggest that no phase transition to a superfluid is possible. Here, the BKT theory developed for the 2D XY model from section 3.1.2 helps to understand why the system can develop superfluidity at all.

At first sight, the application of the ideas developed for the spin model to a 2D BEC seems straight forward: One simply replaces the local spin orientation with the complex phase of the wave function. However, the XY model does not take into account that a 2D BEC can show significant density fluctuations as well. We did not encounter this problem in 3D because here for temperatures $T < T_c$ the mean field (MF) approximation is justified where the quantum field $\hat{\Psi}$ is simply replaced by its expectation value $\Psi(\mathbf{r}) = \sqrt{n(\mathbf{r})}e^{i\varphi}$. While $n(\mathbf{r})$ can still vary spatially, the MF approximation does not allow for any quantum fluctuations

$$\Delta n^2 = \langle \hat{n}^2 \rangle - \langle \hat{n} \rangle^2 \quad (3.13)$$

of the density. It turns out that this simplification is too restrictive in 2D systems where we need to capture fluctuations of phase *and* density. Fortunately, at low temperatures T compared to the MF interaction energy $E_{MF} = gn$ density fluctuations are suppressed [64]

$$\frac{(\Delta n)^2}{n^2} = \frac{2}{n\lambda_T^2} \ln \left(\frac{k_B T}{2gn} \right) \ll 1. \quad (3.14)$$

Therefore, for sufficiently low temperatures or strong interactions we can apply the BKT theory to a 2D Bose gas. The regime where Δn is suppressed below thermal fluctuations of a Poisson distribution, i.e. $\Delta n^2 < n$, is called a *quasi-condensate*. Consequently, the quasi-condensate density n_{qc} is usually defined as [80]

$$n_{qc} = \left(2 \langle n \rangle^2 - \langle n^2(\mathbf{r}) \rangle \right)^{1/2}. \quad (3.15)$$

It is important to note that a *quasi-condensate* is not a superfluid, but only associated with the suppression of density fluctuations. The reason for this is that the suppression of density fluctuations sets in earlier than the suppression of phase fluctuations [81]. We can think of a quasi-condensate as a necessary but not sufficient condition for the occurrence of a BKT transition. So what is the sufficient condition, i.e. the critical phase space density of the BKT transition? We know that the superfluid density exhibits a universal jump at $n_s \lambda_T^2 = 4$. But this is not very helpful in practice since only the total density is directly accessible from absorption images. It turns out that an estimate of the critical phase space density $(n\lambda_T^2)_c$ is a theoretically challenging task. There were intensive theoretical investigations based on Quantum Monte Carlo methods by Prokofev et al. [80] which revealed that for a weakly interacting Bose gas, where the dimensionless coupling constant $\tilde{g} < 1$:

$$(n\lambda_T^2)_c = \ln \left(\frac{380 \pm 3}{\tilde{g}} \right). \quad (3.16)$$

We see from eq. 3.16 that strong interactions reduce the critical density $(n\lambda_T^2)_c$ and thereby favor the occurrence of a quasi-condensate with algebraically decaying phase correlations. However, it remains unclear to what extent we can apply their result to the strongly interacting regime where $\tilde{g} \gg 1$.

Finally, we turn to the nature of the phase transition to a superfluid in an *interacting trapped* Bose gas, which is still debated [20]. In principle, we can apply the above reasoning for a uniform system using the local density approximation. Then, for some temperature $T < T_{BKT}$, one would expect the BKT transition to occur in the outer, low density region of the cloud where $(n\lambda_T^2)_c$ reaches its critical value as in eq. 3.16. However, Petrov et al. [81] showed that both a pure BEC and a BKT driven transition are possible in a trapped interacting Bose gas. For temperatures far below the critical point, $T \ll T_{BKT}$, phase fluctuations are significantly suppressed,

$$(\Delta\phi)^2 = \frac{T}{T_{BKT}} \left(\frac{ng}{4\pi\hbar^2} \right)^2 \ln N, \quad (3.17)$$

and a pure condensate emerges which stretches over the whole system [81]. For slightly higher temperatures, still below T_{BKT} , both a BEC and a BKT phase can coexist as pointed out by Simula et al. [82]. In this regime we expect a pure condensate in the central region of the cloud while outer regions should form a quasi-condensate. For even higher temperatures, but still for $T < T_{BKT}$, only the quasi-condensate remains and we should have algebraically decaying phase correlations stretching over the center of the cloud [83]. Therefore, to study the algebraic decay of phase correlations over a wide range in phase space density, it is actually favorable to achieve temperatures not too far below T_{BKT} .

In summary, a study of phase correlations in a strongly interacting 2D Bose gas is of fundamental interest to gain information about the critical point and the fundamental mechanism of the BKT transition. So far, no predictions for the critical point in the strongly interacting regime are available. A quantitative analysis of $g_1(r)$ could reveal the regime of algebraically and exponentially decaying phase correlations which would be interesting to compare to the superfluid density. In principle, both a quasi-condensate *and* a pure BEC are possible in 2D. However, the results of eq. 3.16 suggests that strong interactions favor a BKT-type transition. As we will see in section 4.1.2, currently achievable temperatures with our setup are not too far below T_{BKT} , which might suppress the occurrence of a pure BEC in the center of the trap.

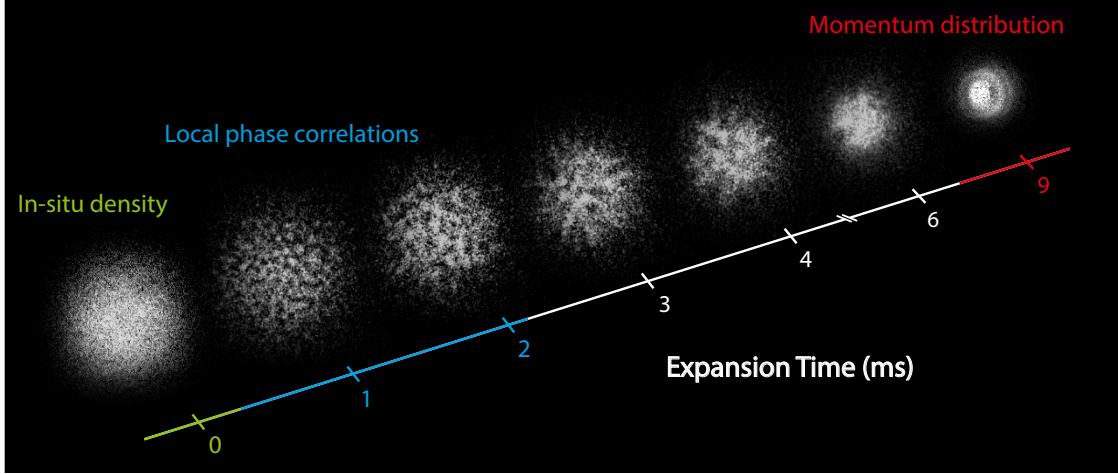


Figure 3.3: Free expansion as a probe of phase correlations on different length scales. A two-dimensional gas of strongly interacting ${}^6\text{Li}$ dimers is released from its tight axial confinement and expands freely in a weakly confining magnetic trap. After short expansion times we analyse the density ripple pattern as a probe of local phase correlations. After long expansion times the cloud is mapped to its bimodal momentum distribution from which we obtain the temperature and quasi-condensed fraction of the gas.

3.2 Revealing in-situ phase fluctuations after short time of flight

The BKT transition is not connected with the occurrence of long-range order, but a qualitative change in the form of spatial correlations between phase fluctuations. Consequently, the characteristics of the transition are not detectable in in-situ density distributions, but are hidden in its quantum noise of phase fluctuations. In principle, one can extract phase information by interfering the cloud with a reference system with a defined phase [84]. In the first observation of the BKT transition in a 2D Bose gas, Hadzibabic et al. [13] prepared several independent layers, which were brought to interference as suggested by [73]. By studying the contrast of the resulting interference pattern they found evidence for quasi-long-range order and the unbinding of V-AV pairs at the transition point. However, due to long expansion times and imaging in radial cloud direction their experiment lacks a direct connection to the local density. Especially the effect of an inhomogeneous density distribution on the interference pattern is still debated. The following section describes how we use a different scheme that allows us to extract local information about phase fluctuations in a 2D Bose gas.

As diverse experiments with ultracold quantum gases may be, the results of most experiments are simply images of atoms. The challenge to probe quantum many body systems is to capture and extract in these images the information about the quantum state we are interested in. A common approach to capture information about phase is to expand the atomic cloud for a certain time. In one of the first observations of a BEC, macroscopic phase coherence could be observed in a

sharp density peak after time of flight [33]. In many systems with more complex phase correlations the mean density profile after time of flight does not reveal details about the quantum state. For example, BCS superfluidity of weakly paired fermions does not appear as a sharp density peak in momentum space. Neither, can we fully characterise Mott-insulating states in optical lattices just from its incoherent momentum distribution. Instead, the analysis of spatial density correlations after time of flight provides a powerful tool to probe strongly correlated quantum systems [8]. Greiner et al. [67] could reveal pair correlations in momentum space of dissociated molecules. So far, momentum space pairing of fermions which results in BCS superfluidity could not be observed. Spatial density correlations of bosons released from an optical lattice revealed details of Mott-insulating states [68]. More recent experiments by Hofferberth et al. [85] and Manz et al. [86] gave an insight into quasi-long range order in one-dimensional Bose gases. The contrast of interference of two interfering 2D Bose gases revealed the BKT transition and quasi-long-range order [13]. First local analyses of density correlations in 2D Bose gases were recently performed by Choi et al. [14] and in Ref. [74]. So far there are no experiments that provide local information about the decay phase correlations.

Here, we probe local phase fluctuations in a 2D Bose gas by performing a short expansion of the cloud. During expansion phase fluctuations transform into density fluctuations, which are imaged along the transverse cloud direction with high optical resolution. As shown in Fig. 3.3, a density ripple pattern develops after the cloud is released from its trap potential. In this section we will concentrate on short expansion times of 0 ms, 0.5 ms, 1 ms and 2 ms, where the overall density profile does not deviate significantly from its in-situ distribution⁴. In section 4.1.2 we will extract the momentum distribution from images taken after long expansion times $t \approx 9$ ms. As shown in Fig. 3.4 the length scale of the density pattern increases with increasing expansion time. It turns out that the fluctuations of density after a certain expansion time contain information about initial phase fluctuations on a certain length scale. We study spatial correlations of the density fluctuation pattern to extract the local decay of phase correlations.

The fundamental quantity to characterise spatial density correlations is the normalised density-density correlation

$$g_2(\mathbf{r}, \mathbf{r}') = \frac{\langle n(\mathbf{r})n(\mathbf{r}') \rangle}{n^2}. \quad (3.18)$$

First, we will restrict our analysis of correlations to the central region of the cloud where the density is almost homogenous $n \approx 2.1 \mu\text{m}^{-2}$. The 2D correlation function is calculated as the scalar product of an image with the same image shifted by a vector $\mathbf{r} - \mathbf{r}'$. Therefore, images of g_2 show a distinct minimum at a certain distance r , which corresponds to the distance between a local maximum and the following

⁴During expansion a weakly confining magnetic trap with frequency $\omega_r \approx 30$ Hz results in an overall decrease in the cloud size. We will use the magnetic confinement as a tool to obtain the momentum distribution as described in section 4.1.2.

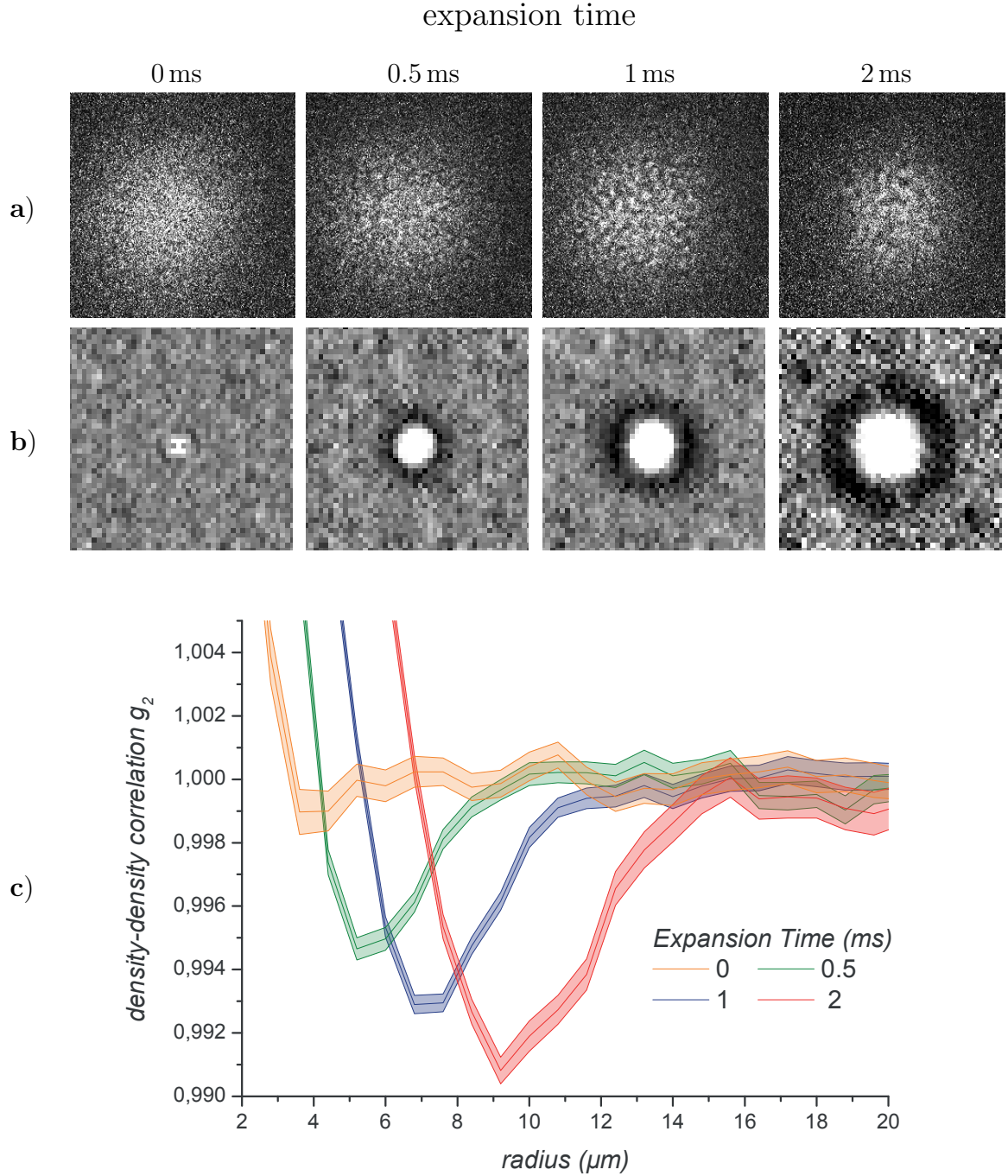


Figure 3.4: Extracting density-density correlations after variable expansion time. A strongly interacting 2D BEC of ${}^6\text{Li}$ dimers with particle number $N \approx 33000$ and temperature $T \approx 24$ nK is prepared in a single layer of a strongly confining blue-detuned lattice with trapping frequency $\omega = 2\pi \cdot 25$ kHz and suddenly released. Top panel (a): individual absorption images along the axial cloud direction for different expansion times. Middle panel (b): 2D density-density correlation $g_2(\mathbf{r})$ in the homogenous central part where $n \approx 2.1 \mu\text{m}^{-2}$. The results shown are averaged over 60 to 110 realisations. Lower panel (c): Radially averaged correlation function $g_2(r)$. The distinct minimum in $g_2(r)$ occurs at larger radii r for longer expansion times.

minimum of density ripples as seen in Fig. 3.4. The increasing length scale of the density pattern for increasing expansion time results in a shift of the minima in g_2 to larger distances. While the observed ripple pattern changes significantly between individual shots, the underlying correlation does not. To improve the signal quality, the density correlation images shown are averaged over 60-110 realisations. Further, we perform a radial average and obtain the radial density-density correlation $g_2(r)$.

3.2.1 Understanding the connection between phase fluctuations and density fluctuations

Since we are not probing the phase correlation function g_1 itself, it is important to understand the connection between phase fluctuations and the resulting density fluctuations after short expansion. The development of the density ripple pattern shown in Fig. 3.4 can be understood in analogy to the Talbot effect [87] as pointed out by Imambekov et al. [88]. When a monochromatic light of wavelength λ passes through a binary amplitude grating with period a , its near field diffraction pattern develops a fractal structure known as *Talbot carpet* [89]. The diffraction pattern repeats itself after the Talbot distance $z_T = 2a^2/\lambda$, where the period of the grating is directly visible in the intensity distribution. When using a sinusoidal phase grating instead of an amplitude grating, a similar diffraction pattern develops in the near field as shown in Fig. 3.5. In the latter case, the grating pattern is recovered after a distance $z = z_T/4 = a^2/2\lambda$ as pointed out by Lohmann et al. [90]. At $z = z_T/4$ the interference pattern is most pronounced and dominates over structures obtained for other propagation distances. Now let us consider the analogy to a Bose gas with phase fluctuations. Instead of a short propagation distance z in the near field, we analyse the evolution of the wavefunction after a short expansion time t . The wavelength of the light source is replaced by the de Broglie wavelength $\lambda_T = 2\pi\hbar/p$ of the Bose gas. We expect to recover the length scale a of initial phase fluctuations after a time

$$t = \frac{z_T}{4} \frac{m}{p} = \frac{a^2 m}{4\pi\hbar}. \quad (3.19)$$

In other words: to each expansion time t corresponds a certain length scale a which would maximise the interference pattern. One of the most striking features of the superfluid BKT phase is the critical behaviour for all temperatures below T_{BKT} as explained in section 3.1.2. Hence, there is no characteristic length scale of phase correlations. Therefore, for each expansion time t , there will always be a length scale a of phase fluctuations which matches condition 3.19 and will consequently dominate the interference pattern.

In terms of wave functions, the previous reasoning can be understood as following [91]. We assume a wave function with some periodical phase modulation corresponding to the momentum $q = 2\pi/a$:

$$\Psi(\mathbf{r}) = \exp(i\delta\phi \cos(\mathbf{q}\mathbf{r})) \approx 1 + i\delta\phi \cos(\mathbf{q}\mathbf{r}). \quad (3.20)$$

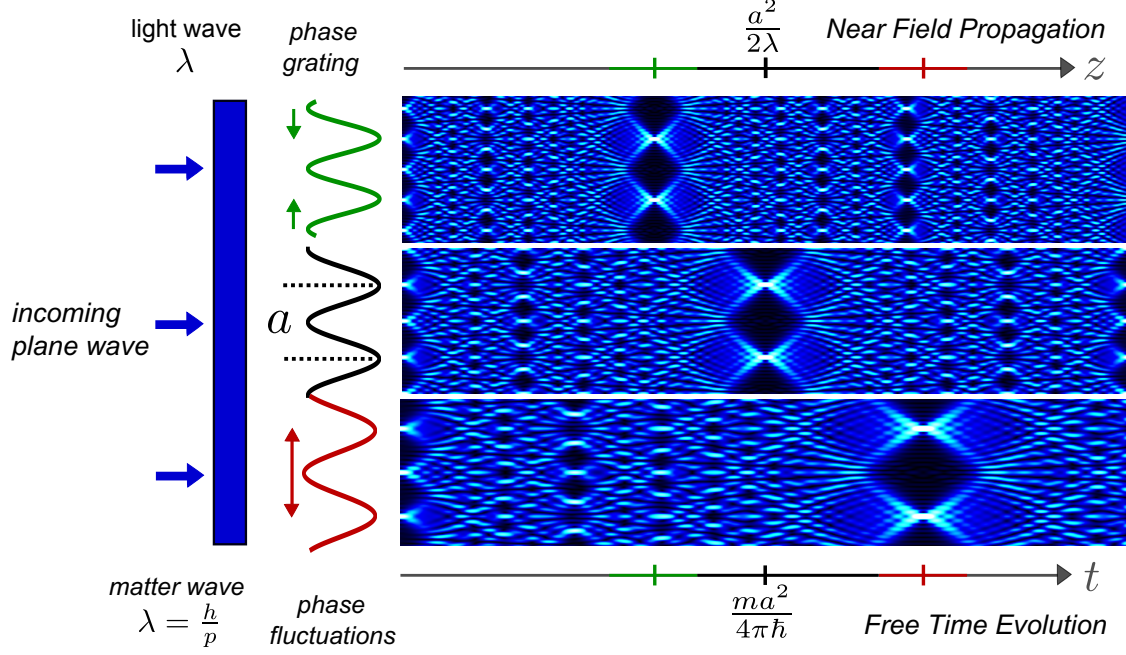


Figure 3.5: Probing phase correlations on different length scales. When monochromatic light of wavelength λ passes through a phase grating with period a , a fractal diffraction pattern develops which reveals the phase grating after a distance $z = a^2/2\lambda$ ⁵. When a BEC with a characteristic length a of phase fluctuations expands freely, the largest density contrast in the interference pattern occurs after a time $t = ma^2/4\pi\hbar$. Since there is no characteristic length scale in the superfluid BKT phase, a certain expansion time t reveals the dominant momentum contribution $q = 2\pi/a = \sqrt{\pi m/\hbar t}$.

Since the expansion in direction of the strongly confined axis is much faster than scattering events between atoms, we can treat the time evolution as non-interacting:

$$\Psi(\mathbf{r}, t) = \Psi(\mathbf{r}) \exp\left(i \frac{\hbar q^2}{2m} t\right). \quad (3.21)$$

Therefore, fluctuations of density $n(\mathbf{r}) = |\Psi(\mathbf{r})|^2$ take the form

$$\delta n(\mathbf{r}) = 2\delta\phi \cos(\mathbf{q}\mathbf{r}) \sin\left(\frac{\hbar q^2}{2m} t\right). \quad (3.22)$$

When the condition 3.19 is fulfilled, i.e. $\hbar q^2 t/m = \pi$, we see from eq. 3.22 that density fluctuations corresponding to a momentum $q^2 = \pi m/\hbar t$ have the largest amplitude and will dominate the density ripple pattern. Our observation that the distinct minimum in $g_2(r)$ is shifted to larger distances for longer expansion times is a first indicator for the algebraic decay of phase correlations in a 2D Bose gas. So far we restricted our analysis to the central region of the cloud. In the following we will give a short preview of our analysis in areas of lower density. A more detailed analysis follows in section 4.2.2, where we use the density dependence of phase correlations to extract information about the critical point of the BKT transition and the algebraic scaling exponent.

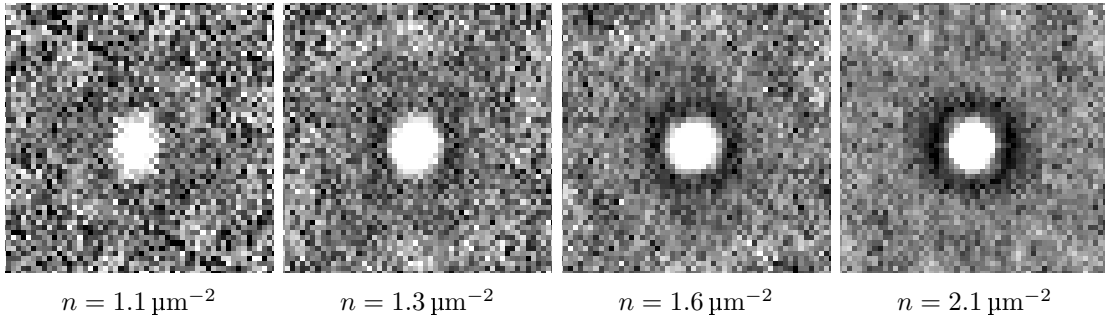
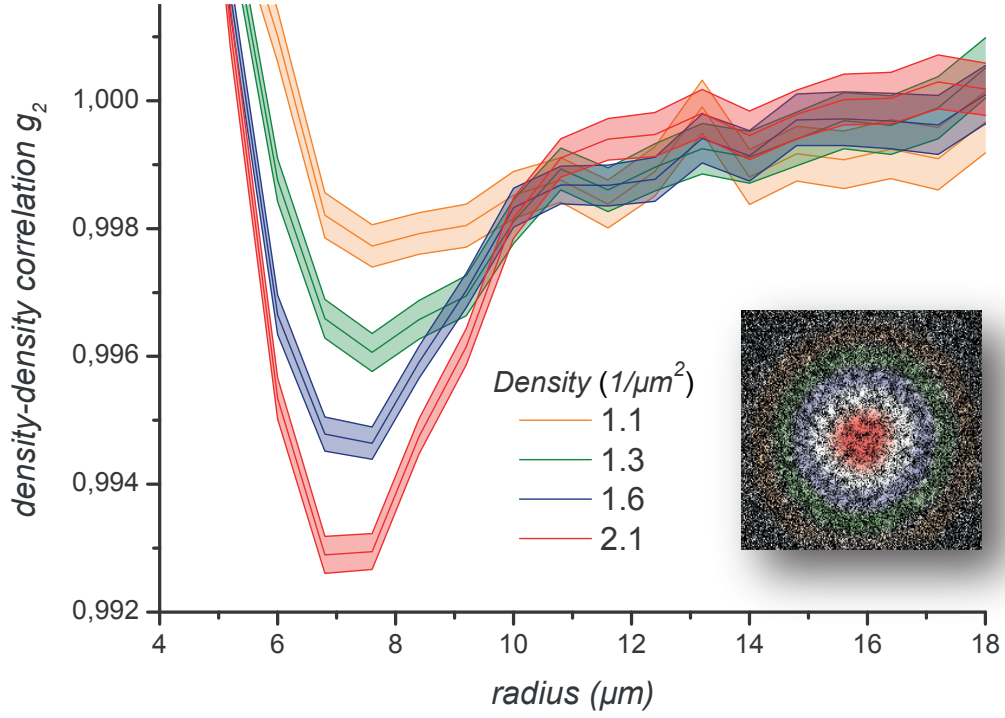


Figure 3.6: Density-density correlations in areas of specific density. A strongly interacting 2D BEC of ${}^6\text{Li}$ dimers expands freely for 1 ms and is destructively imaged as shown in Fig. 3.4. We evaluate the density-density correlation g_2 for each individual realisation on areas of comparable density (colored inset). The results plotted are averaged over 100 realisations. Upper panel: Radially averaged correlation function $g_2(r)$. The indicated shaded area represents the standard deviation of the mean. The reference density is taken from the mean of all realisations. We observe a distinct minimum in g_2 which vanishes for lower densities indicating the phase transition from algebraically to exponentially decaying correlations. Lower panel: Corresponding 2D density-density correlation images for different densities n .

3.2.2 Density dependence of phase correlations

In the local density approximation, we expect the superfluid phase to be present only in the central region of the cloud. In the outer region where the density has dropped below a critical value $(n\lambda_T)_c$ we expect phase correlations to decay quickly. To analyse the density dependence of phase correlations we evaluate $g_2(r)$ in areas of the cloud with a certain density as indicated by the colored regions in Fig. 3.6. We show $g_2(r)$ at fixed expansion time $t = 1$ ms and variable density $n = (1.1 - 2.1)\mu\text{m}^{-2}$. We clearly observe a distinct minimum for high densities $n \approx 2\mu\text{m}^{-2}$ which vanishes for lower densities $n \approx 1\mu\text{m}^{-2}$. This is a signature for the transition from algebraically decaying phase correlations in the superfluid to quickly decaying phase correlations in the thermal part of the cloud. For each expansion time t we probe a certain length scale $\sqrt{\hbar t/m}$ of coherence in our system. For the superfluid part we expect that an interference pattern can develop even for long expansion times t . For the thermal part of the cloud, phase correlations decay quickly on a short length scale ξ , i.e. $g_1(r) \propto \exp(-r/\xi)$. We therefore expect that after a short time of flight t for which $\xi < \sqrt{\hbar t/m}$ no interference pattern and no distinct minimum in g_2 should be visible. In general, we expect the difference between the thermal and superfluid to be most significant for long expansion times as pointed out in [75]. Overall, our data from Fig. 3.6 seems to match our theoretical expectation well. Below a density $n \approx 1.1\mu\text{m}^{-2}$ there is no overall change in the behaviour of g_2 and no minimum detectable.

4 Extracting the algebraic scaling exponent

The work presented in this thesis aims at providing a quantitative study of spatial density correlations. Since the evaluation of correlations is a delicate task, we need to be aware of a number of influencing factors that might distort our results. Before we proceed to our final results for the algebraic scaling exponent in section 4.2.2, we will therefore give a detailed overview of our measurement scheme (4.1.1), the temperature determination (4.1.2) and the data analysis (4.1.3). In section 4.1.4, we will develop a method to test our evaluation scheme. Further, we will give a short overview of contributions to measured correlations that might arise from other sources of noise and our imaging system in section 4.1.5.

4.1 Methods

4.1.1 Measurement procedure

Preparation

The high-resolution detection of density fluctuations in a two-dimensional Fermi gas is an experimentally challenging task. It requires the preparation of a single-layer 2D cloud with significant quasi-condensed fraction and sufficient optical resolution to probe fluctuations on small length scales. We prepare an ultracold Fermi gas of ${}^6\text{Li}$ atoms in a single layer of a blue-detuned optical lattice as described in section 2.1. A prerequisite to probe phase fluctuations through density fluctuations is a quasi-condensate, which can only be realised with bosons. The broad Feshbach resonance of ${}^6\text{Li}$ allows us to tune interactions in a wide range. In 3D, ${}^6\text{Li}$ atoms form bosonic dimers at a positive scattering length a_{3D} . The dimers can in turn condense to a BEC below a critical phase space density $(n\lambda_T)_c$. In 2D, the formation of bound dimers becomes favorable as well. However, due to the algebraic decay of correlations, bosonic dimers only form a quasi-condensate. We achieve temperatures of $T_c = 0.05 T_F$, well below expected critical temperatures of $T \approx 0.1T_F$ [92] ensuring a sufficient condensate fraction of about 49% as shown in Fig. 4.2. In the weakly interacting quasi-2D regime, the interaction strength is density-independent and determined only by the harmonic oscillator

length $l_z = \sqrt{\hbar/m\omega_z}$ and the 3D scattering length a_{3D} :

$$\tilde{g} = \sqrt{8\pi} \frac{a_{3D}}{l_z} \quad (4.1)$$

For a magnetic field of $B = 710$ G and a trapping frequency $\omega_z = 2\pi \cdot 25$ kHz the harmonic oscillator length $l_z \approx 5000a_0$ is on the order of the 3D scattering length $a_{3D} \approx 1800a_0$, where a_0 is the Bohr radius. Therefore, we might need to consider a density dependence of interactions. Using the more general¹ expression derived by Petrov et al. [63] and the experimental parameters described above, we obtain $\tilde{g} \approx 2.7$ for a density of $n = 2.3 \mu\text{m}^{-2}$. This value clearly deviates from $\tilde{g} \approx 1.9$ obtained using the approximate expression 4.1.

Detection

After preparing the cloud, we suddenly turn off the repulsive lattice. Because of the strong confinement in axial direction the resulting expansion in that direction should be so quick that the evolution of the state can simply be described as non-interacting. The relevant scales for this approximation are the mean field energy E_{MF} and the level spacing $\Delta E = \hbar\omega_z$ of the vertical confinement. Using the calculated interaction strength $g \approx 2.7$ and a density $n = 2.3 \mu\text{m}^{-2}$ we obtain

$$\frac{E_{MF}}{\Delta E} = \frac{\frac{\hbar^2}{m} \tilde{g} n}{\hbar\omega_z} = \frac{\hbar \tilde{g} n}{2m\omega_z} \approx 0.07 . \quad (4.2)$$

We can therefore ignore interaction effects during expansion which suggests that phase fluctuations are transformed in density fluctuations by free time evolution. We detect density fluctuations after various expansion times 0 ms, 0.5 ms, 1 ms and 2 ms by absorption imaging with resonant light. Here the increasing size in z-direction might be limiting our resolution because of our limited depth of field as explained in section 4.1.5.

4.1.2 Temperature and condensate fraction

The determination of temperature in a strongly interacting system is a challenging task. In general, the temperature of an ensemble can be obtained from its momentum distribution. While the momentum distribution of non-interacting systems are well known there are no reliable predictions for the strongly interacting regime. In principle, there are two ways to circumvent this issue:

1. Use a non-interacting system in thermal equilibrium with the interacting one
2. Map the strongly interacting distribution to that of a non-interacting system

¹Only recently the strongly interacting regime in 2D has become accessible [49, 61, 62]. The regime corresponds to $l_z \ll a_{3D}$ where the nature of interactions changes from 3D to truly 2D and the expression for \tilde{g} derived by Petrov et al. [63] loses its validity.

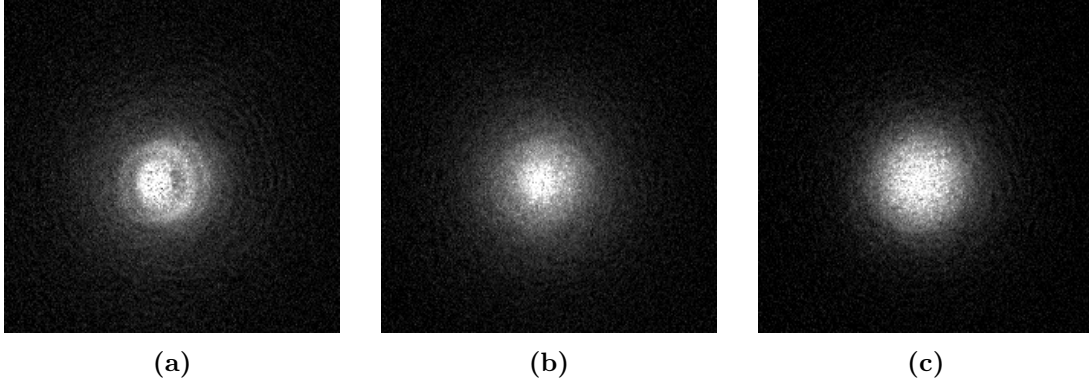


Figure 4.1: Images of the momentum distribution for different interaction strengths. A strongly interacting 2D Bose gas is prepared with different interaction parameters $\ln(k_F a_{2D}) = -1.9$ (a), $\ln(k_F a_{2D}) = -0.8$ (b), $\ln(k_F a_{2D}) = -0.3$ (c) by exposing the gas to a magnetic field $B = 710$ G (a), $B = 770$ G (b), $B = 810$ G (c). Absorption images shown are taken 9 ms after a sudden release from the cloud’s tight axial confinement. The expansion time corresponds to $T/4$ of the radial magnetic confinement with frequency $\omega = 2\pi/T \approx 30$ Hz

While the second option sounds exotic, it turns out that it can be easily realised for a two-dimensional system. When the strongly confining potential is suddenly switched off, the cloud expands so quickly in axial direction that interactions between atoms in the early stage of the expansion can be safely ignored. In the far-field, i.e. in the limit of very long expansion times, the density distribution of the strongly interacting system is mapped to the momentum distribution of an ideal gas. When there is no additional trapping potential present the far-field is only reached after very long expansion times which are not achievable in our setup. However, when the cloud expands in the presence of a weak radial harmonic confinement with trapping frequency $\omega = 2\pi/T$, the position space distribution is already mapped to momentum space after an expansion time $t = T/4$. This method was recently suggested by Murthy et al. [93] and successfully implemented to determine the phase diagram of a strongly interacting 2D Fermi gas [49].

Here, the method enables us to determine the temperature of a strongly interacting 2D Bose gas of ${}^6\text{Li}$ dimers. After suddenly switching of the repulsive lattice, we detect the momentum distribution after an expansion time of $t = T/4 \approx 9$ ms. To access the temperature of the cloud we fit the outer thermal part of the gas with the momentum distribution of an ideal Bose gas:

$$f(p) \propto e^{-p^2/2mk_B T} . \quad (4.3)$$

We restrict the fit to a radial interval $[r_0, r_{max}]$ from the cloud’s center. While $r_{max} = 80 \mu\text{m}$ is determined by our image size, it is not obvious what minimal radius r_0 we should choose. Here, we fit the radial density distribution with the general expression

$$n(r) = A + B \cdot e^{-(r/w)^2} , r_0 < r < r_{max} . \quad (4.4)$$

for various values of r_0 and determine the R^2 -value of the fit. We keep the offset A fixed and vary amplitude B and waist w . As shown in Fig. 4.3, above a certain value of r_0 the R^2 -value reaches its maximum in the form of a plateau which we therefore associate with the optimal value. We repeat this procedure for different values of the offset A . The correct value for A is found when the plateau of the R^2 -values coincides with a plateau in the values of the waist w . For the realisation shown in Fig. 4.2, we obtain $w = (52.0 \pm 0.3) \mu\text{m}$, which for $t = 9 \text{ ms}$ corresponds to a temperature of

$$T = \frac{m_d w^2}{2k_B t^2} \approx (24.0 \pm 0.3) \text{ nK} . \quad (4.5)$$

When using eq. 4.5 it is important to use the mass $m_d = 2m$ of ${}^6\text{Li}$ dimers. Further, t should be obtained from the trap frequency $\omega = 2\pi/T$ instead of the actual expansion time t_{exp} . The momentum distribution shown in Fig. 4.2 allows us to determine the quasi-condensed fraction $N_{qc}/N \approx 0.49$. Here, we treat the non-Gaussian distribution as the quasi-condensate as done by Clade et al. [46]. Similarly to their results, we observe a *trimodal* distribution with a region between $r = 30 \mu\text{m}$ and $r = 40 \mu\text{m}$ which is neither part of the central parabola nor the outer Gaussian shape. As already pointed out by Clade et al. [46] this observation is in contrast to the results obtained by Kruger et al. [94], who observed a clear bimodal distribution. In our case, the trimodal distribution is in parts the result of a ring around the quasi-condensed center of the momentum distribution as can be seen in Fig. 4.1a. We do not fully resolve the ring structure in the radial distribution in Fig. 4.2, because we performed a running average of width $7 \mu\text{m}$ to increase the signal quality for large r . One might think that the ring corresponds to the binding energy of molecules which was already analysed in [61] using RF-spectroscopy. After the strong axial confinement is switched off, we expect ${}^6\text{Li}$ dimers to be dissociated. Since dimers of the quasi-condensate do not carry any net-momentum both dissociated atoms carry a momentum \mathbf{k} with same size but opposite direction which would result in a ring structure at a certain distance

$$r = \frac{\hbar k}{m} t = \sqrt{\frac{E_B}{m}} t \quad (4.6)$$

Using the 2D scattering length $a_{2D} \approx 2.09 \cdot l_z \exp(-\sqrt{\pi/2} l_z / a_{3D})$ [95] with 3D scattering length $a_{3D} \approx \cdot 1900 a_0$ and harmonic oscillator length $l_z = 4900 \cdot a_0$, where a_0 is the Bohr radius, to calculate the binding energy $E_B = \hbar^2 / m a_{2D}^2$, we obtain $r \approx 2.5 \text{ mm}$. The ring structure in Fig. 4.1a occurs at a distance of about $25 \mu\text{m}$ and cannot be explained by the above reasoning.

4.1.3 Local evaluation of correlations

We are interested in evaluating and comparing spatial density correlations in areas of the cloud within a specific density interval $[n_{min}, n_{max}]$. This can be a challenging task since for inhomogenous density distributions the form and size of the areas

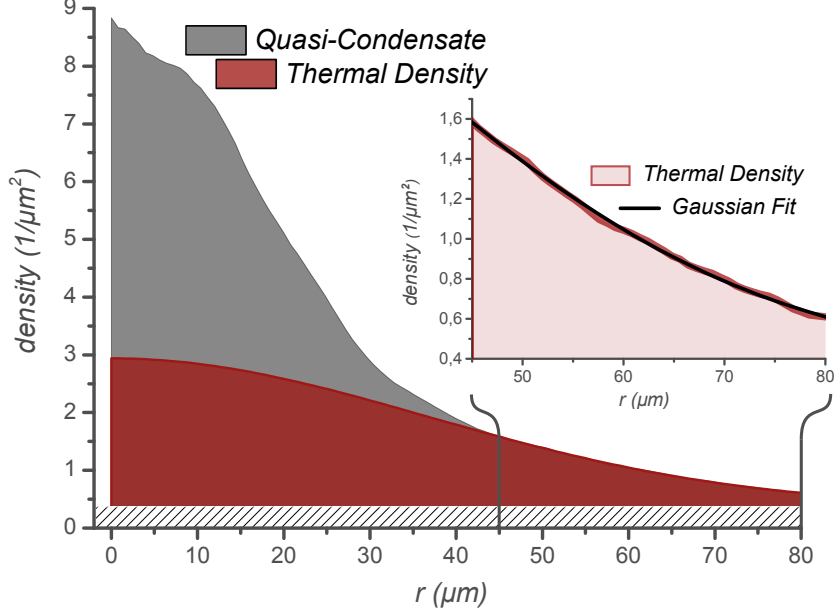


Figure 4.2: Radial momentum distribution of a strongly interacting 2D Bose gas. After sudden release from its tight axial confinement the cloud expands freely in a weakly confining magnetic trap with frequency $\omega \approx 2\pi \cdot 30 \text{ Hz} = 2\pi/T$. After an expansion time $t = T/4$ the position space distribution is mapped to momentum space. We determine quasi-condensate fraction $N_{qc}/N \approx 0.49$ and temperature $T = (24.0 \pm 0.3) \text{ nK}$. Inset: A Gaussian is fitted to the outer part $r > r_0$ of the distribution as described in Fig. 4.3. We radially average the distribution with a moving average of width $7 \mu\text{m}$ to increase the signal quality for large r . Therefore, the ring features of Fig. 4.1a are not fully resolved here and appear as an apparent trimodal distribution.

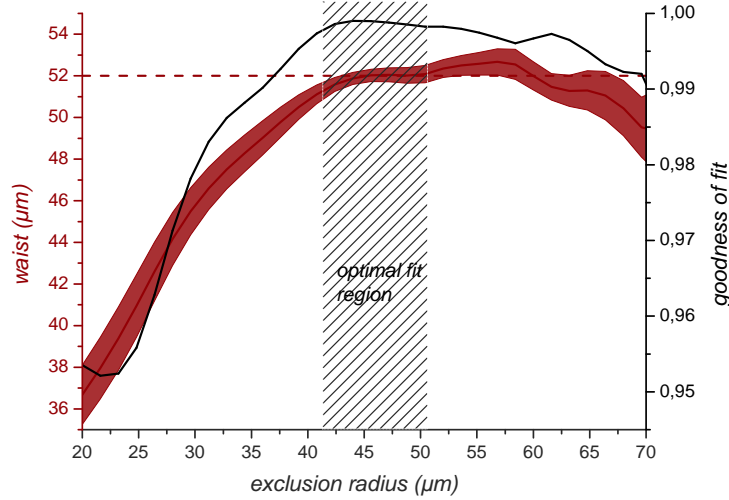


Figure 4.3: Waist determination of a thermal Bose gas. A Gaussian function $A + B \exp(-r^2/w^2)$ is fitted to our momentum distribution in Fig. 4.2 in an interval $[r_0, 80 \mu\text{m}]$ with varying exclusion radius r_0 and fixed offset $A = 3.7 \mu\text{m}$. The correct waist $w = (52.0 \pm 0.3) \mu\text{m}$ is independent of the exclusion radius in a large interval $r_0 = 42 \mu\text{m} - 50 \mu\text{m}$ and coincides with a maximum in the goodness of fit (R^2 -value) when the correct offset is chosen.

where the correlations are evaluated on differ significantly from each other. The following section will give a step-by-step procedure to obtain comparable correlation functions independent of the evaluation area. To check that the calculated correlation functions only capture physical information we will validate the procedure using test distributions with an imprinted pixel-pixel correlation.

Extracting density-density correlations on areas of constant density

The following steps are performed to calculate the normalised density-density correlation function

$$g_2 = \frac{\langle n(r)n(0) \rangle}{n^2} \quad (4.7)$$

1. Average over sufficiently large number N of density images $n_i(\mathbf{r})$ to get a smooth mean density distribution

$$n_{mean}(\mathbf{r}) = \frac{1}{N} \sum_i^N n_i(\mathbf{r}) \quad (4.8)$$

The mean density will serve as a reference for the following steps and should not contain any fluctuations on scales smaller than the actual cloud form. We therefore fit $n_{mean}(\mathbf{r})$ using a smoothing spline.

2. Divide each individual realisation by the mean distribution. This way the normalisation of eq. 4.7 is automatically fulfilled when calculating g_2 in step 5.

$$n_{norm,i}(\mathbf{r}) = n_i(\mathbf{r})/n_{mean}(\mathbf{r}) \quad (4.9)$$

3. Crop the normalised density to an area A within the desired density interval $[n_{min}, n_{max}]$:

$$A(\mathbf{r}) = \begin{cases} 1 & \text{for } n_{min} < n_{mean}(\mathbf{r}) < n_{max} \\ 0 & \text{else} \end{cases}$$

$$n_{crop,i}(\mathbf{r}) = n_{norm,i}(\mathbf{r}) \cdot A(\mathbf{r}) \quad (4.10)$$

4. Reduce the effect of fluctuations of the total atom number by dividing each $n_{crop,i}$ by its mean density:

$$n_{final,i}(\mathbf{r}) = \frac{n_{crop,i}(\mathbf{r})}{\sum_{\mathbf{r}'} n_{crop,i}(\mathbf{r}')} \quad (4.11)$$

5. Calculate the autocorrelation $\tilde{g}_{2,i}$ for each individual realisation and average over all realisations

$$\tilde{g}_{2,i}(\mathbf{r}) = \sum_{\mathbf{r}'} n_{final,i}(\mathbf{r}') n_{final,i}(\mathbf{r}' - \mathbf{r}) \quad (4.12)$$

$$\tilde{g}_2(\mathbf{r}) = \frac{1}{N} \sum_i^N \tilde{g}_{2,i}(\mathbf{r}) \quad (4.13)$$

6. Calculate the autocorrelation g_A of the binary area A to normalise $\tilde{g}_{2,i}$. This will allow us to compare correlations which are evaluated on different regions of the cloud.

$$g_{2,A}(\mathbf{r}) = \sum_{\mathbf{r}'} A(\mathbf{r}') A(\mathbf{r}' - \mathbf{r}) \quad (4.14)$$

$$g_2(\mathbf{r}) = \tilde{g}_2(\mathbf{r}) / g_{2,A}(\mathbf{r}) \quad (4.15)$$

The above calculation of correlations on a restricted area A assumes that the form of g_2 doesn't change within A . This assumption is valid when A corresponds to an area inside the cloud within a narrow density interval, i.e. an almost constant phase space density.

Evaluation of the power spectrum

It is often convenient to analyse correlations in momentum-space, where the relevant length scales are directly visible. The main quantity for our subsequent analysis is the *power spectrum*, which is obtained from g_2 via Fourier transformation:

$$p(\mathbf{q}) = \int d^2\mathbf{r} \cos(\mathbf{q}\mathbf{r}) (g_2(\mathbf{r}, t) - 1) . \quad (4.16)$$

Our absorption images contain information in discrete pixel values of size $\Delta x = 0.8 \mu\text{m}$ on a quadratic $n \times n$ grid. We therefore evaluate eq. 4.16 via a discrete *fast Fourier transformation*. The position space pixel size Δx then corresponds to a pixel size $\Delta q = n\Delta x/2\pi$ in Fourier space. Further, each pixel value of the discrete power spectrum has units of $(\Delta x)^2 = 0.64 \mu\text{m}^2$.

4.1.4 Testing the evaluation scheme

Any reliable evaluation of correlations needs testing. This holds especially true for our analysis where the size and shape of the area on which correlations are evaluated change significantly. To test the validity and robustness of our analysis method we need a set of reference distributions with given correlations. In principle, one could take another physical system like a thermal cloud as a reference. Images of thermal ensembles would be suited to analyse contributions of shot noise

and technical noise which should appear on very small length scales. However, we are interested in probing correlations on significantly larger length scales, where no trivial physical reference system exists.

We therefore numerically create a set of test distributions with an explicitly imprinted pixel-pixel correlation. This allows us to understand how we can uncover density-density correlations on a finite region from a finite set of images.

First, we create a set of N test images $\{\mathcal{T}_i\}_{i=1\dots N}$ by convolving pseudo-random matrices \mathcal{M}_i with a certain imprinting function f

$$\mathcal{T}_i = \mathcal{M}_i \star f \quad (4.17)$$

In analogy to density fluctuations we consider fluctuations with a certain amplitude A around 1 of the form

$$\mathcal{M}_i = 1 + A \cdot \left(\mathcal{R}_i - \frac{1}{2} \right) , \quad (4.18)$$

with a pseudorandom standard uniform distribution \mathcal{R}_i on the open interval $(0, 1)$ which is generated with *Matlab*'s implemented function *rand*. Since $\text{Var}(\mathcal{R}) = 1/12$ we get pixel fluctuations in \mathcal{M}_i with variance

$$\text{Var}(\mathcal{M}_i) = \frac{A^2}{12} \quad (4.19)$$

The pixel-pixel correlation g_2 is then approximately reproduced by averaging over a sufficiently large number of images

$$g_2 \approx \sum_i^N \mathcal{T}_i \star \mathcal{T}_i = \sum_i^N (\mathcal{M}_i \star f) \star (\mathcal{M}_i \star f) = \sum_i^N (\mathcal{M}_i \star \mathcal{M}_i) \star (f \star f) \quad (4.20)$$

$$= \frac{A^2}{12} f \star f \quad (4.21)$$

We can therefore test our evaluation scheme of section 4.1.3 by comparing g_2 obtained from the set of test images to the theoretical expectation 4.21. Here, we take $f(\mathbf{r}) = \text{sinc}(\mathbf{r}/w)$ with a characteristic length scale $w = 5$ px as imprinting function. Correlations then also take the form of a sinc-function which resembles the theoretical expectation derived in Ref. [88] and Ref. [75]. Figure 4.4 shows a comparison between imprinted correlations from eq. 4.21 and our evaluation results according to the procedure described in section 4.1.3 with an image number of $N = 10, 50, 100$. Here, we use an evaluation area which corresponds to a density interval $n = 2\mu\text{m}^{-2} \pm \Delta n$ in the image shown in Fig. 3.4 with $\Delta n = (0.1 - 0.2)\mu\text{m}^{-2}$. We see that for a given density interval Δn the signal-to-noise ratio greatly increases with the number N of images taken. Analogously, at a fixed number N the signal improves for larger density intervals.

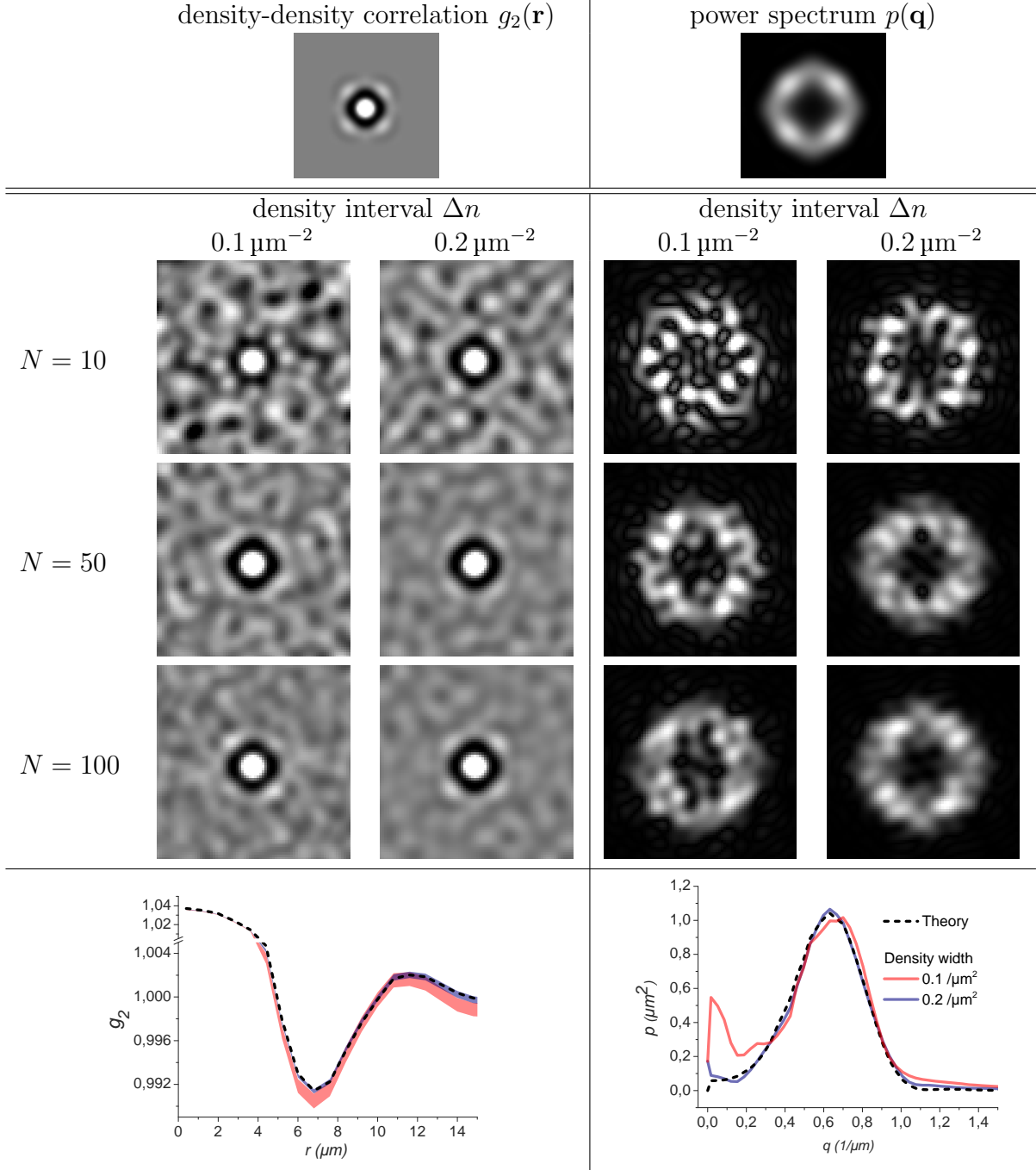


Figure 4.4: Testing the evaluation of density-density correlations using test distributions. We imprint a specific pixel-pixel correlation to test images (top row). Using our evaluation scheme of section 4.1.3 we recover the imprinted density-density correlation g_2 (left column) and its power spectrum p (right column) from N test images generated as described in section 4.1.4. Here, we use an evaluation area which corresponds to a density interval $n = 2\mu\text{m}^{-2} \pm \Delta n$ in the image shown in Fig. 3.4 with $\Delta n = (0.1 - 0.2)\mu\text{m}^{-2}$. Bottom row: radial average of correlations evaluated with $N = 100$. Correlations for $\Delta n = 0.2\mu\text{m}^{-2}$ (blue line) match the theoretical expectation (dashed line), while $\Delta n = 0.1\mu\text{m}^{-2}$ (red) results in significant noise contributions especially in the low-momentum part of the power spectrum.

Similarly, we test our evaluation of the power spectrum $p(\mathbf{q})$ by applying 4.16 to the previously generated test images. Since we evaluate g_2 on restricted areas, values for large r do not contain physical information. We therefore restrict the evaluation of the power spectrum to small distances $r < r_{max}$ and ignore contributions for larger r where $g_2(\mathbf{r}) \approx 1$. This is done by setting:

$$g(\mathbf{r}) = \begin{cases} g(\mathbf{r}) & \text{for } |\mathbf{r}| < r_{max} \\ 1 & \text{else} \end{cases} \quad (4.22)$$

The value of r_{max} has to be chosen very carefully, such that all resolvable features of g_2 are still considered. For the following test we set $r_{max} = 25$ px. The right column of Fig. 4.4 shows that our evaluation scheme allows to recover the imprinted power spectrum. It is clearly visible that for a narrow density interval $\Delta n = 0.1 \mu\text{m}^{-2}$ even for large N the low-momentum part of the power spectrum deviates significantly from the imprinted spectrum. For a larger density interval $\Delta n = 0.1 \mu\text{m}^{-2}$ we are able to recover the low-momentum part quite well.

The present section gave an overview of our data analysis of correlations. We described a step by step procedure to calculate density-density correlations on restricted areas. We introduced the power spectrum $p(\mathbf{q})$, which will be the central quantity for the following determination of the algebraic scaling exponent. Finally, our evaluation scheme was successfully tested by evaluating correlations on areas which correspond to a certain density interval in actual absorption images. The tests indicated that in general a large density interval is favorable to improve the signal to noise ratio. Since we took about $N = 50 - 100$ absorption images for each expansion time we find a good compromise of density resolution and signal quality in an interval of $\Delta n = n_{max} - n_{min} = 0.2 \mu\text{m}^{-2}$ for the following analysis.

4.1.5 Other influences to measured correlations

We saw in the previous section that for a sufficiently large density interval and number of realisations we can in principle almost perfectly recover $g_2(\mathbf{r})$ and $p(\mathbf{q})$. Before we can extract quantitative information about the decay of phase correlations from these quantities, we need to consider other influences apart from phase fluctuations that might affect the density correlations we obtain from our analysis. Here, we will concentrate on the effect of shot noise and the imaging system. While atomic shot noise is an intrinsic physical contribution to correlations, the imaging system only affects the imaged distribution.

Shot noise

It is an intrinsic quantum-mechanical property that there is no definite particle number N for $T > 0$. Instead, between individual measurements one always has fluctuations $\Delta N^2 \approx N$ in atom number. When performing absorption imaging

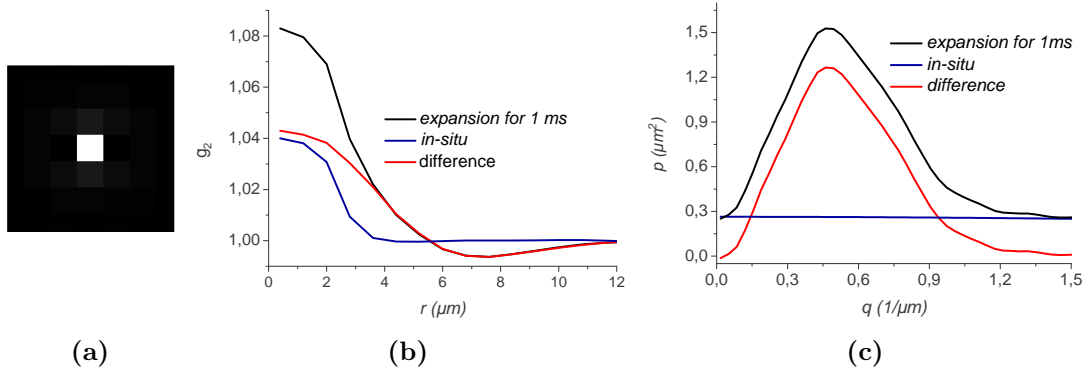


Figure 4.5: Subtraction of the shot noise contribution. We use the density correlation of the in-situ distribution (a) to subtract the shot noise contribution from the correlation function g_2 (b) and the power spectrum p (c) after an expansion time of 1 ms. For illustration, we evaluate correlations in a density interval $n = (2.0 \pm 0.1) \mu\text{m}^{-2}$. Image (a) shows only the central part of the density-density correlation and is scaled to its maximum value. For the subtraction it is sufficient to restrict the shot noise contribution to its central peak, which is a factor 10 larger than its neighbouring pixels.

of an atomic cloud we have mainly two shot noise contributions: *atom shot noise* and *photon shot noise*. Both contribute to the total fluctuation of imaged particle number on a single pixel. Naively, one might not expect any spatial correlation between individual pixels due to shot noise. Consequently, there should not be any contribution to our evaluation of $g_2(r)$ apart from $r = 0$. However, this statement only holds when individual pixel values are completely independent from each other. The limited optical resolution of any imaging systems results in a smearing out of individual pixels. In other words: each pixel contains a bit of information of neighbouring pixels and is therefore correlated with them. Formally, we can interpret our images as a convolution of the actual atomic distribution and a characteristic imaging function, called *point-spread-function*². The width of the point-spread function determines the actual spot size that can be optically resolved. It is a great benefit of our high-resolution imaging system providing a resolution on the order of $1 \mu\text{m}^3$. This enables us to separate between shot noise contributions and density correlations due to phase fluctuations even for relatively short expansion times. Still, the question remains how we can reliably determine the shot noise contribution $g_{2,shot}$ which we eventually subtract from g_2 .

Here, we simply take the in-situ distribution as a reference and use our evaluation scheme of section 4.1.3 to get $g_{2,shot}$ for a specific density interval as shown in Fig. 4.5. We see that the dominant contribution to $g_{2,shot}$ occurs in the center of the image corresponding to $r = 0$. Since the center pixel value is significantly larger than neighbouring pixel values it is sufficient to restrict g_2 to its center value only when performing the subtraction. This observation might support the expectation

²A detailed analysis how to extract the point spread function from in-situ absorption images is given in Ref. [96].

³Our imaging system is described in detail in Ref. [18] and Ref. [97].

that the resolution of our imaging system should be on the order of the pixel size $\Delta x = 0.8 \mu\text{m}$. However, the $r = 0$ value will be affected by uncorrelated technical noise as well. Therefore, a more careful analysis is needed when we want to extract the resolution of our imaging system. Nevertheless, we see in Fig. 4.5b and Fig. 4.5c that the in-situ distribution provides a reliable reference to subtract the shot noise component in densit-density correlations. For an expansion time of $t = 1 \text{ ms}$ the overall offset of the power spectrum seen in Fig. 4.5c is successfully subtracted.

Limited depth of field

The above analysis concentrated on correlations that are inherent to the physical system itself. However, absorption images do not necessarily reflect only the intrinsic properties of the atomic gas but are always influenced by the imaging system itself. In the previous section we encountered the influence of limited optical resolution which resulted in a smearing out of the shot noise contribution. Now, we will focus on the effect of a limited depth of field in axial direction. While the shot noise contribution only affected the high-momentum part of $p(\mathbf{q})$ we will see that the finite extent in axial direction affects correlations on all length scales. The following section is therefore of fundamental importance to extract quantitative information about correlations from absorption images.

While we can image structures inside the focal plane with diffraction limited resolution, outside the focal plane resolution decreases. The characteristic distance over which resolution degrades is called *depth of field*. When the cloud is released from its tightly confining potential it quickly expands in axial direction as shown in Fig. 4.6. Thereby the cloud's width in axial direction quickly exceeds the depth of field of our imaging system. Therefore, absorption images even after short expansion time naturally cover an integration over multiple planes, where structures far from the focal plane are not resolvable. Thus, we expect a diffuse background to decrease the contrast of density fluctuation patterns. In general we expect the ratio of depth of field d and axial cloud width w to determine the reduction in contrast. When we assume that only structures inside the depth of field are resolvable, imaged correlations for $d < w$ should be averaged out and thereby reduced by a factor $D < 1$.

$$g_{2,avg}(\mathbf{r}) = 1 + D (g_2(\mathbf{r}) - 1) \quad (4.23)$$

$$p_{avg}(\mathbf{q}) = D \cdot p(\mathbf{q}) \quad (4.24)$$

In general, the exact value of the prefactor in eq. 4.24 depends on details of the imaging like spatially varying magnetic field strengths and is therefore hard to determine. Introducing the prefactor as third free parameter in eq. 4.26 besides the scaling exponent and the cutoff length would cause a redundancy in determining the scaling exponent. We therefore adopt the method recently suggested in [93] to reduce the expansion in axial direction. Quickly, after the strongly confining lattice is switched off we turn on an attractive dipole trap for a short time. Figure

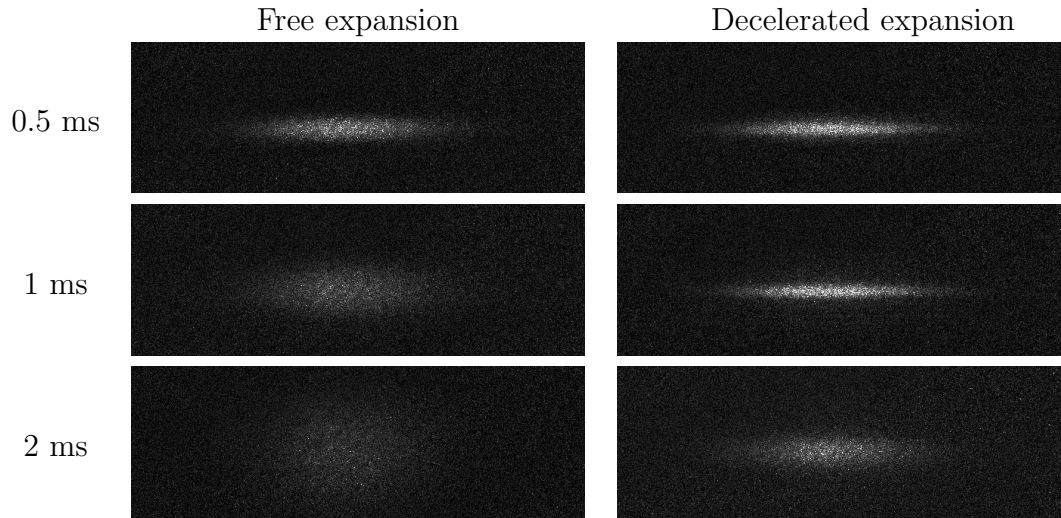


Figure 4.6: Deceleration of the rapid expansion in axial direction. Left panel: A 2D Bose gas is released from its tight harmonic potential and expands quickly in axial direction. Right panel: Same as left panel where an additional red-detuned dipole trap is flashed on to stop the motion in axial direction. A comparison of the width in axial direction is found in Fig. 4.7

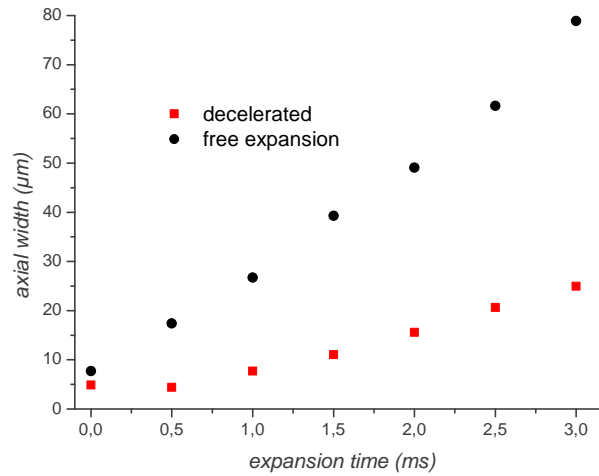


Figure 4.7: Reducing the cloud width in axial direction after free expansion. A red-detuned dipole trap is flashed on to stop the rapid expansion of the cloud in axial direction. The axial width of the cloud remains small for expansion times up to 2 ms. This will enable us to study density correlations without taking into account the limited depth of field of our imaging setup.

4.6 and 4.7 show that this method can successfully reduce the expansion in axial direction. We therefore expect that even for expansion times up to 2 ms we can fully resolve density fluctuations. At the time of writing, the effect of the axial cloud width on the measured correlation spectrum was not analysed. When it comes to quantitative results, we will therefore restrict ourselves to a short expansion time $t = 0.5$ ms where the cloud width is still on the order of the depth of field.

4.2 Results

We saw in section 3.2 that we can successfully extract information about phase correlations in a 2D Bose by studying density-density correlations after short time of flight. The high signal quality of the extracted correlation function g_2 enabled us to probe local phase correlations in areas with a certain density. Now that we have tested our evaluation scheme and understood the main contributions to measured density correlations after time of flight, we will apply the developed methods to locally probe the BKT transition in a 2D Bose gas. First, we will determine the critical point of the BKT transition. Afterwards, we will extract quantitative information about the local decay of phase correlations to obtain the algebraic scaling exponent.

4.2.1 Critical point of the BKT transition

Previous studies of the critical point of the BKT transition relied on the onset of a bimodal density distribution in time of flight [46, 94] or universal scaling near the transition [58]. Here, local probing of phase fluctuations allows us to determine the critical point which marks the characterising feature of the BKT transition: the transition from exponentially to algebraically decaying phase correlations.

As described in section 3.2.2 we evaluate density-density correlations after short time of flight on areas of a specific density. We measure the value of the minimum in $g_2(r)$ for a range of densities and expansion times $t = 0.5$ ms and $t = 1$ ms as shown in Fig. 4.8. For both expansion times, the minimum value of g_2 increases with decreasing density as expected. For densities below a density $n_c = (1.1 \pm 0.1) \mu\text{m}^{-2}$ there is no change in the minimal value anymore. Below the critical density n_c the coherence length ξ drops below the characteristic length scale $\sqrt{\hbar t/m}$. Therefore, smaller values of ξ in areas of lower densities have no effect on the imaged density fluctuations and the behaviour of g_2 remains unchanged for lower density $n < n_c$. Thus, we interpret n_c as the critical density for the BKT transition. To calculate the critical phase space density $(n\lambda_T^2)_c$ we extract the temperature of the cloud from its momentum distribution obtained via the $T/4$ -method described in 4.1.2. We obtain $T \approx 24$ nK and get

$$(n\lambda_T^2)_c = 11.6 \pm 1.1 \quad (4.25)$$

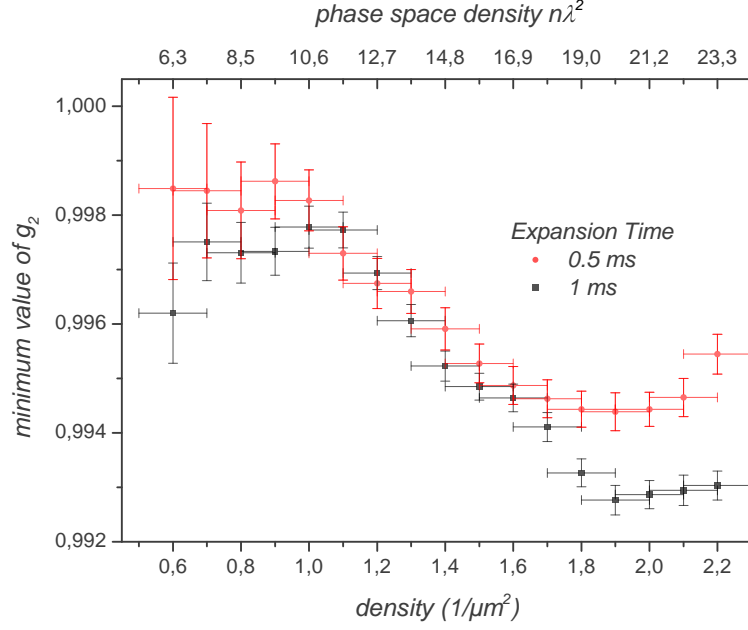


Figure 4.8: Critical point of the BKT transition in a strongly interacting Bose gas. The minimum value of g_2 is tracked for various densities for expansion times $t = 0.5$ ms and $t = 1$ ms. Below a density of $n_c = (1.1 \pm 0.1) \mu\text{m}^{-2}$ the minimum which is clearly visible for higher densities disappears. Using the measured temperature $T \approx 24$ nK we associate n_c with the critical phase space density $(n\lambda_T^2)_c = 11.6 \pm 1.1$.

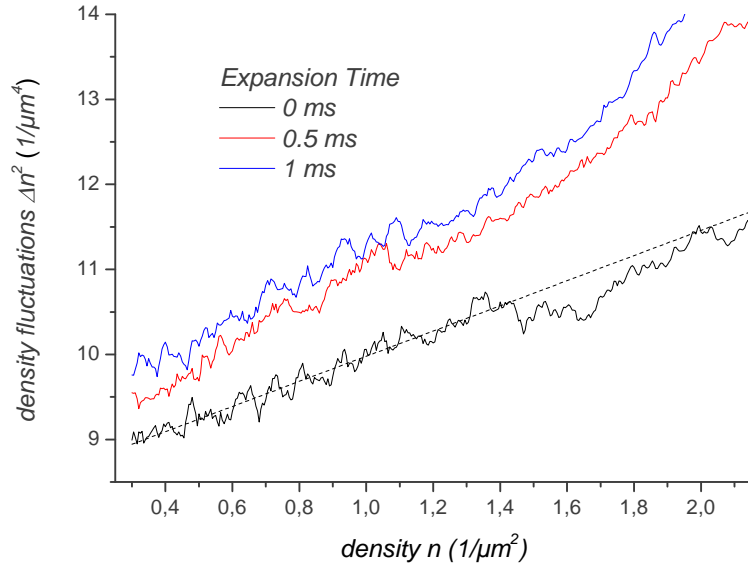


Figure 4.9: Density fluctuations after time of flight. We measure density fluctuations $\Delta n^2(n)$ on individual pixels with mean density n for the in-situ distribution $t = 0$ ms and expanded clouds after $t = 0.5$ ms and $t = 1$ ms respectively. We perform a moving average on the data. Fluctuations are suppressed above $n \approx 1.3 \mu\text{m}^{-2}$ for the in-situ distribution and above $n \approx 1.1 \mu\text{m}^{-2}$ for both expansion times. The linear behaviour of fluctuations in the low-density regime of the in-situ distribution is indicated by the dashed line.

While the theoretical prediction 3.16 for the critical phase space density by Prokofev et al. [80] was calculated for the weakly interacting regime it is interesting to make a comparison here. We prepare a strongly interacting Bose gas with an interaction parameter $\tilde{g} \approx 2.7$ and would expect $(n\lambda_T^2)_c \approx 5$ according to eq. 3.16 which is considerably lower than our measured value. Consequently, the effect of strong interaction on superfluidity cannot be understood by extrapolating from the weakly interacting regime.

We note that the critical point determined here is sensitive to our density calibration. In future experiments, we could check the validity of our results by preparing a gas with a higher temperature. While the total density n at the transition point will be higher, the critical phase space density $(n\lambda_T^2)_c$ should remain unchanged. Here, we will concentrate on the onset of a quasi-condensate as a cross-check of our results.

We directly access the quasi-condensate density as defined in 3.15 by studying density fluctuations Δn around the mean density n of single pixels of our absorption images. In Fig. 4.9, we see a kink of $\Delta n^2(n)$ at a density $n \approx 1.3 \mu\text{m}^{-2}$ for the in-situ distribution and at $n \approx 1.1 \mu\text{m}^{-2}$ for both expansion times $t = 0.5 \text{ ms}$ and $t = 1 \text{ ms}$. The critical density for suppression of density fluctuations in the in-situ image suggests that a quasi-condensate occurs at a comparable point as the BKT transition. This is quite remarkable since the density fluctuations analysed here are analysed on individual pixels and thereby occur on a very different length scale than density fluctuations due to phase correlations.

It is interesting to note that for low density part of the in-situ distribution we have $\Delta n^2 = (1.48 \pm 0.03) n$, which for a pixel size of $0.8 \mu\text{m} \times 0.8 \mu\text{m}$ corresponds to a particle number fluctuation of $\Delta N^2 = (0.95 \pm 0.02) N$ in good agreement with the expected scaling of shot noise $\Delta N^2 = N$. In hindsight, this might justify our density calibration of absorption images. However, the exact value of the fluctuation amplitude is affected by photon shot noise and technical noise, which we did not consider here. Therefore our result for ΔN^2 rather serves as a rough estimate than an accurate determination.

4.2.2 Revealing the algebraic decay of phase correlations

While the previous section used only the minimum value of g_2 to determine the critical point, we will now analyse the overall behaviour of spatial density correlations. The main quantity for the following analysis is the power spectrum p , which we calculate as described in section 4.1.3. By comparing our results to the recent theoretical study by Singh et al. [75], we find evidence for the algebraic decay of phase correlations and determine the scaling exponent τ which determines the decay of phase correlations in the superfluid phase.

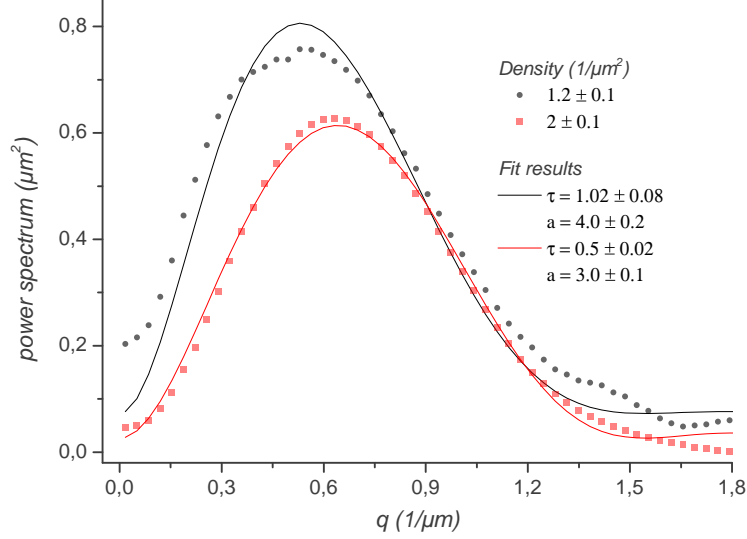


Figure 4.10: Extracting the scaling exponent and cutoff from the power spectrum. After an expansion of $t = 0.5$ ms we locally evaluate $g_2(r)$ in an area of constant density $n = (1.1 \pm 0.1) \mu\text{m}^{-2}$ [$n = (2.0 \pm 0.1) \mu\text{m}^{-2}$] in a 2D Bose gas with temperature $T = 24$ nK. We evaluate the power spectrum $p(q)$ by Fourier transformation of $g_2(\mathbf{r})$ restricted to values $r < r_{max} = 15[25]$ px and subsequent radial averaging. We fit the data using expression 4.26 to obtain the algebraic scaling exponent τ and the cutoff a which determine the decay of phase correlations in a 2D Bose gas.

Fitting the power spectrum of spatial density correlations

There is a very illustrative theoretical prediction made in Ref. [75], for the power spectrum of density-density correlations after a free expansion time t in the superfluid phase, i.e. $T < T_{BKT}$:

$$p(q) \approx \frac{\pi a \tau K_1(aq)}{q} \left(\frac{a^2}{a^2 + q^2 \hbar^2 t^2 / m^2} \right)_{alg}^{\tau/4} \left(1 - \cos \left(\frac{q^2 \hbar t}{m} \right) \right)_{MF} \quad (4.26)$$

Expression 4.26 contains a mean field (MF) part that roughly determines the position of the maximum around $1/q = \sqrt{\hbar t / m}$ as explained in section 3.2. Further, the algebraically decaying phase correlation function g_1 of eq. 3.7 directly appears as a factor (alg) where r is replaced by $q^2 \hbar^2 t^2 / m^2$. The prefactor which contains the first order Bessel function K_1 is a result of the cutoff length a . We will fit our experimental results with eq. 4.26 to extract the algebraic scaling exponent τ and the cutoff length a . While expression 4.26 was derived to first order in τ , the authors of Ref. [75] showed that it is a good approximation to numerical results in the full range $0 < \tau < 1$.

In principle, one could fit the low-momentum part of the power spectrum only, which should be independent of the cutoff a and contain the scaling exponent τ as

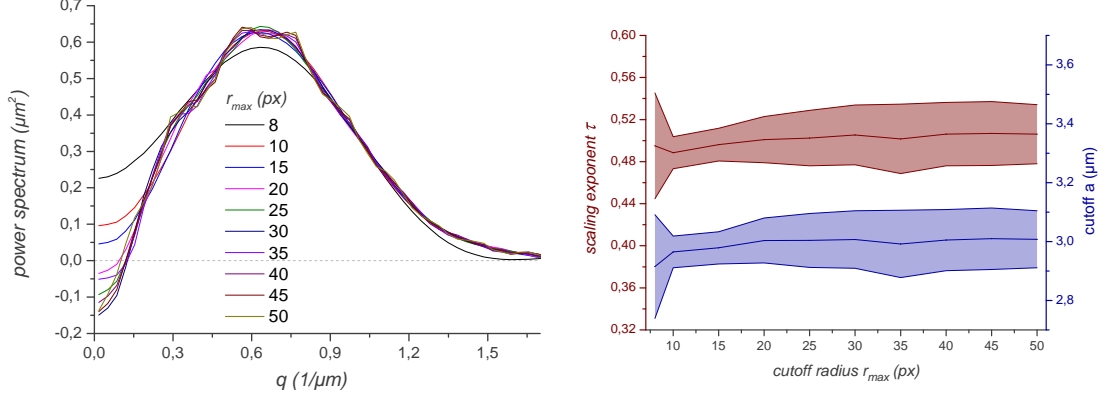


Figure 4.11: Effect of evaluation radius r_{max} on the power spectrum. $p(\mathbf{q})$ shows less low-momentum noise when restricting the area to the physically significant part only. When r_{max} is set too low we get unphysical contribution to the low momentum part of the spectrum. When r_{max} is set too high we pick up significant overall noise on the signal. The main behaviour of $p(\mathbf{q})$ remains unchanged for in a large interval of r_{max} which is indicated by the obtained parameters τ and a .

the only free parameter:

$$p(q) \approx \pi\tau \frac{\hbar^2 q^2 t^2}{2m^2} . \quad (4.27)$$

However, we saw in section 4.1.4 that the signal to noise ratio of the low-momentum part is in general quite poor and sensitive to the chosen evaluation radius r_{max} . We can understand this behaviour as the result of analysing fluctuations on restricted areas, which effectively introduces a low-momentum cutoff. Section 4.1.4 showed that while in principle we can cover fluctuations on length scales on the order of the evaluation area, the signal to noise ratio decreases for larger distancences. Therefore, we set $g_2(r) = 1$ for all values $r > r_{max}$ for our calculation of the power spectrum $p(\mathbf{r})$ as described in section 4.1.4. Figure 4.11 shows how the cutoff radius r_{max} affects the calculated power spectrum. When r_{max} is set too low we obtain unphysical low-momentum contributions corresponding to the cutoff length. We obtain the optimal value for r_{max} when the low-momentum contribution vanishes while the behaviour of $p(q)$ for larger q remains the same. When the cutoff r_{max} is set to even larger values the signal to noise decreases significantly. As we are actively removing a part of the data in g_2 we need to be very careful not to affect any physical information in $p(\mathbf{q})$. Here, we use the full expression 4.26 to fit $p(\mathbf{r})$ and check the dependence of the fit results on r_{max} . We observe that the fit parameters a and τ remain unchanged within a large interval of r_{max} .

Finally, we apply the method described above to obtain the power spectrum for a fixed expansion time $t = 0.5$ ms and varying density $n = 0.7 \mu\text{m}^{-2} - 2.2 \mu\text{m}^{-2}$ with intervals of $\Delta n = 0.2 \mu\text{m}^{-2}$. As the density is decreased the peak value of the power spectrum increases and occurs at lower momenta resulting in a steeper rise for low q (s.Fig 4.10). A comparison with eq. 4.27 indicates that the scaling exponent τ increases towards lower densities. In general, we observe excellent agreement with

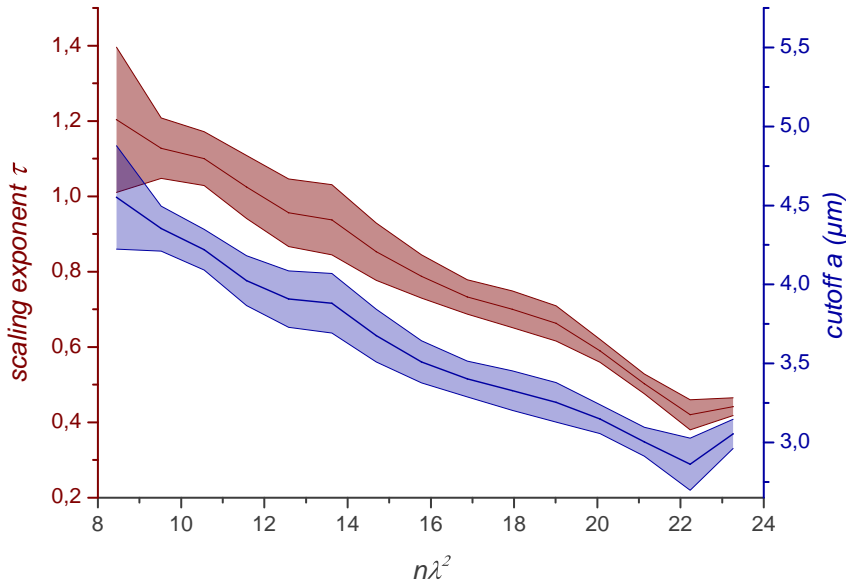


Figure 4.12: Algebraic scaling exponent and cutoff length in a strongly interacting 2D Bose gas. We locally evaluate the power spectrum $p(q)$ in a 2D Bose with temperature $T = 24\text{nK}$ after short expansion $t = 0.5$ ms on areas of constant density $n = (0.8 - 2.2)/\mu\text{m}^{-2} \pm 0.1\mu\text{m}^{-2}$ as illustrated in Fig. 4.10. By fitting $p(q)$ with the expression 4.26 we obtain the algebraic scaling exponent τ and the cutoff length a in dependence of local phase space density $n\lambda_T^2$.

the full expression 4.26 over the full range of densities. We therefore observe a signature of algebraically decaying phase correlations. Further, we expect that our method constitutes a reliable determination of the scaling exponent. As expected, the value of τ significantly increases in areas of lower density as can be seen in Fig. 4.12. For $n = (1.1 \pm 0.1)\mu\text{m}^{-2}$ corresponding to $n\lambda_T^2 = 11.5 \pm 1.0$ we obtain $\tau \approx 1$ consistent with the determination of the critical point in section 4.2.1. Since expression 4.26 is only valid for $\tau < 1$ we cannot quantify the regime of exponentially decaying correlations. Here, a quantitative analysis might reveal the exponential divergence of the correlation length ξ as outlined in the introduction.

Reconstructing the superfluid density of a trapped 2D Bose gas

One of the most remarkable features of the BKT transition is the jump of the superfluid density at a universal critical point $n_s\lambda_T^2 = 4$. In a trapped system using the local density approximation we expect the jump to occur at a certain distance from the cloud's center. Therefore the superfluid density should be distributed mainly over the central region, while the thermal component can in principle stretch over the whole system⁴. So far, the value of the local superfluid density was an inaccessible quantity in two-dimensional quantum gases. Here, we assume that the

⁴A mean field analysis of scattering between superfluid and thermal atoms shows that the thermal part is actually repelled by the superfluid component to the outer part of the cloud

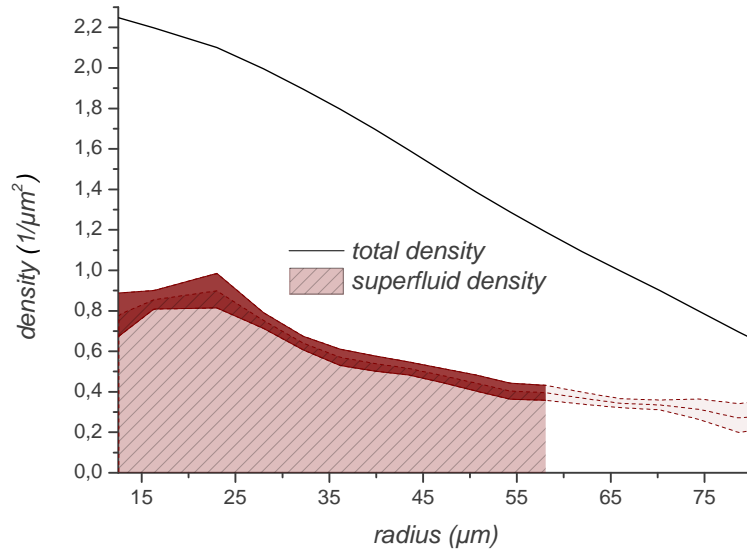


Figure 4.13: Superfluid density reconstructed from the algebraic scaling exponent. We extract the scaling exponent τ from the power spectra as shown in Fig. 4.12. The superfluid density n_s is calculated via $n_s \lambda_T^2 = 4/\tau$ using the temperature $T = 24$ nK obtained from the momentum distribution described in section 4.1.2. We use the radial total density from in-situ images as a reference. The dashed red line corresponds to $\tau > 1$ where eq. 4.26 is not valid and we expect the superfluid density to drop to zero.

fundamental prediction of BKT theory for the long-range decay of phase correlations as described by eq. 3.7 holds. Thereby, we can use the values of the algebraic scaling exponent $\tau(n)$ to deduce the local superfluid density n_s in a trapped 2D Bose gas as show in Fig. 4.13. Overall the deduced superfluid component follows the behaviour of the total density in the center of the cloud. Further, the total superfluid part seems in good agreement with the quasi-condensed fraction shown in Fig. 4.2.

Robustness to different expansion times

Next, we evaluate density-density correlations from another expansion time $t = 1$ ms. In principle, considering multiple expansion times provides an important cross-check of our method and might allow us to study the delocalisation of the superfluid component. However, as already pointed out in section 4.1.5 we expect that the contrast in interference is reduced due to our limited depth of field compared to the large size of the cloud in axial direction. Indeed, as can be seen in Fig. 4.14, the application of expression 4.26 delivers results for the scaling exponent τ which are systematically below the values obtained for a shorter expansion time $t = 0.5$ ms. In general, one should reduce the fast expansion in axial direction as show in Fig. 4.7. Here, we preliminarily introduce a prefactor $D = 0.6$ for expression 4.26 to account for the limited depth of field as explained in section 4.1.5. The

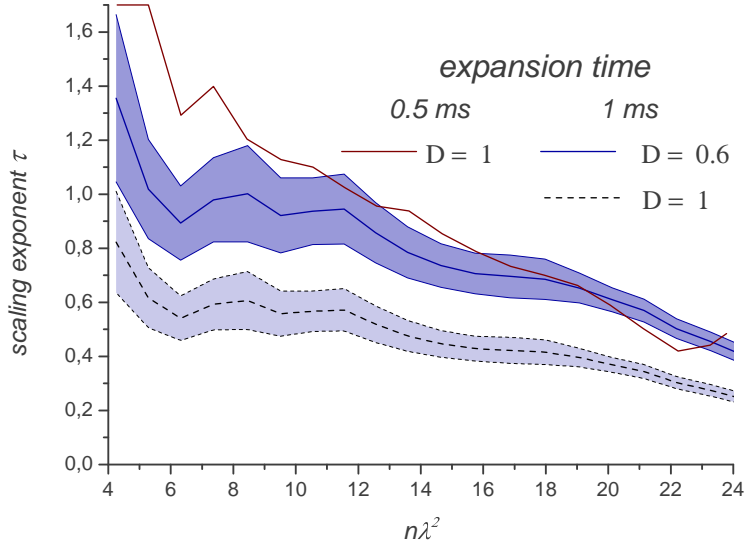


Figure 4.14: Algebraic scaling exponent for different expansion times. We locally evaluate the power spectrum $p(q)$ in a 2D Bose with temperature $T = 24$ nK after short expansion $t = 1$ ms on areas of specific density $n = (0.8 - 2.2)/\mu\text{m}^{-2} \pm 0.1$ per $\mu^2\text{m}$. We introduce a scaling factor D as described in section 4.1.5 to account for the limited depth of field of our imaging setup and fit our results with $D \cdot p(q)$ as in Fig. 4.10. By choosing $D \approx 0.6$ we can approximately recover the results for the algebraic scaling exponent τ obtained for a shorter expansion time of 0.5 ms for large phase space density $n\lambda_T^2$. The overall scaling of τ needs to be checked in future experiments by considering several expansion times below 0.5 ms.

prefactor is chosen in such a way that the scaling exponent τ obtained from a longer expansion time $t = 1$ ms matches the scaling exponent obtained from the shorter expansion time $t = 0.5$ ms. Fig. 4.14 shows that the overall behaviour of the superfluid density for both expansion times matches reasonably well. Still, the overall value of τ needs to be checked using even shorter expansion times $t < 0.5$ ms and the described method in section 4.1.5 to suppress the expansion in axial direction. Finally, a reliable determination of the scaling exponent for different expansion times might allow us to reconstruct the time-dependent behaviour of the superfluid density. When the strongly confining lattice is suddenly turned off we expect that the assumed sharp edge in the superfluid density is not maintained and the superfluid should delocalise to larger radii.

4.3 Summary and outlook

In the previous chapters we have described how we locally probe phase correlations in a strongly interacting 2D Bose gas. We prepare a single two-dimensional layer of an ultracold Fermi gas of ${}^6\text{Li}$. Using a Feshbach resonance we create a strongly interacting Bose gas of ${}^6\text{Li}$ dimers. After suddenly switching off the strongly confining lattice potential phase fluctuations transform into density fluctuations. We evaluate density-density correlations after a certain expansion time to probe the decay of phase correlations. Since our high-resolution imaging system allows us to resolve density fluctuations after short expansion times the cloud's shape does not deviate significantly from its in-situ distribution. This enables us to locally probe phase fluctuations in areas of specific density. In the central region of the cloud corresponding to high densities we observe evidence for the algebraic decay of phase correlations predicted for the superfluid phase in 2D. In outer regions of the cloud corresponding to low densities we find evidence for the phase transition where phase correlations decay on short length scales. We extract the total critical phase space density $(n\lambda_T^2)_c = 11.6 \pm 1.1$ in the strongly interacting regime with $\tilde{g} \approx 2.7$. We obtain the cloud's temperature from the thermal wings which are clearly visible in the momentum distribution. The momentum distribution is obtained by expanding the gas for a time $t = T/4$ in a weak magnetic trap with frequency $\omega = 2\pi/T$. By calculating the power spectrum of density-density correlations in areas of specific density n we are able to extract the algebraic scaling exponent and the microscopic cutoff length over a wide range in phase space density $n\lambda_T^2 = 8 - 23$. The scaling exponent significantly increases for decreasing $n\lambda_T^2$ and reaches values consistent with 1 around the critical point.

The local evaluation of density-density correlations could be successfully tested using test distributions with imprinted correlations. Further, we discussed limiting physical factors in our analysis. While shot noise contributions can be easily subtracted, the limited depth of field of our imaging system may be a major complication for the extraction of reliable quantitative results. We could successfully implement a laser pulse to significantly slow down the quick expansion of the cloud in axial direction. Using this pulse in combination with several different expansion times we are optimistic to fully reconstruct the decay of phase correlations in a strongly interacting 2D Bose gas.

Our measurement marks an important step to test the predicted connection between the superfluid density n_s and the decay of phase correlations: $\tau = 4/n_s\lambda_T^2$. The reason for the lack of quantitative studies of the BKT transition and its connection to superfluidity lies in the difficult detectibility of the superfluid density. According to Landau's two-fluid model⁵ the total density n is the superposition of a thermal and a superfluid component [98]. We cannot directly image the superfluid component because absorption images only probe the total density of an

⁵The two-fluid model was originally proposed to describe liquid helium films, but is also accurate for the description of strongly interacting two-dimensional quantum gases

atomic gas. Instead, one can study excitations as a probe of superfluidity. An intriguing possibility to access the superfluid component lies in the excitation of second sound, in which the superfluid and normal part of the gas oscillate out of phase. In a recent experiment by Sidorenkov et al. [99] second sound was observed in a strongly interacting Fermi gas and used as a probe of the superfluid density. So far second sound could not be observed in any 2D system [100].

Another possibility to access the superfluid density in 2D can be achieved by moving an obstacle through the cloud and observe the onset of dissipation above a critical velocity v_c as predicted by the Landau criterion. Recently, Desbuquois et al. [65] used a red-detuned laser beam as a local perturbation to probe superfluidity in a 2D Bose gas. Besides the striking evidence for superfluidity, they found evidence for the superfluid jump by stirring the cloud in areas of different density. In future experiments, we plan to probe superfluidity in a 2D Fermi gas similarly to the experiment by Desbuquois et al. [65] and our recent experiment in 3D [15] which is presented in chapter 5. In combination with the results of the present chapter, we should be able to test the connection between phase correlations and superfluid density as predicted by BKT theory.

Shortly before submitting this thesis, we conducted another set of measurements to access the algebraic scaling exponent. Preliminary results suggest an additional dependence on the detuning of the imaging light and the position of the imaging objective in axial cloud direction. Further, the effect of in-situ density fluctuations and interaction effects during expansion were not considered in this chapter. Eventually, a reliable determination of the scaling exponent requires a full account of imaging artefacts and physical complications during the initial expansion. At the moment, we are performing systematic studies of imaging effects. Additionally, we analyse spatial density correlations after several short expansion times to understand the initial evolution from phase to density fluctuations. As demonstrated in the previous chapters, we can extract local density-density correlations with high precision. We are therefore optimistic to provide a detailed analysis of in-situ phase correlations in future investigations.

5 The critical velocity in the BEC-BCS crossover

Superfluidity is one of the most remarkable examples of collective behaviour in quantum systems. Obstacles moving through a superfluid with a speed below a certain critical velocity do not excite the quantum system. Here, we determine the critical velocity in an ultracold gas of ${}^6\text{Li}$ in the BEC-BCS crossover. I took part in the measurements of the speed of sound which serves as a reference for the critical velocity. Additionally, I contributed to the derivation of the theoretical prediction for the speed of sound in the BEC-BCS crossover based on the $T = 0$ equation of state by Astrakharchik et al. [54]. Further, I took part in verification measurements of the critical velocity. The following section was initially published as a preprint [15] and is reprinted without modifications.

The critical velocity in the BEC-BCS crossover

Wolf Weimer,¹ Kai Morgener,¹ Vijay Pal Singh,^{1,2,3} Jonas Siegl,¹ Klaus Hueck,¹ Niclas Luick,¹ Ludwig Mathey,^{1,2,3} and Henning Moritz¹

¹*Institut für Laserphysik, Universität Hamburg, Luruper Chaussee 149, 22761 Hamburg, Germany*

²*Zentrum für Optische Quantentechnologien, Universität Hamburg,*

Luruper Chaussee 149, 22761 Hamburg, Germany

³*The Hamburg Centre for Ultrafast Imaging, Luruper Chaussee 149, 22761 Hamburg, Germany*

We map out the critical velocity in the crossover from Bose-Einstein condensation (BEC) to Bardeen-Cooper-Schrieffer superfluidity with ultracold ⁶Li gases. A small attractive potential is dragged along lines of constant column density. The rate of the induced heating increases steeply above a critical velocity v_c . In the same samples, we measure the speed of sound v_s by exciting density waves and compare the results to the measured values of v_c . We perform numerical simulations in the BEC regime and find very good agreement, validating the approach. In the strongly correlated regime, where theoretical predictions only exist for the speed of sound, our measurements of v_c provide a testing ground for theoretical approaches.

PACS numbers: 03.75.Kk, 03.75.Ss, 05.30.Fk, 67.85.Lm

Frictionless flow of charged or neutral particles is one of the most striking macroscopic phenomena arising from quantum physics. Its appearance is remarkably widespread, ranging from superconductivity in solids to superfluidity in liquids and dilute gases with flow of either bosonic or fermionic particles. For technological applications, stability against thermal fluctuations or external perturbations is crucial. The corresponding quantities, i. e. critical temperature and critical velocity, are typically highest in the strongly correlated regime, where the interactions stabilizing the many-body state are particularly strong. Attaining a full understanding of the underlying microscopic mechanisms in this regime is one of the major challenges of modern physics. Ultracold atomic gases have emerged as an excellent platform to study the influence of microscopic physics on macroscopic observables [1–4].

Here, we explore the stability of superfluids against external perturbation in the crossover from Bose-Einstein condensation (BEC) of composite bosons to Bardeen-Cooper-Schrieffer (BCS) pairing of fermions. An obstacle consisting of a small attractive potential is moved through an oblate superfluid gas. Above a critical velocity heating is observed, as shown in Fig. 1. For a pointlike weak perturbation, the Landau criterion $v_c = \min_p(\epsilon(p)/p)$ makes the direct connection between the critical velocity v_c as a macroscopic observable and the microscopic excitations of the system with energy $\epsilon(p)$ and momentum p . One source of heating is the excitation of phonons. For these excitations, the Landau criterion predicts that the critical velocity equals the sound velocity v_s , which can be calculated within the Bogoliubov approximation for a weakly interacting Bose gas. Consequently, we measure v_s as well by exciting and tracking density modulations. The obtained results are compared to the critical velocities.

Previously, v_c has been measured in ultracold Bose and

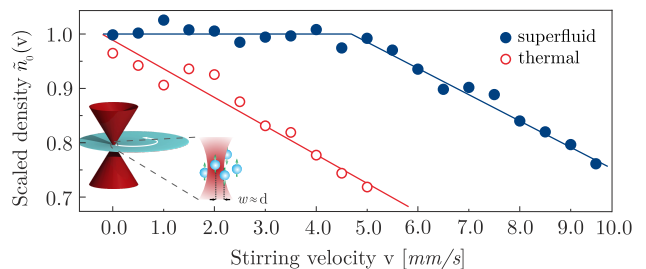


FIG. 1: A red detuned laser beam with waist w moves through the cloud with velocity v , where the obstacle size is on the order of the inter-particle separation d (inset). After stirring, the column integrated density $\tilde{n}_0(v)$ at the center of the cloud is reduced for $v > v_c$ compared to the unperturbed value, indicating heating. For a superfluid gas (blue circles), the critical velocity v_c can be determined from a bilinear fit (blue line) and in a thermal cloud (red circles and line), no critical velocity can be observed. The data is acquired at $B = 806$ G, $a = 13500 a_0$ with $\tilde{n}_0 = 1.11 \mu\text{m}^{-2}$, $N = 6100$ for the superfluid.

Fermi gases. Weakly interacting three-dimensional [2] and two-dimensional [3] BECs were probed with moving repulsive obstacle potentials and critical velocities of 10 % and 60 % of the Bogoliubov sound velocity were found. It is expected that vortex excitations limited v_c [5] since the healing length was much smaller than the obstacle size. In Fermi gases, v_c was determined in the BEC-BCS crossover by subjecting the cloud to a moving optical lattice [6]. A comparison with theory was performed at the universal point yielding $v_c \approx 70\% v_s$. The precise microscopic excitation mechanism is not fully understood yet, but theoretical analyses [7] suggested that it is quite different from the one relevant in our measurements. In the crossover, v_s was measured as well [8]. However, in those experiments no comparison to v_c was made.

Due to the high optical resolution and low densities

achieved in our apparatus, it is finally possible to manipulate and probe superfluids on their intrinsic length scales. The obstacle size is on the order of the healing length in the BEC regime, the coherence length in the BCS regime, and the inter-particle separation in the crossover. Our main results are shown in Fig. 2: they consist of measurements of v_c , v_s , and a detailed comparison with theory in the entire crossover. The results for v_s are in very good agreement with the theoretical prediction. In the BEC regime, the critical velocity is found to be significantly smaller than v_s but in excellent agreement with numerical simulations. The simulations take all experimental details into account and allow us to determine the origins of the reduction. Having validated the method in the BEC regime, our results in the strongly correlated regime may provide valuable benchmarks for theory. In the BCS regime, pair-breaking excitations are expected to limit v_c and our results are in qualitative agreement.

We prepare ${}^6\text{Li}$ atoms with mass m in a balanced mixture of the two lowest hyperfine states with a similar procedure as described in Ref. [9]. Ultimately, the atoms are trapped in a highly elliptical optical dipole trap with a beam waist of $10\ \mu\text{m} \times 370\ \mu\text{m}$ and a wavelength of $1064\ \text{nm}$. Typical trap frequencies are $\omega_z \approx 2\pi \cdot 550\ \text{Hz}$ and $\omega_r \approx 2\pi \cdot 30\ \text{Hz}$ in the vertical and radial direction. The radial confinement is mainly caused by the curvature of a radially symmetric magnetic field. We adjust the final evaporation to obtain a constant line of sight integrated central density of $\bar{n}_0 = (1.15 \pm 0.05)\ \mu\text{m}^{-2}$ per spin state. Depending on the interaction strength, this corresponds to a total atom number N of 2500 to 14000 per spin state. We estimate the systematic errors on atom numbers and densities to be approximately $\pm 20\%$. Although the vertical confinement dominates, effects caused by reduced dimensionality are negligible since $E_F/\hbar\omega_z > 4.2$ in all measurements, where the Fermi energy E_F and wavevector k_F are defined as $E_F = \hbar^2 k_F^2/2m = \hbar(\omega_r^2 \omega_z \cdot 6N)^{1/3}$. A measure for the temperature T is provided by the observed condensate fractions in the BEC regime of approximately 80%. Since we observe no significant heating during magnetic field ramps, we use the theory in Ref. [10] to estimate the temperature in the BCS regime, yielding values of $T/T_F \approx 7\%$.

In the actual stirring experiment, a red-detuned laser beam forms an attractive potential. This obstacle traces out a circular trajectory with speed v and radius $r = 10\ \mu\text{m}$ along lines of constant column density $\tilde{n}(r) \approx \tilde{n}_0$ within the superfluid core. The beam has a wavelength of $780\ \text{nm}$ and is focused to a waist w of $2.4\ \mu\text{m} \times 1.9\ \mu\text{m}$, a size comparable to the interparticle distance $d = n^{-1/3} \approx 1.5\ \mu\text{m}$ at unitarity. The relative column integrated density increase in the focus is approximately 85%. The corresponding beam powers were adjusted depending on the interaction strength.

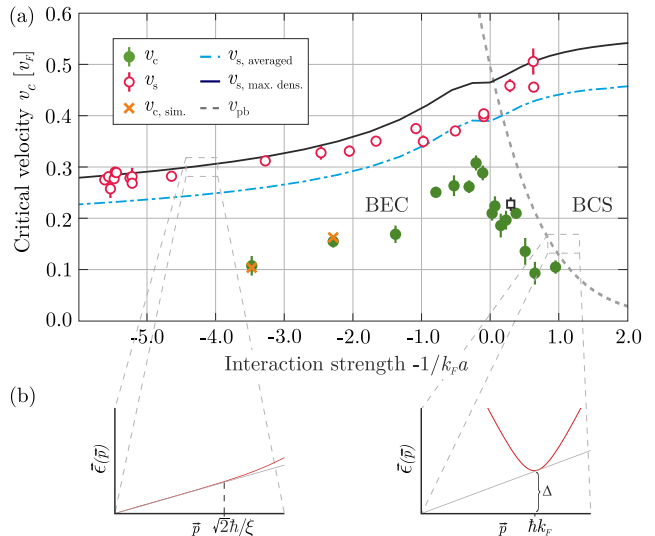


FIG. 2: (a) Critical velocity v_c (green filled circles) and speed of sound v_s (red open circles) in units of the Fermi velocity v_F throughout the BEC-BCS crossover. The error bars correspond to the fit errors. A statistical error for v_c (black open square) was determined from five measurements. The simulated critical velocities are marked with crosses. The solid (dot-dashed) curve is the theory prediction for v_s assuming that the maximum (column averaged) density is relevant for sound propagation, see main text. The pair breaking velocity v_{pb} providing an upper bound for v_c in the BCS regime is plotted with a dashed line. (b) Dispersion relations for the BEC and the BCS limiting cases (red) and the tangent to this curve from the origin to visualize the Landau criterion (grey).

The stirring sequence proceeds as follows: first, the scattering length a is set to the desired value by ramping the magnetic field to a value between 750 G and 890 G close to a broad Feshbach resonance, followed by 50 ms thermalization time. Next, the power of the moving obstacle beam is linearly ramped up within 10 ms and the gas is stirred for 200 ms before the power is linearly ramped down in 5 ms. After 100 ms thermalization time the magnetic field is ramped to 680 G in 100 ms and an in-situ absorption image of the atoms is acquired. We repeat this sequence typically ten times for each speed v and extract the radially averaged and line of sight integrated density distribution $\tilde{n}(r)$ from the mean of those datasets, accounting for optical saturation effects [11]. Since the gas is well in the BEC regime at the time of imaging, we determine the central column density $\tilde{n}_0(v)$ as well as the condensate fraction from a bimodal fit. Heating is indicated by a reduction in either, yet $\tilde{n}_0(v)$ is the more robust measure since evaporation upon heating can occur in our trap of finite depth.

We observe a significant reduction in $\tilde{n}_0(v)$ and hence heating only above a threshold velocity which we identify with the critical velocity as shown in Fig. 1. The exact value is obtained from a fit with a continuous bilinear

function [6]. It has a constant value of \tilde{n}_0 below v_c and decreases linearly above, see blue line in Fig. 1. The figure also shows that stirring within the thermal region of the cloud leads to heating for all obstacle speeds.

We determine the critical velocities for different interaction strengths $-1/k_F a$ throughout the whole BEC-BCS crossover and far into the BEC regime and plot them in units of the Fermi velocity v_F in Fig. 2(a). Qualitatively, the data shows a maximum of v_c close to $1/k_F a = 0$ and a decrease towards the BEC and the BCS side of the resonance, in agreement with Ref. [6]. The absolute values range between $1.7 \text{ mm/s} \leq v_c \leq 6.3 \text{ mm/s}$. For comparison we also measure the speed of sound v_s by creating a small density excess in the center of the gas, releasing it and tracking the maximum of the outgoing circular density wave. Here, the stirrer beam is placed at the center of the gas, its power is adiabatically raised to values between $7 \text{ } \mu\text{W}$ and $40 \text{ } \mu\text{W}$ in 100 ms and suddenly switched off.

To compare the experimental results with theoretical predictions, it is convenient to consider three regimes, the BEC, the strongly correlated regime, and the BCS regime. In the latter ($-1/k_F a > 1$), superfluids are formed from loosely bound Cooper pairs. The excitation spectrum is sketched in the r. h. s. of Fig. 2(b). Pair breaking excitations limit the critical velocity to $m v_{pb}^2 = (\Delta^2 + \mu^2)^{1/2} - \mu$ [12]. The pair breaking velocity v_{pb} is plotted as the dashed line in Fig. 2(a), where we determined the gap Δ and the chemical potential μ at $T = 0$ by solving the mean field gap the number equations numerically [13, 14]. The curve can be extended into the strongly correlated regime, where no simple theoretical description exists. Here, the mean field approach can at least provide a rough estimate for v_c and our data appears to be in qualitative agreement. We expect temperature effects to be small since $T/T_c < 0.5$ [15].

Before discussing the strongly correlated regime in depth, which is theoretically largely inaccessible and hence particularly interesting, we benchmark our experiment against theory. In the BEC regime ($-1/k_F a < -1$), the gas forms a molecular BEC of tightly bound dimers. Within Bogoliubov theory the dispersion relation is linear at low momenta with a slope v_s , see l. h. s. of Fig. 2(b), and v_c should equal v_s . The measured sound velocities are in very good agreement with the two theoretical predictions shown in Fig. 2(a). When the sound wavelength is large compared to the vertical extent of the cloud, the wave effectively probes the column averaged density (dot-dashed line), provided the gas is fully hydrodynamic [16]. Otherwise, the wavefront observed should be the one travelling with the speed determined by the maximum density along the z-direction (solid line). Since the gas is only partially hydrodynamic in the vertical direction, we expect the experimental data to lie between the two curves. We note that the measurements of v_s

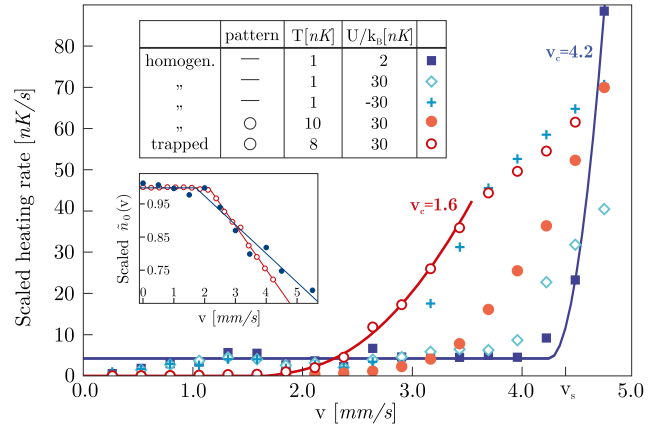


FIG. 3: The simulated heating rates normalized by the stirrer depth U^2 . The complexity is gradually increased: blue squares depict the idealized case of a very cold homogeneous sample stirred with linear pattern. The relative density excess η in the weak stirrer potential $U = k_B \cdot 2 \text{ nK}$ is only 3%. For all datasets, the Bogoliubov result for v_s is 4.4 mm/s. The red open circles depict a simulation of the experimental case: a trapped sample is stirred circularly with a stirrer of realistic depth. A lower temperature is chosen for technical reasons. Here, the y-axis scaling factor is one. In the inset, the results for the heating observed in the central column density $\tilde{n}_0(v)$ are compared. We find very good agreement between the experimental (blue filled circles) and the simulated results (red open circles). The bilinear fits to extract v_c are shown with solid lines. In the inset $U = k_B \cdot 35 \text{ nK}$.

presented here probe a new regime since all previous experiments determining v_s were performed in prolate gas clouds [8] described by effectively one-dimensional hydrodynamics [16]. The theory curves for v_s are obtained by taking thermodynamic derivatives [17] of the equation of state calculated in numerically exact zero-temperature quantum Monte Carlo simulations [18]. The homogeneous theory is applied using the local density approximation: the density distribution in the trap, given by the equation of state, is used to calculate k_F and v_F of the corresponding trapped clouds [19]. Temperature effects should be small since the temperatures in the experiment are smaller than the mean field energy in the BEC regime and the Fermi temperature in the BCS regime [20].

In order to understand the critical velocity in the BEC regime, we perform simulations and identify the factors reducing v_c . These are the finite temperature, the inhomogeneous density profile along the strongly confined direction, the circular instead of linear motion of the stirrer, and to a lesser degree the finite depth of the obstacle potential. We use a classical field method, which is the limiting case of the truncated Wigner method used in Ref. [21]. The time evolution of an ensemble of complex-valued fields is calculated using classical equations of motion. The initial states are generated from a grand canonical ensemble via a classical Metropolis al-

gorithm. We employ a real-space representation on a lattice with $60 \times 60 \times 3$ ($140 \times 140 \times 11$) sites for the simulation of homogeneous (trapped) systems. The discretization length is $1 \mu\text{m}$. All simulations are performed with the same stirring time, stirrer beam size, dimer-dimer scattering length $a_{DD} = 0.6 \times 3634 a_0$, and density $n_{3D} = 0.486 \mu\text{m}^{-3}$ (and column density in the trapped case) as the experimental data point at $-1/k_F a \approx -3.5$. When choosing all remaining parameters, i.e. temperature, confining potential, stirrer depth, and motion in accordance with the experiment, we reproduce the experimentally measured v_c . To disentangle the various features of the system that influence these measurements, it is instructive to start with an idealized case: a homogeneous gas at a low temperature of 1 nK , stirred along a linear path. In this case, the heating rate increases steeply at a critical velocity which is approximately v_s as shown in Fig. 3. To determine v_c , the fit function $A \cdot (v^2 - v_c^2)^2 / v + B$ is used for $v > v_c$ [22], with the free parameters A , B and v_c . The simulated heating rates are in good agreement with the second order perturbation theory that predicts a scaling with U^2 . Moreover, by increasing the stirrer depth U , we observe that the extracted v_c is slightly reduced. These results demonstrate that we work with relatively weak perturbations and that vortex excitations do not limit v_c [5], in contrast to previous experiments in 3D [2] and 2D atomic BECs [3]. The simulations also show that attractive stirrer potentials are preferable to realize a stirrer. For larger repulsive potentials [2, 3] the inherent density reduction strongly reduces the observed critical velocity as shown in Fig. 3.

Next, the effects of the finite experimental temperature and of the circular motion of the stirrer are investigated. The simulations show that both features reduce v_c by approximately 15%. Having both present simultaneously causes a small further reduction of v_c . The reduction at finite temperature might be due to vortex-antivortex excitations, or rotonic precursors of them. As the temperature is increased above the mean field energy, density fluctuations increase and vortices can nucleate at points of minimal density. That the circular motion can reduce v_c can be seen in perturbation theory performed in momentum space: here, the motion of the perturbation consists of a distribution of velocities rather than a single velocity.

Finally, we perform a simulation of an inhomogeneous system in a trap, with a realistic temperature and a circular stirring motion. The simulated critical velocity of $1.6(1) \text{ mm/s}$ agrees excellently with the experimentally measured value of $1.7(3) \text{ mm/s}$, see Fig. 2. We believe that the additional reduction of 39% with respect to the homogeneous simulation result is mainly due to probing lower density regions along the stirrer axis. The results for the central column densities are in good agreement as well, see inset of Fig. 3, considering the experimental

signal to noise.

We now turn to the strongly correlated regime. Due to the lack of a small parameter, perturbation theories are inaccurate and the quasiparticle description breaks down. Hence, the velocities v_s and v_{pb} associated with phonon creation and Cooper pair breaking excitations can only provide upper limits for v_c . We are not aware of a prediction for v_c , even at the universal point where $|a| \rightarrow \infty$. The largest value for v_c we observe is $v_c = 0.31(2) v_F$, close to the universal point, see Fig. 2. Reference [6] found a value of $v_c = 0.31 v_F$ using a different excitation mechanism. These values are considerably smaller than the corresponding $v_s \approx 0.40(1) v_F$ we measure and the theory prediction $v_s = \xi_B^{1/4} / \sqrt{3} v_F = 0.45 v_F$ [14, 23] employing the local density approximation. Very recently, a critical velocity of $v_c = 0.42_{-0.11}^{+0.05} v_F$ was observed in an elongated ${}^6\text{Li}$ gas oscillating with respect to a ${}^7\text{Li}$ BEC [25]. Here, the onset of heating is predicted to occur for a relative velocity that equals the sum of the individual sound velocities [26].

In conclusion, we have demonstrated the breakdown of superfluidity due to moving obstacle across the BEC-BCS transition, for the first time in close analogy to Landau's Gedankenexperiment. We compare the results with theoretical predictions throughout and achieve quantitative understanding in the BEC regime by performing numerical simulations. Pointlike defects also play a role in strongly correlated high temperature superconductors. The experiment presented here provides the opportunity to isolate relevant effects in a very clean and controllable environment. Of particular interest for future studies are strongly correlated two-dimensional superfluids.

We thank N. Strohmaier, J. H. Drewes, and F. Wittkötter for their contributions to early stages of this experiment and J. Dalibard, C. Weitenberg, W. Zwerger, and especially L. Tarruell for stimulating discussions. This work has been supported financially by the Deutsche Forschungsgemeinschaft within SFB 925, GRK 1355, the Hamburg Centre for Ultrafast Imaging, and by the Landesexzellenzinitiative Hamburg, which is supported by the Joachim Herz Stiftung.

-
- [1] I. Bloch, J. Dalibard, and W. Zwerger, *Rev. Mod. Phys.* **80**, 885-964 (2008).
 - [2] C. Raman, M. Köhl, R. Onofrio, D. S. Durfee, C. E. Kulewicz, Z. Hadzibabic, and W. Ketterle, *Phys. Rev. Lett.* **83**, 2502 (1999); R. Onofrio, C. Raman, J. M. Vogels, J. R. Abo-Shaer, A. P. Chikkatur, and W. Ketterle, *Phys. Rev. Lett.* **85**, 2228 (2000).
 - [3] R. Desbuquois, L. Chomaz, T. Yefsah, J. Lonard, J. Beugnon, C. Weitenberg, and J. Dalibard, *Nature Phys.* **8**, 645 (2012).
 - [4] M. W. Zwierlein, J. R. Abo-Shaer, A. Schirotzek, C. H. Schunck, and W. Ketterle, *Nature* **435**, 1047 (2005); A.

- Ramanathan et al., Phys. Rev. Lett. **106**, 130401 (2011).
- [5] J. S. Stieβberger, and W. Zwerger, Phys. Rev. A **62**, 061601 (2000).
- [6] D. E. Miller, J.K. Chin, C. A. Stan, Y. Liu, W. Setiawan, C. Sanner, and W. Ketterle, Phys. Rev. Lett. **99**, 070402 (2007).
- [7] G. Watanabe, F. Dalfovo, F. Piazza, L. P. Pitaevskii, and S. Stringari, Phys. Rev. A **80**, 053602 (2009); Y. Yunomae, I. Danshita, D. Yamamoto, N. Yokoshi, and S. Tsuchiya, J. Phys.: Conf. Ser. **150**, 032128 (2009); G. Watanabe, F. Dalfovo, L. P. Pitaevskii, and S. Stringari, Phys. Rev. A **83**, 033621 (2011).
- [8] J. Joseph, B. Clancy, L. Luo, J. Kinast, A. Turlapov, and J. E. Thomas, Phys. Rev. Lett. **98**, 170401 (2007); M. Horikoshi, S. Nakajima, M. Ueda and T. Mukaiyama, Science **327**, 442 (2010); L. A. Sidorenkov, M. K. Tey, R. Grimm, Y.-H. Hou, L. P. Pitaevskii and S. Stringari, Nature **498**, 78 (2013).
- [9] B. Zimmermann, T. Müller, J. Meinecke, T. Esslinger, and H. Moritz, New J. of Phys. **13**, 043007 (2011).
- [10] L. D. Carr, G.V. Shlyapnikov, and Y. Castin, Phys. Rev. Lett. **92**, 150404 (2004).
- [11] G. Reinaudi, T. Lahaye, Z. Wang, and D. Gury-Odelin, Opt. Lett. **32**, 3143-3145 (2007).
- [12] R. Combescot, M. Y. Kagan, and S. Stringari, Phys. Rev. A **74**, 042717 (2006).
- [13] M. Marini, F. Pistolesi, and G. Strinati, The European Physical Journal B **1**, 151-159 (1998).
- [14] S. Giorgini, L. P. Pitaevskii, and S. Stringari, Rev. Mod. Phys. **80**, 1215 (2008).
- [15] B. Mühlischlegel, Zeitschrift für Physik **155**, 313-327 (1959).
- [16] P. Capuzzi, P. Vignolo, F. Federici, M.P. Tosi, Phys. Rev. A **73**, 021603(R) (2006); G. Bertaina, L. P. Pitaevskii, S. Stringari, Phys. Rev. Lett. **105**, 150402 (2010); T.K. Ghosh, and K. Machida, Phys. Rev. A **73** 013613 (2006).
- [17] N. Manini, and L. Salasnich, Phys. Rev. A **71**, 033625 (2005), Eq. (9). The change of slope at $1/k_F a = 0$ is an artefact of the parametrization used to approximate the QMC data analytically.
- [18] G. E. Astrakharchik, J. Boronat, J. Casulleras, and S. Giorgini, Phys. Rev. Lett. **93**, 200404 (2004).
- [19] Please note that the commonly accepted definition of k_F used also here is not trivially connected to the density.
- [20] H. Heiselberg, Phys. Rev. A **73**, 013607 (2006).
- [21] A. C. Mathey, C. W. Clark, and L. Mathey, Phys. Rev. A **90**, 023604 (2014).
- [22] G. E. Astrakharchik, and L. P. Pitaevskii, Phys. Rev. A **70**, 013608 (2004).
- [23] The Bertsch parameter $\xi_B = 0.37$ is determined in [24].
- [24] M. Ku, A. Sommer, L. Cheuk, and M. Zwierlein, Science **335**, 563 (2012); G. Zürn, T. Lompe, A. N. Wenz, S. Jochim, P. S. Julienne, and J. M. Hutson, Phys. Rev. Lett **110**, 135301 (2013).
- [25] I. Ferrier-Barbut, M. Delehaye, S. Laurent, A. T. Grier, M. Pierce, B. S. Rem, F. Chevy, and C. Salomon, Science 1255380 Published online 17 July 2014.
- [26] Yvan Castin, Igor Ferrier-Barbut, Christophe Salomon, 2014, eprint arXiv:condmat/1408.1326.

6 The speed of sound in a strongly-interacting 2D Fermi gas

The propagation of sound is a manifestation of collective behaviour in quantum systems. We measure the speed of sound in a 2D ultracold gas of ${}^6\text{Li}$ in the BEC-BCS crossover and compare our results to values obtained from the equation of state (EOS) which we determine from in-situ density distributions. Similarly to our measurements in 3D [15], the speed of sound may serve as a reference for future studies of the critical velocity in a 2D Fermi gas. A detailed description of our measurements and results will appear in the PhD thesis by Kai Morgener [19]. In the following, I will present a short summary of his work. I contributed to the planning, performing and evaluation of our measurements of the speed of sound. I also contributed to the theoretical prediction based on the $T = 0$ equation of state by Bertaina et al. [95].

Probing thermodynamical behaviour in two-dimensional quantum gases

Thermodynamical properties of a system are fully characterised by an EOS which links macroscopic state variables like pressure P , density n and temperature T . While the EOS itself encodes static properties of a system, derivatives of the EOS capture the dynamic response to small changes in state variables. In principle, the EOS can be obtained from a full microscopic description of the system. In the case of strongly interacting quantum systems in 2D a full theoretical understanding is often lacking, making a derivation of the EOS difficult. Experiments with ultracold quantum gases enable probing of the EOS of strongly interacting 2D systems by studying its static and dynamic properties.

Experimental studies of the static density distribution¹ in weakly interacting 2D Bose gases by Hung et al. [58] and Yefsah et al. [59] revealed the scale-invariant density EOS $n = n(\mu/T)$. Recent experiments probed the equation of state in strongly interacting 2D Bose gases [60] and the ground-state pressure EOS in the BEC-BCS crossover [62]. So far there are no experimental studies of the EOS in the BEC-BCS crossover which include the effect of temperature.

Dynamical properties of 2D Fermi gases in the BEC-BCS crossover were studied in the damping of breathing modes [16] and spin transport [17]. Both experiments delivered results which are not theoretically understood, illustrating the need for

¹The presence of a trapping potential $V(\mathbf{r})$ can be described by a local chemical potential $\mu(\mathbf{r}) = \mu_0 - V(\mathbf{r})$. Therefore, the in-situ density distribution $n(\mathbf{r})$ of an atomic cloud with temperature T directly gives the density equation of state $n = n(\mu, T)$.

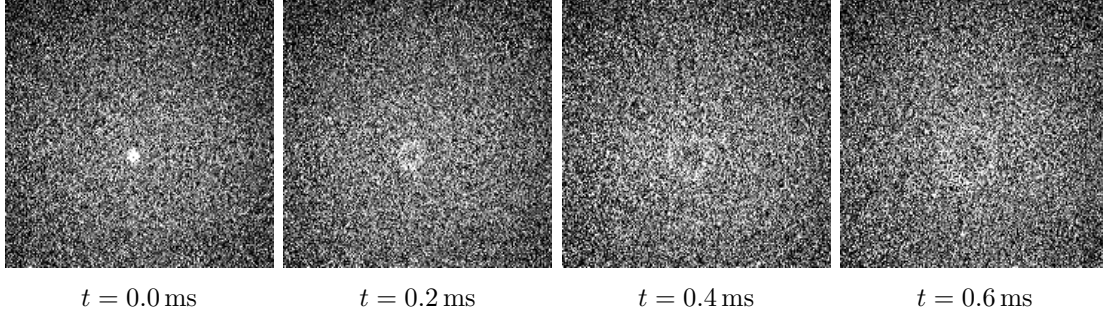


Figure 6.1: Sound propagation in a strongly interacting 2D Fermi gas. We excite sound by creating a density perturbation with a tightly focused red-detuned dipole trap in the center of a strongly interacting 2D Fermi gas with particle number $N = 35000$ and interaction parameter $\ln(k_F a_{2D}) = 0.8$. The propagation of the density is tracked for increasing times t to determine the speed of sound.

further studies of dynamical properties in strongly interacting 2D Fermi gases [101–103]. While the breathing mode is only sensitive to the polytropic exponent γ in an EOS $\mu \propto n^\gamma$, the speed of sound $v_s = \sqrt{n/m \cdot \partial\mu/\partial n}$ captures more information about the chemical potential μ and allows for a more direct comparison with recent predictions of the equation of state [95]. Further, the speed of sound in 2D might reveal the jump in superfluid density as pointed out by Oszawa et al. [100]. Here, we measure the speed of sound in a 2D Fermi gas in the BEC-BCS crossover. For each covered interaction parameter, we determine the EOS from in-situ images as an alternative way to extract the speed of sound. We find excellent agreement between the two approaches to determine the speed of sound. Our measurements connect the static and dynamic behaviour of a 2D Fermi in the BEC-BCS crossover and may provide new insights to understand the controversially discussed topic of strong interactions in 2D quantum gases [101].

Preview: measurements of the speed of sound in 2D

We prepare a single layer of a 2D Fermi gas of ^6Li as described in chapter 2.3. We excite sound by a density perturbation in a highly-oblate 2D geometry similar to our recent work in 3D [15]. The density perturbation is created in the cloud’s center with a tightly-focused red-detuned 780 nm dipole trap. The beam power is ramped up linearly to its final value and suddenly switched off. We track the outward moving density perturbation and measure the distance between peak position of the density excess and cloud center after various delay times to obtain the speed of sound as shown in Fig. 6.1. We measure the speed of sound in clouds with fixed total atom number per spin state $N = 25000$ and various interaction strengths as shown in Fig. 6.2. We tune the interaction parameter $\ln(k_F a_{2D}) \approx -1.5$ to 1.5 across the BEC-BCS crossover by exposing the cloud to magnetic fields $B = 730 \text{ G} - 890 \text{ G}$, facilitating the broad Feshbach resonance of ^6Li . We compare our results to the speed of sound obtained from the pressure EOS $v_s^2 = 1/m \cdot \partial P/\partial n$.

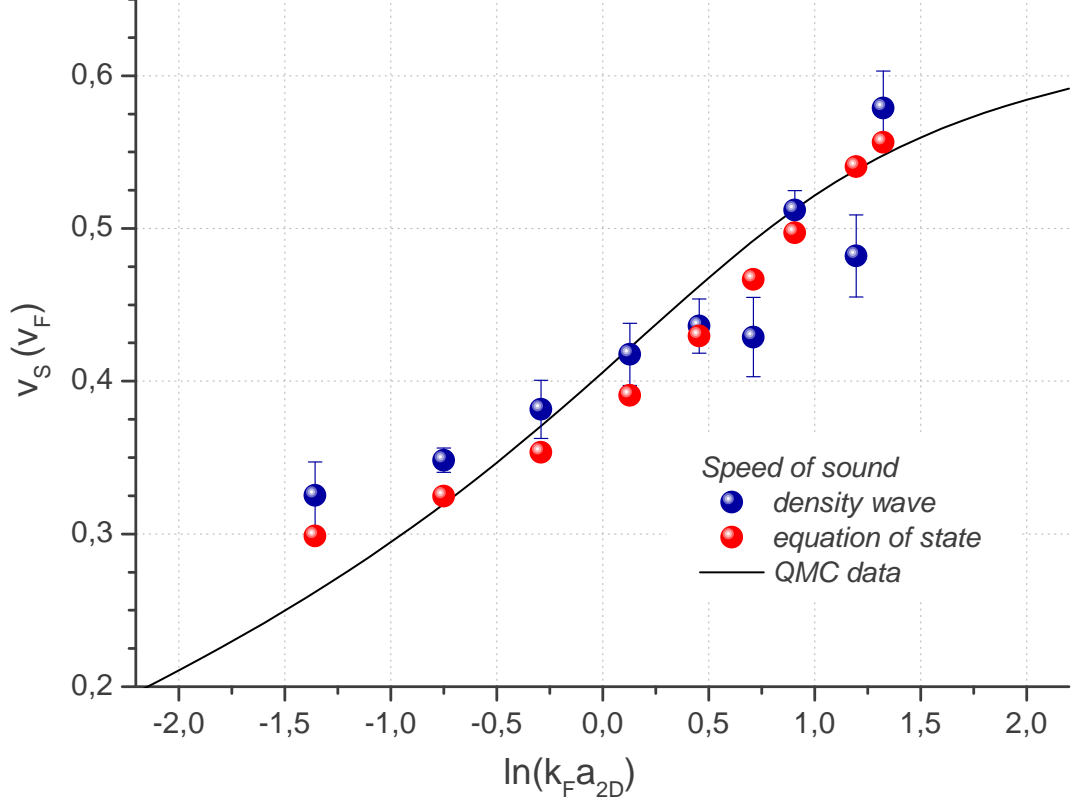


Figure 6.2: The speed of sound in the 2D BEC-BCS crossover. We create a local density perturbation in the center of a 2D Fermi gas and track the propagation of the density maximum (s. Fig. 6.1) to obtain the speed of sound for different values of the interaction parameter $\ln(k_F a_{2D})$ (blue dots). Analysing the density profile $n(\mathbf{r})$ of the sound propagation medium, we obtain the pressure EOS $P(n)$ to calculate the speed of sound as $v_s = \sqrt{1/m \cdot \partial P / \partial n}$ (blue dots). Our results are compared to the recent zero-temperature QMC EOS by Bertaina et al. [95] (black line).

We obtain $P(n)$ by analysing the in-situ density distribution $n(\mathbf{r})$ of the trapped 2D Bose gas. We determine the spatial form of the trapping potential $V(\mathbf{r})$ to obtain the pressure $P = \int n(V) dV$. As shown in Fig. 6.2, we observe excellent agreement between the two approaches to determine the speed of sound. Therefore, our results provide a reliable testing ground for theoretical predictions of the EOS. Recent zero-temperature QMC calculations by Bertaina et al. [95] are in good agreement with our experimental results.

Bibliography

- [1] P. Anderson, *More is different*, Science **177**, 393 (1972).
- [2] N. Mott, *The basis of the electron theory of metals, with special reference to the transition metals*, Proc. Phys. Soc. Sect. A **416** (1949).
- [3] F. Steglich, J. Aarts, C. Bredl, W. Lieke, D. Meschede, W. Franz, and H. Schäfer, *Superconductivity in the Presence of Strong Pauli Paramagnetism: Ce Cu₂ Si₂*, Phys. Rev. Lett. **437**, 1892 (1979).
- [4] J. Bednorz and K. Müller, *Possible high T_c superconductivity in the BaLaCuO system*, Zeitschrift für Phys. B Condens. Matter **193**, 189 (1986).
- [5] D. Tsui, H. Stormer, and A. Gossard, *Two-dimensional magnetotransport in the extreme quantum limit*, Phys. Rev. Lett. **48**, 1559 (1982).
- [6] G. Kotliar and D. Vollhardt, *Strongly correlated materials: Insights from dynamical mean-field theory*, Phys. Today 53–59 (2004).
- [7] P. Lee, N. Nagaosa, and X. Wen, *Doping a Mott insulator: Physics of high-temperature superconductivity*, Rev. Mod. Phys. **78**, 17 (2006).
- [8] E. Altman, E. Demler, and M. Lukin, *Probing many-body states of ultracold atoms via noise correlations*, Phys. Rev. A **70**, 013603 (2004).
- [9] N. Mermin and H. Wagner, *Absence of ferromagnetism or antiferromagnetism in one-or two-dimensional isotropic Heisenberg models*, Phys. Rev. Lett. **17**, 1133 (1966).
- [10] P. Hohenberg, *Existence of long-range order in one and two dimensions*, Phys. Rev. **158**, 383 (1967).
- [11] J. Kosterlitz and D. Thouless, *Ordering, metastability and phase transitions in two-dimensional systems*, J. Phys. C Solid State Phys. **6**, 1181 (1973).
- [12] V. Berezinskii, *Destruction of long-range order in one-dimensional and two-dimensional systems having a continuous symmetry group I. classical systems*, Sov. Phys. JETP **32**, 2 (1971).
- [13] Z. Hadzibabic, P. Krüger, M. Cheneau, B. Battelier, and J. Dalibard, *Berezinskii–Kosterlitz–Thouless crossover in a trapped atomic gas*, Nature **441**, 1118 (2006).

- [14] J.-y. Choi, S. Seo, W. Kwon, and Y.-i. Shin, *Probing phase fluctuations in a 2D degenerate Bose gas by free expansion*, Phys. Rev. Lett. **109**, 125301 (2012).
- [15] W. Weimer, K. Morgener, V. Singh, J. Siegl, K. Hueck, N. Luick, L. Mathey, and H. Moritz, *The critical velocity in the BEC-BCS crossover*, arXiv Prepr. arXiv1408.5239v1 5 (2014).
- [16] E. Vogt, M. Feld, B. Fröhlich, D. Pertot, M. Koschorreck, and M. Köhl, *Scale invariance and viscosity of a two-dimensional Fermi gas*, Phys. Rev. Lett. **108**, 070404 (2012).
- [17] M. Koschorreck, D. Pertot, E. Vogt, and M. Köhl, *Universal spin dynamics in two-dimensional Fermi gases*, Nat. Phys. **9**, 405 (2013).
- [18] W. Weimer, *Probing superfluid properties in strongly correlated Fermi gases with high spatial resolution*, Ph.D. thesis, Universität Hamburg (2014).
- [19] K. Morgener, *tba*, Ph.D. thesis, Universität Hamburg (2014).
- [20] I. Bloch, J. Dalibard, and W. Zwerger, *Many-body physics with ultracold gases*, Rev. Mod. Phys. **80**, 885 (2008).
- [21] D. Bishop and J. Reppy, *Study of the Superfluid Transition in Two-Dimensional He 4 Films*, Phys. Rev. Lett. **40**, 1727 (1978).
- [22] K. Novoselov, A. Geim, S. Morozov, D. Jiang, M. Katsnelson, I. Grigorieva, S. Dubonos, and A. Firsov, *Two-dimensional gas of massless Dirac fermions in graphene*, Nature **438**, 197 (2005).
- [23] I. Bloch, *Ultracold quantum gases in optical lattices*, Nat. Phys. **1** (2005).
- [24] J. Dalibard, F. Gerbier, G. Juzeliunas, and P. Öhberg, *Colloquium: Artificial gauge potentials for neutral atoms*, Rev. Mod. Phys. **83**, 1523 (2011).
- [25] S. Sachdev, *Quantum phase transitions*, Cambridge Univ. Press (2007).
- [26] D. Jaksch, C. Bruder, J. Cirac, C. Gardiner, and P. Zoller, *Cold bosonic atoms in optical lattices*, Phys. Rev. Lett. **81**, 3108 (1998).
- [27] M. Greiner, O. Mandel, T. Esslinger, T. Hänsch, and I. Bloch, *Quantum phase transition from a superfluid to a Mott insulator in a gas of ultracold atoms*, Nature 39–44 (2002).
- [28] W. Ketterle and M. Zwierlein, *Making, probing and understanding ultracold Fermi gases*, arXiv Prepr. arXiv0801.2500v1 206 (2008).
- [29] W. Phillips, *Laser cooling and trapping of neutral atoms* (1992).

- [30] S. Chu, L. Hollberg, J. Bjorkholm, A. Cable, and A. Ashkin, *Three-dimensional viscous confinement and cooling of atoms by resonance radiation pressure*, Phys. Rev. Lett. **55** (1985).
- [31] H. Metcalf and P. V. d. Straten, *Laser cooling and trapping*, Graduate Texts in Contemporary Physics, Springer New York, New York, NY (1999).
- [32] K. Davis, M. Mewes, M. Andrews, N. van Druten, D. Durfee, D. Kurn, and W. Ketterle, *Bose-Einstein condensation in a gas of sodium atoms*, Phys. Rev. Lett. **75** (1995).
- [33] M. Anderson, J. Ensher, M. Matthews, C. Wiemann, and E. Cornell, *Observation of Bose-Einstein condensation in a dilute atomic vapor*, Science **269**, 198 (1995).
- [34] S. Inouye, M. Andrews, J. Stenger, H. Miesner, D. Stamper-Kurn, and W. Ketterle, *Observation of Feshbach resonances in a Bose-Einstein condensate*, Nature **392**, 151 (1998).
- [35] B. DeMarco and D. Jin, *Onset of Fermi degeneracy in a trapped atomic gas*, Science **285**, 1703 (1999).
- [36] M. Greiner, C. Regal, and D. Jin, *Emergence of a molecular Bose-Einstein condensate from a Fermi gas*, Nature **426**, 537 (2003).
- [37] S. Jochim, M. Bartenstein, A. Altmeyer, G. Hendl, S. Riedl, C. Chin, J. Hecker Denschlag, and R. Grimm, *Bose-Einstein condensation of molecules*, Science **2101**, 2101 (2003).
- [38] M. Zwierlein, C. Stan, C. Schunck, S. Raupach, A. Kerman, and W. Ketterle, *Condensation of pairs of fermionic atoms near a Feshbach resonance*, Phys. Rev. Lett. **92**, 120403 (2004).
- [39] K. Hueck, *Erzeugung und Untersuchung von ultrakalten, zweidimensionalen Fermi-Gasen*, Master's thesis, Universität Hamburg (2013).
- [40] D. Boiron, A. Michaud, P. Lemonde, Y. Castin, C. Salomon, S. Weyers, K. Szymaniec, L. Cagnet, and A. Clairon, *Laser cooling of cesium atoms in gray optical molasses down to 1.1 μ K*, Phys. Rev. A **53**, R3734 (1996).
- [41] G. Zürn, T. Lompe, A. Wenz, S. Jochim, P. Julienne, and J. Hutson, *Precise Characterization of Li 6 Feshbach Resonances Using Trap-Sideband-Resolved RF Spectroscopy of Weakly Bound Molecules*, Phys. Rev. Lett. **110**, 135301 (2013).
- [42] A. Görlitz, J. Vogels, A. Leanhardt, C. Raman, T. Gustavson, J. Abo-Shaeer, A. Chikkatur, S. Gupta, S. Inouye, T. Rosenband, and W. Ketterle, *Realization of Bose-Einstein condensates in lower dimensions*, Phys. Rev. Lett. **87**, 130402 (2001).

- [43] D. Rychtarik, B. Engeser, H.-C. Nägerl, and R. Grimm, *Two-dimensional Bose-Einstein condensate in an optical surface trap*, Phys. Rev. Lett. **92**, 173003 (2004).
- [44] G. Modugno, F. Ferlaino, R. Heidemann, G. Roati, and M. Inguscio, *Production of a Fermi gas of atoms in an optical lattice*, Phys. Rev. A **68**, 011601 (2003).
- [45] K. Günter, T. Stöferle, H. Moritz, M. Köhl, and T. Esslinger, *p-Wave interactions in low-dimensional fermionic gases*, Phys. Rev. Lett. **95**, 230401 (2005).
- [46] P. Cladé, C. Ryu, A. Ramanathan, K. Helmerson, and W. Phillips, *Observation of a 2D Bose gas: From thermal to quasicondensate to superfluid*, Phys. Rev. Lett. **102**, 170401 (2009).
- [47] T. Meyrath, F. Schreck, J. Hanssen, C.-S. Chuu, and M. Raizen, *A high frequency optical trap for atoms using Hermite-Gaussian beams*, Opt. Express **13**, 2843 (2005).
- [48] K. Martiyanov, V. Makhalov, and A. Turlapov, *Observation of a two-dimensional Fermi gas of atoms*, Phys. Rev. Lett. **105**, 030404 (2010).
- [49] M. Ries, A. Wenz, G. Zürn, L. Bayha, I. Boettcher, D. Kedar, P. Murthy, M. Neidig, T. Lompe, and S. Jochim, *Observation of pair condensation in a strongly interacting two-dimensional Fermi gas*, arXiv Prepr. arXiv1409.5273v1 (2014).
- [50] L. Landau, *The theory of a Fermi liquid*, Sov. Phys. JETP-USSR (1957).
- [51] A. Abrikosov and I. Khalatnikov, *The theory of a fermi liquid (the properties of liquid ^3He at low temperatures)*, Reports Prog. Phys. (1959).
- [52] R. Laughlin, *Anomalous quantum Hall effect: an incompressible quantum fluid with fractionally charged excitations*, Phys. Rev. Lett. **50**, 1395 (1983).
- [53] A. Georges, G. Kotliar, W. Krauth, and M. Rozenberg, *Dynamical mean-field theory of strongly correlated fermion systems and the limit of infinite dimensions*, Rev. Mod. Phys. **68** (1996).
- [54] G. Astrakharchik, J. Boronat, J. Casulleras, and S. Giorgini, *Equation of state of a Fermi gas in the BEC-BCS crossover: A quantum Monte Carlo study*, Phys. Rev. Lett. **93**, 200404 (2004).
- [55] M. Ku, A. Sommer, L. Cheuk, and M. Zwierlein, *Revealing the superfluid lambda transition in the universal thermodynamics of a unitary Fermi gas*, Science **335**, 563 (2012).

- [56] C. Nayak, S. Simon, A. Stern, M. Freedman, and S. Das Sarma, *Non-Abelian anyons and topological quantum computation*, Rev. Mod. Phys. **80**, 1083 (2008).
- [57] A. Kitaev, *Fault-tolerant quantum computation by anyons*, Ann. Phys. (N. Y). **303**, 2 (2003).
- [58] C. Hung, X. Zhang, N. Gemelke, and C. Chin, *Observation of scale invariance and universality in two-dimensional Bose gases*, Nature **470**, 236 (2011).
- [59] T. Yefsah, R. Desbuquois, L. Chomaz, K. J. Günter, and J. Dalibard, *Exploring the thermodynamics of a two-dimensional Bose gas*, Phys. Rev. Lett. **107**, 130401 (2011).
- [60] L. Ha, C. Hung, X. Zhang, U. Eismann, S.-K. Tung, and C. Chin, *Strongly interacting two-dimensional Bose gases*, Phys. Rev. Lett. **110**, 145302 (2013).
- [61] B. Fröhlich, M. Feld, E. Vogt, M. Koschorreck, W. Zwerger, and M. Köhl, *Radio-frequency spectroscopy of a strongly interacting two-dimensional Fermi gas*, Phys. Rev. Lett. **106**, 105301 (2011).
- [62] V. Makhalov, K. Martiyanov, and A. Turlapov, *Ground-state pressure of quasi-2D Fermi and Bose gases*, Phys. Rev. Lett. **112**, 045301 (2014).
- [63] D. Petrov and G. Shlyapnikov, *Interatomic collisions in a tightly confined Bose gas*, Phys. Rev. A **64**, 012706 (2001).
- [64] Z. Hadzibabic and J. Dalibard, *Two-dimensional Bose fluids: An atomic physics perspective*, arXiv Prepr. arXiv:0912.1490v3 51 (2009).
- [65] R. Desbuquois, L. Chomaz, T. Yefsah, J. Leonard, J. Beugnon, C. Weitenberg, and J. Dalibard, *Superfluid behaviour of a two-dimensional Bose gas*, Nat. Phys. **8**, 645 (2012).
- [66] R. Brown and R. Twiss, *Correlation between photons in two coherent beams of light*, Nature (1956).
- [67] M. Greiner, C. Regal, J. Stewart, and D. Jin, *Probing pair-correlated fermionic atoms through correlations in atom shot noise*, Phys. Rev. Lett. **94**, 110401 (2005).
- [68] S. Fölling, F. Gerbier, A. Widera, O. Mandel, T. Gericke, and I. Bloch, *Spatial quantum noise interferometry in expanding ultracold atom clouds*, Nature **695**, 692 (2005).
- [69] J. Simon, W. Bakr, R. Ma, M. Tai, P. Preiss, and M. Greiner, *Quantum simulation of antiferromagnetic spin chains in an optical lattice*, Nature **472**, 307 (2011).

- [70] M. Schellekens, R. Hoppeler, A. Perrin, J. Viana Gomes, D. Boiron, A. Aspect, and C. Westbrook, *Hanbury Brown Twiss effect for ultracold quantum gases*, Science **310**, 648 (2005).
- [71] C. Sanner, E. Su, A. Keshet, R. Gommers, and Y.-i. Shin, *Suppression of density fluctuations in a quantum degenerate Fermi gas*, Phys. Rev. Lett. **105**, 040402 (2010).
- [72] T. Müller, B. Zimmermann, J. Meineke, J.-P. Brantut, T. Esslinger, and H. Moritz, *Local observation of antibunching in a trapped Fermi gas*, Phys. Rev. Lett. **105**, 040401 (2010).
- [73] A. Polkovnikov, E. Altman, and E. Demler, *Interference between independent fluctuating condensates*, Proc. Natl. Acad. Sci. **103**, 6125 (2006).
- [74] R. Desbuquois, *Thermal and superfluid properties of the two-dimensional Bose gas*, Ph.D. thesis (2013).
- [75] V. Singh and L. Mathey, *Noise correlations of two-dimensional Bose gases*, Phys. Rev. A **89**, 053612 (2014).
- [76] O. Penrose and L. Onsager, *Bose-Einstein condensation and liquid helium*, Phys. Rev. **104** (1956).
- [77] S. Pilati, S. Giorgini, and N. Prokof'ev, *Critical temperature of interacting Bose gases in two and three dimensions*, Phys. Rev. Lett. **4** (2008).
- [78] D. Nelson and J. Kosterlitz, *Universal jump in the superfluid density of two-dimensional superfluids*, Phys. Rev. Lett. **39**, 1201 (1977).
- [79] V. Bagnato and D. Kleppner, *Bose-Einstein condensation in low-dimensional traps*, Phys. Rev. A **44**, 7439 (1991).
- [80] N. Prokof'ev, O. Ruebenacker, and B. Svistunov, *Critical point of a weakly interacting two-dimensional Bose gas*, Phys. Rev. Lett. **87**, 270402 (2001).
- [81] D. Petrov, M. Holzmann, and G. Shlyapnikov, *Bose-Einstein condensation in quasi-2D trapped gases*, Phys. Rev. Lett. (2000).
- [82] T. Simula and P. Blakie, *Thermal activation of vortex-antivortex pairs in quasi-two-dimensional Bose-Einstein condensates*, Phys. Rev. Lett. **96**, 020404 (2006).
- [83] R. Bisset, M. Davis, T. Simula, and P. Blakie, *Quasicondensation and coherence in the quasi-two-dimensional trapped Bose gas*, Phys. Rev. A **79**, 033626 (2009).
- [84] Q. Niu, I. Carusotto, and A. Kuklov, *Imaging of critical correlations in optical lattices and atomic traps*, Phys. Rev. A **73**, 053604 (2006).

- [85] S. Hofferberth, I. Lesanovsky, T. Schumm, a. Imambekov, V. Gritsev, E. Demler, and J. Schmiedmayer, *Probing quantum and thermal noise in an interacting many-body system*, Nat. Phys. **4**, 489 (2008).
- [86] S. Manz, R. Bücker, T. Betz, C. Koller, S. Hofferberth, I. Mazets, A. Imambekov, E. Demler, A. Perrin, J. Schmiedmayer, and T. Schumm, *Two-point density correlations of quasicondensates in free expansion*, Phys. Rev. A **81**, 031610 (2010).
- [87] H. Talbot, *LXXVI. Facts relating to optical science. No. IV*, Philos. Mag. Ser. 3 **9**, 401 (1836).
- [88] A. Imambekov, I. Mazets, D. Petrov, V. Gritsev, S. Manz, S. Hofferberth, T. Schumm, E. Demler, and J. Schmiedmayer, *Density ripples in expanding low-dimensional gases as a probe of correlations*, Phys. Rev. A **80**, 033604 (2009).
- [89] M. Berry, I. Marzoli, and W. Schleich, *Quantum carpets, carpets of light*, Phys. World 1–6 (2001).
- [90] A. Lohmann and J. Thomas, *Making an array illuminator based on the Talbot effect*, Appl. Opt. **29**, 1 (1990).
- [91] S. Seo, J.-y. Choi, and Y.-i. Shin, *Scaling behavior of density fluctuations in an expanding quasi-two-dimensional degenerate Bose gas*, Phys. Rev. A **89**, 043606 (2014).
- [92] D. Petrov, M. Baranov, and G. Shlyapnikov, *Superfluid transition in quasi-two-dimensional Fermi gases*, Phys. Rev. A **67**, 031601 (2003).
- [93] P. Murthy, D. Kedar, T. Lompe, M. Neidig, M. Ries, A. Wenz, G. Zürn, and S. Jochim, *Matter wave Fourier optics with a strongly interacting two-dimensional Fermi gas*, arXiv Prepr. arXiv1408.4680v1 1–7 (2014).
- [94] P. Krüger, Z. Hadzibabic, and J. Dalibard, *Critical point of an interacting two-dimensional atomic Bose gas*, Phys. Rev. Lett. **99**, 040402 (2007).
- [95] G. Bertaina and S. Giorgini, *BCS-BEC crossover in a two-dimensional Fermi gas*, Phys. Rev. Lett. **106**, 110403 (2011).
- [96] C. Hung, X. Zhang, L. Ha, S. Tung, N. Gemelke, and C. Chin, *Extracting density–density correlations from in situ images of atomic quantum gases*, New J. Phys. **13**, 075019 (2011).
- [97] J. H. Drewes, *Aufbau eines hochauflösenden optischen Systems zur Untersuchung ultrakalter Quantengase*, Master’s thesis, Universität Hamburg (2012).

- [98] L. Landau, *The theory of superfluidity of helium II*, J. Phys. (1941).
- [99] L. Sidorenkov, M. Tey, R. Grimm, Y. Hou, L. Pitaevskii, and S. Stringari, *Second sound and the superfluid fraction in a Fermi gas with resonant interactions*, Nature **498**, 78 (2013).
- [100] T. Ozawa and S. Stringari, *Discontinuities in the First and Second Sound Velocities at the Berezinskii-Kosterlitz-Thouless Transition*, Phys. Rev. Lett. **112**, 025302 (2014).
- [101] J. Levinsen and M. Parish, *Strongly interacting two-dimensional Fermi gases* (2014).
- [102] J. Hofmann, *Quantum anomaly, universal relations, and breathing mode of a two-dimensional Fermi gas*, Phys. Rev. Lett. **108**, 185303 (2012).
- [103] E. Taylor and M. Randeria, *Apparent Low-Energy Scale Invariance in Two-Dimensional Fermi Gases*, Phys. Rev. Lett. **109**, 135301 (2012).

List of Figures

2.1	Overview of the experimental apparatus to create an ultracold Fermi gas	13
2.2	Formation of a molecular BEC of ^6Li dimers	14
2.3	Illustration of the preparation of a single two-dimensional layer . . .	15
2.4	Verification of the creation of a single two-dimensional layer	16
3.1	Phase correlations in a trapped 3D Bose gas	23
3.2	Phase correlations in a trapped 2D Bose gas	25
3.3	Free expansion as a probe of phase correlations on different length scales	31
3.4	Extracting density-density correlations after variable expansion time	33
3.5	Probing phase correlations on different length scales	35
3.6	Density-density correlations in areas of specific density	36
4.1	Images of the momentum distribution of a strongly interacting 2D Bose gas for different interaction strengths	41
4.2	Radial momentum distribution of a strongly interacting 2D Bose gas	43
4.3	Fitting thermal wings of a Bose gas	43
4.4	Testing the evaluation of density-density correlations using test distributions	47
4.5	Subtraction of the shot noise contribution	49
4.6	Deceleration of the rapid expansion in axial direction	51
4.7	Reducing the cloud width in axial direction after free expansion. . .	51
4.8	Critical point of the BKT transition in strongly interacting Bose gas	53
4.9	In-situ density fluctuations as a probe of the quasi-condensate . . .	53
4.10	Extracting the scaling exponent and cutoff from the power spectrum	55
4.11	Effect of the evaluation radius r_{max} on the power spectrum.	56
4.12	Algebraic scaling exponent and cutoff length in a strongly interacting 2D Bose gas	57
4.13	Superfluid density reconstructed from the algebraic scaling exponent	58
4.14	Algebraic scaling exponent for different expansion times	59
6.1	Sound propagation in a strongly interacting 2D Fermi gas	70
6.2	The speed of sound in the 2D BEC-BCS crossover	71

Danksagung

Als erstes möchte ich mich bei Prof. Dr. Henning Moritz bedanken. Bereits während der Masterarbeit selbstständig mit Doktoranden an aktuellen Experimenten arbeiten zu dürfen ist gewiss keine Selbstverständlichkeit. Vielen Dank für die zahlreichen Diskussionen, die intensive Betreuung und nicht zuletzt die wunderbare Gruppenatmosphäre, zu der du ganz entscheidend beiträgst.

Ein großes Danke gilt ebenfalls den Doktoranden Wolf, Kai, Jonas, und Klaus. Ich habe mich von Anfang an bei euch in der Gruppe wohl gefühlt. Da ihr euch stets die Zeit genommen habt, mir die Details des experimentellen Aufbaus zu erklären, habe ich während des letzten Jahres sehr viel von euch lernen können. Ich schließe mich den Worten meines Vorgängers an: Gut, dass der Spaß mit euch nicht nur im Labor zu kurz kam!

Weiterhin möchte ich Prof. Dr. Ludwig Mathey für die stets aufschlussreichen Diskussionen und auch für die Übernahme der Rolle des zweiten Gutachters danken.

Nicht zuletzt gilt mein Dank meiner Familie, auf deren Rückhalt ich mich immer verlassen kann.

Eidesstattliche Erklärung

Hiermit bestätige ich, dass die vorliegende Arbeit von mir selbstständig verfasst wurde und ich keine anderen als die angegebenen Hilfsmittel – insbesondere keine im Quellenverzeichnis nicht benannten Internet-Quellen – benutzt habe und die Arbeit von mir vorher nicht einem anderen Prüfungsverfahren eingereicht wurde. Die eingereichte schriftliche Fassung entspricht der auf dem elektronischen Speichermedium. Ich bin damit einverstanden, dass die Masterarbeit veröffentlicht wird.

Hamburg, den 24. Oktober 2014
